Advanced Image Reconstruction in Parallel Magnetic Resonance Imaging: Constraints and Solutions

by

Ernest N. Yeh

S.B. Electrical Engineering and Computer Science
M.Eng. Electrical Engineering and Computer Science
Massachusetts Institute of Technology, 1998

SUBMITTED TO THE HARVARD-MIT DIVISION OF HEALTH SCIENCES AND TECHNOLOGY IN PARTIAL FULFILLMENT OF THE REQUIREMENTS FOR THE DEGREE OF

DOCTOR OF PHILOSOPHY IN ELECTRICAL AND MEDICAL ENGINEERING
AT THE
MASSACHUSETTS INSTITUTE OF TECHNOLOGY

JUNE 2005

Signature of Author: _____
Harvard-MIT Division of Health Sciences and Technology
May 5, 2005

Certified by: _____
Daniel K. Sodickson, M.D., Ph.D.
Assistant Professor of Radiology and Medicine
Beth Israel Deaconess Medical Center
Harvard Medical School
Thesis Supervisor

Accepted by: _____
Martha L. Gray, Ph.D.
Edward Hood Taplin Professor of Medical and Electrical Engineering
Co-Director, Harvard-MIT Division of Health Science and Technology

Advanced Image Reconstruction in Parallel Magnetic Resonance Imaging: Constraints and Solutions

Ernest N. Yeh

Submitted to the Harvard-MIT Division of Health Sciences and Technology on May 5, 2005 in Partial Fulfillment of the Requirements for the Degree of Doctor of Philosophy in Electrical and Medical Engineering.

ABSTRACT

Imaging speed is a crucial consideration for magnetic resonance imaging (MRI). The speed of conventional MRI is limited by hardware performance and physiological safety measures. "Parallel" MRI is a new technique that circumvents these limitations by utilizing arrays of radiofrequency detector coils to acquire data in parallel, thereby enabling still higher imaging speeds.

In parallel MRI, coil arrays are used to accomplish part of the spatial encoding that was traditionally performed by magnetic field gradients alone. MR signal data acquired with coil arrays are spatially encoded with the distinct reception patterns of the individual coil elements. The quality of parallel MR images is dictated by the accuracy and efficiency of an image reconstruction (decoding) strategy. This thesis formulates the spatial encoding and decoding of parallel MRI as a generalized linear inverse problem. Under this linear algebraic framework, theoretical and empirical limits on the performance of parallel MR image reconstructions are characterized, and solutions are proposed to facilitate routine clinical and research applications.

Each research study presented in this thesis addresses one or more elements in the inverse problem, and the studies are collectively arranged to reflect three progressive stages in solving the inverse problem: 1) determining the encoding matrix, 2) computing a matrix inverse, 3) characterizing the error involved. First, a self-calibrating strategy is proposed which uses non-Cartesian trajectories to automatically determine coil sensitivities without the need of an external scan or modification of data acquisition, guaranteeing an accurate formulation of the encoding matrix. Second, two matrix inversion strategies are presented which, respectively, exploit physical properties of coil encoding and the phase information of the magnetization. While the former allows stable and distributable matrix inversion using the *k*-space locality principle, the latter integrates parallel image reconstruction with conjugate symmetry. Third, a numerical strategy is presented for computing noise statistics of parallel MRI techniques which involve magnitude image combination, enabling quantitative image comparison. In addition, fundamental limits on the performance of parallel image reconstruction are derived using the Cramer-Rao bounds. Lastly, the practical applications of techniques developed in this thesis are demonstrated by a case study in improved coronary angiography.

Thesis Supervisor: Daniel K. Sodickson, M.D., Ph.D.
Title: Assistant Professor of Radiology and Medicine, Harvard Medical School

ACKNOWLEDGEMENTS

With much joy and humility, I am here to celebrate with each and every one of you whose love, sacrifice and guidance have helped me reach this milestone. This short acknowledgement simply could not convey the many thoughts of mine.

My family has been the greatest blessing in my life. As I was growing up, there was never a single day that I did not feel loved. My parents have taught me the virtue of hard work and optimism. For the twelve years I have been at MIT, my father has worked, without complaints, two full-time jobs to support my education. My mother, who has also made many sacrifices, has nurtured me a relentless passion for education. My big sister, Selina, serving the role of a parent since our immigration to the US, has, through her example, inspired me to pursue my dreams in this land of opportunities.

I have also been blessed by an elite group of colleagues whose intellects are only surpassed by their genialities. My thesis supervisor, Daniel Sodickson, has been instrumental in every aspect during my formative years as a young scientist. He has provided a magical balance of freedom and guidance, allowing me to explore my interests without getting lost. Charles McKenzie, who has taught me everything I know about MR scanners, has also granted me the privileges to work closely with him on many exciting projects. Aaron Grant,

with his vast knowledge about almost every phenomenon in physics, has equally impressive patience in reviewing and offering suggestions to my thesis at various stages. Michael Ohliger, my officemate for five years, has always been the first one to listen to my ideas, and has also devoted many hours in helping refine my thesis.

I would like to express my special gratitude to my thesis committee. David Staelin has been generous in offering his mentorship in multiple occasions. Dave was the course director for a class which I taught as a TA, then served in my PhD qualifying committee, and now serves in my thesis committee. Rene Botnar, who has taken the trouble to fly back from Germany to attend my defense, has been a wonderful mentor, colleague, and friend. Rene has demonstrated to me how to simultaneously excel in both physics and physique.

There are many friends who have been supportive along the way. William Peake, my undergraduate academic advisor, has continued to be my source of inspiration. BakFun and MeiKee Wong have warmly taken me to their family and provided wisdom and guidance in my searching years. Friends in the MIT Hong Kong Student Bible Study Group, whose heritage and faith I share, have fought side-by-side in many battles of the graduate life. To all of us who are graduating, a job well done!

Last and most importantly, I am inexplicably blessed by my wife, Connie, who has gone through the ups and downs in my graduate years, and is duly credited for giving this thesis document a professional touch. Together, we are thrilled to see the conclusion of my PhD, and ready to embark a new phase of our lives.

This research has been supported by the generosity of the Harvard-MIT Division of Health Sciences and Technology; the National Institutes of Health; and the Whitaker Foundation.

TABLE OF CONTENTS

LIST OF FIGURES

LIST OF TABLES

CHAPTER 1. INTRODUCTION

SECTION 1.1 General Introduction: Parallel Magnetic Resonance Imaging

Magnetic resonance imaging (MRI) allows non-invasive diagnostic assessment of the human body without the risk of ionizing radiation. The quality of MR image is critically determined by the imaging speed. However, hardware performance and physiological safety measures have limited the speed of conventional MRI. In recent years, parallel MRI techniques have been developed that utilize radiofrequency (RF) coil arrays to accelerate image acquisition beyond these previous limits (1-9).

Conventional MRI uses magnetic field gradients to spatially encode the magnetic resonance (MR) signal in order to produce an image with resolution many times finer than the signal wavelength. This so-called Fourier encoding technique, though invented to make MRI possible in the first place (10,11), considerably limits the image acquisition speed, since MR signal data have to be acquired one Fourier component at a time. In 1977, the first clinical MR image of the human body took 5 hours to acquire (12), and nowadays, after almost three decades of research and development, a single MR image can be acquired in less than a second. While this is a significant accomplishment, conventional MRI has more or

less reached its imaging speed limit. Even when the most modern conventional scanner hardware is used, cumulative acquisition times may be excessively long for clinical diagnosis that requires datasets of particularly high spatial and temporal resolution. Unfortunately, safety guidelines regarding magnetic field gradient switching and RF power deposition preclude further increases in imaging speed

Prolonged acquisitions are especially problematic for imaging of moving structures such as the heart. Even though several techniques (e.g., breath-holding (13), electrocardiogram gating (14) and diaphragmatic tracking (15)) have been developed to help circumvent the speed bottleneck, accelerating image acquisition remains the most attractive and fundamental solution.

In parallel MRI, RF coil arrays are used to share the burden of spatial encoding that is conventionally accomplished by magnetic field gradients. The spatially varying sensitivities of an RF coil array provide additional encoding of the received MR signal data, and this spatial information permits images to be reconstructed from a small subset of the original Fourier-encoded dataset. In other words, some of the Fourier-encoding steps can be omitted in the image acquisition, consequently accelerating image acquisition. In contrast to the sequential data acquisition scheme in conventional MRI, parallel MRI techniques allow parallel data acquisition via the use of multiple RF detector coils.

Since its first clinical demonstration in 1997 (2), investigators have reported ever increasing acceleration factors, recently up to a factor of 16 in vivo (16). The ability to perform markedly faster MRI not only promises many immediate benefits (e.g., improving image quality, reducing examination time, increasing patient comfort), but also opens up new possibilities (e.g., single breath-hold whole-heart coronary angiography) that were previously inaccessible.

SECTION 1.2 Statement of the Thesis

To date, various challenges in image reconstruction have complicated everyday clinical applications of parallel MRI. This thesis formulates the image reconstruction of parallel MRI as a generalized linear inverse problem. Under this framework, theoretical and practical limits on the performance of parallel MR image reconstruction are characterized. In particular, six important aspects of parallel MRI are addressed, and practical solutions are proposed to facilitate routine clinical and research applications.

1.2.a Coil Sensitivity Calibration: Accuracy and Consistency

In parallel imaging, MR signal data are spatially encoded using RF coil sensitivities, and parallel image reconstruction requires accurate knowledge of the underlying RF coil reception patterns. RF coils are typically positioned close to the anatomy of interest in order to obtain favorable signal-to-noise ratio. As a result, coil positioning and hence detailed coil sensitivity patterns may change from patient to patient, and potentially from image acquisition to image acquisition, (e.g., as a result of patient motion).

Coil sensitivity information for parallel MRI can be obtained either from separate reference scans (external calibration) or from reference scans incorporated within the accelerated image acquisitions themselves (self calibration). The use of self-calibrating techniques is attractive since they eliminate the need for additional calibration scans and avoid potential mismatches between calibration scans and subsequent accelerated acquisitions. However, most examples of self-calibrating techniques require modification of data sampling trajectories, potentially limiting the flexibility and the maximum acceleration factor in image acquisitions.

Chapter 2 proposes an inherently self-calibrating image acquisition that makes use of non-Cartesian sampling trajectories. Commonly used non-Cartesian trajectories, namely spiral and radial trajectories, offer inherent self-calibrating characteristics because of their densely sampled centers. At no additional cost in acquisition time and with no modification in scanning protocols, *in vivo* coil sensitivity maps may be extracted from the densely-

sampled central regions of *k*-space. Illustrative examples are presented to demonstrate feasibility, and physical arguments are put forward to establish the theoretical minimal amount of calibration information required for a successful parallel image reconstruction. Future directions for coil sensitivity calibration are outlined.

1.2.b Computational Efficiency and Stability

After the coil sensitivities are accurately calibrated, parallel MR images can in principle be reconstructed by solving a system of linear equations. However, the system of equations involved is typically prohibitively large for arbitrary sampling trajectories. Efficient algorithms only exist for special cases in which data are sampled on a regularly-spaced Cartesian grid where the Fast Fourier Transform (FFT) can be applied to reduce the computational burden. Even then, the final solution may not be numerically stable, and the numeric instability is especially pronounced in highly accelerated parallel imaging. Together, the computational efficiency and stability represent critical constraints on the performance of parallel MRI, restricting most current applications to relatively low acceleration factors and regular sampling trajectories.

In Chapter 3, the principle of *k*-space locality is exploited to address some of these computational constraints. An efficient and stable parallel image reconstruction algorithm is proposed: Parallel magnetic resonance imaging with Adaptive Radius in *k*-Space (PARS). In RF coil encoding, information relevant to reconstructing an omitted datum rapidly diminishes as a function of *k*-space separation between the omitted datum and the acquired signal data. The proposed PARS method harnesses this principle of *k*-space locality via a sliding-window approach to judiciously partition the large system of equations into manageable and distributable independent systems of equations, achieving both computational efficiency and numerical stability. Additionally, an empirical method designed to measure total error power is described. The total error power of PARS reconstructions is studied over a range of *k*-space radii and accelerations, revealing "minimal-error" conditions at comparatively modest *k*-space radii. For experimental verifications, PARS reconstructions of undersampled *in vivo* Cartesian and non-Cartesian datasets are shown, and are compared selectively with standard

parallel image reconstructions. Various characteristics of PARS (such as the tradeoff between signal-to-noise ratio and artifact power, and the relationship with iterative parallel conjugate- gradient approaches or non-parallel gridding approaches) are discussed.

1.2.c Phase Constraint: Exploitation of Phase Information for Parallel MRI

When an image has a slowly spatially-varying phase, conjugate symmetry in k-space allows that image to be reconstructed accurately using only slightly more than half of the data which would otherwise be required. This phase-constrained approach, which can improve image acquisition time by as much as a factor of two, is commonly referred to as half Fourier or, more generally, partial Fourier encoding. Partial Fourier imaging (e.g., Ref. (17)) was clinically implemented for conventional MRI before the invention of parallel MRI. Once parallel imaging techniques became available, it was only natural to combine them with partial Fourier encoding so as to increase imaging speeds still further. However, this combination can also present certain challenges for image reconstruction. Most combinations attempted so far have used sequential concatenations of partial Fourier and parallel image reconstructions. Depending on the particular parallel imaging methods used, and on the order of concatenations, the phase calibration or other conditions for accurate reconstruction may cease to be valid. The lack of mathematical rigor and generality in concatenated approaches could limit their reliablity and robustness for clinical diagnosis.

Chapter 4 presents an integrated image reconstruction approach to combine partial Fourier encoding and parallel imaging. A generalized framework is provided for reconstructing images encompassing either or both techniques and for comparing image quality achieved by varying *k*-space sampling schemes. The theory of integrated phase-constrained parallel MRI is outlined, and the phase calibration requirements and limitations are discussed. A special derivation is devoted to combining the phase constraint and the *k*-space locality principle. Simulations, phantom experiments, and *in vivo* experiments are presented.

1.2.d Error Analysis: Noise in Magnitude Images

Quantitative noise analysis of MR image constructions provides an objective metric to evaluate the performance of a particular image reconstruction approach. However, no noise analysis tool is available for parallel image reconstruction strategies which involve magnitude operations. As a result, comparative noise analysis cannot be performed among these parallel image algorithms, or against other approaches which do not involve magnitude operations.

In general, noise analysis in parallel MRI is different from that of conventional MRI in two critical aspects: First, unlike conventional MRI where noise is uniformly distributed in the reconstructed image, the noise in parallel MR images exhibits significant spatial variation. The signal-to-noise ratio (SNR) can no longer be calculated by a region-of-interest (ROI) approach where the power of noise and signal is estimated in regions that are noise- and signal-dominant, respectively. This ROI method fails because the noise in the signal-dominant region may have different variance than that of in the noise-dominant region. A common method of measuring SNR by taking the quotient of the signal power and the noise power would be potentially incorrect. Secondly, and more importantly, many parallel image algorithms (including those presented in Chapters 3 and 4) involve reconstructing intermediate images and then performing a magnitude combination (e.g., sum-of-squares combinations) to form a final composite image. These magnitude operations transform the underlying noise statistics from Gaussian distributions to distributions not readily characterized in traditional forms.

In Chapter 5, a generalized noise analysis strategy for magnitude-combined parallel image reconstructions is proposed to provide a quantitative metric first to characterize the new noise distribution, and eventually to provide a new basis for comparing different parallel image reconstruction algorithms. It is shown that the new noise distribution can be represented as a linear combination of non-central chi-squares variates. Numeric solutions are outlined for the general case where no closed-form solution exists, and closed-form solutions are derived for three special degenerate cases.

1.2.e Theoretical Limits of Parallel Image Reconstruction

The work described in Chapters 2-5 addresses specific aspects of parallel MRI including sensitivity calibration, image reconstruction and noise analysis. While this work and other previous parallel MRI advances have been developed largely within the MRI community, analogous array processing technologies have also been developed in other disciplines. In fact, the use of detector arrays is common not only in medical imaging such as ultra-sound and multi-detector computerized tomography (MD-CT), but also in non-medical fields such as telecommunications and radio-astronomy. The quest to find fundamental performance limits in parallel image reconstruction has serendipitously led to a convergent path with other array processing technologies. In particular, a close correspondence with multi-input multi-output (MIMO) systems in telecommunications has been reported at a recent conference. Questions have been raised as to whether current parallel image reconstructions are statistically optimal, and if not, whether decoding algorithms in the MIMO system can be used to improve parallel image reconstruction.

Chapter 6 tests the optimality of image reconstruction for parallel MRI by adapting the decoding apparatus used for MIMO. Cramer-Rao bounds for parallel MRI are established. A special case where noise is of Gaussian distribution is explored, and a demonstration of the use of a maximum likelihood decoding algorithm, namely the Viterbi decoding algorithm, is presented. Results from simulations are compared to those predicted by the Cramer-Rao bounds.

1.2.f Adaptation of a Cardiac Imaging Technique to Parallel MRI

Physiological constraints, e.g. cardiac and respiratory motion, have been a driving force for continual improvement in MR imaging technology. Even though parallel MRI has achieved many-fold accelerations, these physiological constraints are still important considerations in designing imaging protocols. For example, some of the speed gained by parallel MRI may be traded for greater tolerance of heart beat irregularity (cardiac

arrhythmia). It is important to evaluate how the existing clinical imaging protocols could be optimized for use with parallel imaging.

Chapter 7 presents a case study of anatomy-specific clinical applications of parallel MRI. In MR coronary angiography, imaging parameters (e.g., magnetic field gradients, RF excitations and receiver bandwidth) have been designed to work under the timing constraints of conventional MRI. The added flexibility provided by parallel imaging warrants a re-examination of these imaging parameters. Specifically, the study explores the possibility of trading some of imaging speed gain by parallel MRI for increased tolerance for heart rate variability. This study helps conclude the thesis work by demonstrating how a new technological advance can be translated and refined to meet specific clinical needs.

SECTION 1.3 Background

The physical and engineering principles of MRI have been documented in many textbooks (e.g., Ref. (18)). This section is not intended as a comprehensive exposition of MRI. Rather, principles pertinent to the understanding of parallel MRI are reviewed in order to provide a platform for discussion of the dissertation work. A special focus is devoted to spatial encoding and decoding methodologies for conventional and parallel MRI. A formulation of the linear inverse problem for MR image reconstruction is derived, and selected examples of parallel image reconstruction methods are provided.

1.3.a The MR Signal

The MR signal originates from the quantum mechanical phenomenon of nuclear magnetic resonance (NMR). Under the influence of an external magnetic field, the nuclear spins of a given atomic species (e.g., hydrogen nuclei) produce a net equilibrium magnetization M_o given by:

$$\bar{M}(\mathbf{r}) = M_o(\mathbf{r})\hat{\mathbf{z}} = \frac{\gamma^2\hbar^2}{4k_BT} B(\mathbf{r})\rho(\mathbf{r})\hat{\mathbf{z}} \qquad [1.1]$$

Here, $\mathbf{r}$ is the 3-dimensional spatial vector, γ is the gyromagnetic ratio of the atomic species of interest, $\hbar$ is Planck's constant, k_B is Boltzmann's constant, and T is the temperature in degrees Kelvin. $B(\mathbf{r})$ is the magnitude of the external magnetic field, and $\rho(\mathbf{r})$ is the spin density of the atomic species. The unit vector $\hat{\mathbf{z}}$ is parallel to the external magnetic field.

The magnetization vector can be rotated from the z axis by applying a radiofrequency (RF) excitation pulse, resulting in a time-varying magnetization in the transverse plane (x-y plane). The overall effect of the RF excitation is summarized by the flip angle $\alpha(\mathbf{r})$, and the magnetization vector now has a time-dependence, expressed as follows [1]:

$$\vec{M}(\mathbf{r},t) = M_z(\mathbf{r})\hat{\mathbf{z}} + \mathrm{Re}\left[M_{xy}(\mathbf{r}) e^{-i\omega(\mathbf{r})t} (\hat{\mathbf{x}} - i\hat{\mathbf{y}}) \right] \qquad [1.2]$$

where

$$\begin{aligned} M_z(\mathbf{r}) &= \cos(\alpha(\mathbf{r})) \cdot M_o(\mathbf{r}) \\ M_{xy}(\mathbf{r}) &= \sin(\alpha(\mathbf{r})) \cdot M_o(\mathbf{r}) \end{aligned} \qquad [1.3]$$

and $\omega(\mathbf{r})$ is the Larmor frequency at which the nucleus precesses:

$$\omega(\mathbf{r}) = \gamma B(\mathbf{r}). \qquad [1.4]$$

Finally, the oscillating magnetization vector produces a changing magnetic flux in a nearby RF coil, and the voltage induced around the RF coil can be expressed in terms of a volume integral of M_{xy},

$$v(t) \propto \mathrm{Re}\left[\int C(\mathbf{r}) M_{xy}(\mathbf{r}) e^{-i\omega(\mathbf{r})t} d^3r \right]. \qquad [1.5]$$

Here, the spatially varying $C(\mathbf{r})$ represents the RF reception sensitivity, which is a function of the particular geometry of the coil and its position relative to the magnetization unit. $C(\mathbf{r})$ can be calculated using Maxwell's Equations (or the Biot-Savart law for sufficiently low frequencies) in combination with the principle of reciprocity (19).

---

[1]The rotated magnetization vector reverts to the equilibrium state with the longitudinal and transverse relaxation time constants, T_1 and T_2 respectively. The difference of T_1 and T_2 among tissue types can be harnessed to enhance image contrast. However, this topic is beyond the scope of the thesis. In this thesis work, the T_1 and T_2 effects are intentionally omitted to better illustrate the issues of spatial encoding in parallel MRI. However, the generalized framework of this thesis does allow easy incorporation of T_1 and T_2 effects in constructing the generalized encoding matrix described in later sections.

The voltage $v(t)$ is subsequently demodulated by $\cos(\omega_o t)$ and $\sin(\omega_o t)$, and the results are combined to yield the complex MR signal $s(t)$ as follows,

$$s(t) = \int C(\mathbf{r}) M_{xy}(\mathbf{r}) e^{-i(\omega(\mathbf{r})-\omega_o)t} d^3r, \qquad [1.6]$$

where ω_o is the demodulation carrier frequency given by:

$$\omega_o = \gamma B_o, \qquad [1.7]$$

and B_o is the static component of $B(\mathbf{r})$. (Details about $B(\mathbf{r})$ will be presented later in Eq. [1.19].)

1.3.b Imaging with the MR Signal: Spatial Encoding and Image Reconstruction

The long wavelength of the MR signal (e.g., 5 m in vacuum at 1.5 Tesla) precludes resolving an object within the image using traditional diffraction methods. Instead, uniquely-identifiable spatial information must be encoded into the MR signal, and the image is reconstructed by properly decoding the spatially-encoded MR signal. After expanding the MR signal equation by substituting Eq., [1.1] into Eq. [1.6],

$$\begin{aligned} s(t) &= \int C(\mathbf{r}) \sin(\alpha(\mathbf{r})) M_o(\mathbf{r}) e^{-i(\omega(\mathbf{r})-\omega_o)t} d^3r \\ &= \frac{\gamma^2\hbar^2}{4k_B T} \int C(\mathbf{r}) \sin(\alpha(\mathbf{r})) B(\mathbf{r}) e^{-i\gamma(B(\mathbf{r})-B_o)t} \rho(\mathbf{r}) d^3r \end{aligned}, \qquad [1.8]$$

there are four spatially dependent functions inside the volume integral. Besides the spin density, $\rho(\mathbf{r})$, which is unknown, the other three functions (i.e., $C(\mathbf{r})$, $\alpha(\mathbf{r})$ and $B(\mathbf{r})$) are parameters that can be in principle measured *a priori*. Generally speaking, these three functions reflect spatial encoding at three distinct stages: in the beginning, the RF pulse provides an excitation pattern, $\alpha(\mathbf{r})$; at the end, the MR signal received is weighted by the

coil sensitivity, $C(\mathbf{r})$; in between the RF excitation and the signal reception, the magnetic field, $B(\mathbf{r})$, dictates the phase evolution.[2]

In the general case where all three functions are used to perform spatial encoding, the spatial encoding function $E_\xi(\mathbf{r})$ may be defined as follows:

$$E_\xi(\mathbf{r}) \equiv \beta C(\mathbf{r}) \sin(\alpha(\mathbf{r})) B(\mathbf{r}) e^{-i\gamma(B(\mathbf{r})-B_o)t}\Big|_{t=t_\xi}, \qquad [1.9]$$

where β denotes a scalar accounting for the constants outside of the integral of Eq. [1.8]. The discrete-time signal s_ξ:

$$s_\xi = s(t_\xi), \qquad [1.10]$$

can be interpreted as a generalized projection of $\rho(\mathbf{r})$ onto $E_\xi(\mathbf{r})$ and expressed using the notation of the inner product,

$$s_\xi = \langle E_\xi(\mathbf{r}), \rho(\mathbf{r}) \rangle. \qquad [1.11]$$

A set of basis functions then produces a signal vector with N elements,

$$\mathbf{s} = \begin{bmatrix} s_1 \\ s_2 \\ \vdots \\ s_N \end{bmatrix} = \left\langle \begin{matrix} E_1(\mathbf{r}), \\ E_2(\mathbf{r}), \\ \vdots \\ E_N(\mathbf{r}), \end{matrix} \quad \rho(\mathbf{r}) \right\rangle. \qquad [1.12]$$

In theory, because $\rho(\mathbf{r})$ is a continuous function with infinite dimensions, it would require infinitely many projections to perfectly reconstruct $\rho(\mathbf{r})$. In practice, however, appropriate discretization of the continuous position vector $\mathbf{r}$ can be applied to $\rho(\mathbf{r})$ at selected voxel locations $\mathbf{r}_\gamma$, resulting in a column vector $\boldsymbol{\rho}$,

$$\boldsymbol{\rho}_\gamma = \rho(\mathbf{r}_\gamma). \qquad [1.13]$$

Eq. [1.12] can now be rewritten using as a matrix equation,

$$\mathbf{s} = \mathbf{E}\boldsymbol{\rho} \qquad [1.14]$$

---

[2] $B(\mathbf{r})$ also determines the equilibrium magnetization, $M_o(\mathbf{r})$, which has a lesser role in spatial encoding than the phase evolution.

where the entries of the encoding matrix **E** are:

$$\mathbf{E}_{\xi,\gamma} \equiv E_{\xi}\left(\mathbf{r}_{\gamma}\right). \qquad [1.15]$$

ρ can be uniquely reconstructed from N linearly-independent projections, where N equals to the number of voxels. The spatial encoding equations in Eq. [1.14] are central to this thesis work because they immediately cast the image reconstruction problem as a generalized linear inverse problem, which assumes a more familiar form:

$$\mathbf{b} = \mathbf{A}\mathbf{x} \qquad [1.16]$$

where **b** is traditionally the vector of observations, **A** the known matrix, and **x** the vector of deterministic unknowns. Different MR image reconstruction algorithms, including those for parallel MRI, may differ in appearance and approaches. Nonetheless, these algorithms achieve the ultimate goal of obtaining a solution of ρ,

$$\boldsymbol{\rho} = \mathbf{E}^{-1}\mathbf{s}, \qquad [1.17]$$

in which they explicitly or implicitly perform the three necessary steps of: a) determining the value of the encoding matrix **E**, b) computing an inverse $\mathbf{E}^{-1}$, and c) minimizing the error involved.

The remaining sections in this chapter use this linear algebraic framework to characterize the encoding and decoding methodologies which are representative of existing conventional and parallel MRI techniques.

1.3.c Conventional MRI

1.3.c.1 Spatial Encoding Using Magnetic Field Gradients

Conventional MRI relies on the spatially varying magnetic field $B(\mathbf{r})$ in Eq. [1.9] for spatial encoding. A uniform RF excitation pulse is typically applied to rotate the magnetization at a flip angle $\alpha(\mathbf{r}) = \alpha_0$. The coil sensitivity $C(\mathbf{r})$ is combined with the spin density $\rho(\mathbf{r})$ to form the coil-modulated spin density $\rho_c(\mathbf{r})$. As a result, the MR signal equation (Eq. [1.8]) is simplified to:

$$
\begin{aligned}
s(t) &= \frac{\gamma^2\hbar^2}{4k_BT}\int C(\mathbf{r})\sin(\alpha(\mathbf{r}))B(\mathbf{r})e^{-i\gamma(B(\mathbf{r})-B_o)t}\rho(\mathbf{r})d^3r \\
&= \frac{\gamma^2\hbar^2}{4k_BT}\sin(\alpha_o)\int B(\mathbf{r})e^{-i\gamma(B(\mathbf{r})-B_o)t}\rho_c(\mathbf{r})d^3r
\end{aligned}
\quad . \qquad [1.18]
$$

In most examples of clinical MRI scanners, $B(\mathbf{r})$ is expressed as the sum of the constant external magnetic field B_o and linear magnetic field gradients $G(\mathbf{r})$[3],

$$
B(\mathbf{r}) = B_o + G(\mathbf{r}), \qquad [1.19]
$$

where $G(\mathbf{r})$ can be expressed as the dot product of a gradient vector $\vec{\mathbf{G}}$ with $\mathbf{r}$,

$$
\begin{aligned}
G(\mathbf{r}) &= \vec{\mathbf{G}}\cdot\mathbf{r} \\
&= G_x r_x + G_y r_y + G_z r_z
\end{aligned}
\quad . \qquad [1.20]
$$

Moreover, B_o is typically several orders of magnitude greater than $G(\mathbf{r})$, and Eq. [1.18] becomes,

$$
\begin{aligned}
s(t) &= \frac{\gamma^2\hbar^2}{4k_BT}\sin(\alpha_o)\int B(\mathbf{r})e^{-i\gamma(B(\mathbf{r})-B_o)t}\rho_c(\mathbf{r})d^3r \\
&= \frac{\gamma^2\hbar^2}{4k_BT}\sin(\alpha_o)\int (B_o+G(\mathbf{r}))e^{-i\gamma G(\mathbf{r})t}\rho_c(\mathbf{r})d^3r \,. \qquad [1.21] \\
&\approx \frac{\gamma^2\hbar^2}{4k_BT}\sin(\alpha_o)B_o\int e^{-i\gamma G(\mathbf{r})t}\rho_c(\mathbf{r})d^3r
\end{aligned}
$$

Furthermore, by allowing a time-dependence in $\vec{\mathbf{G}}$, the phase evolution over time can be expressed in terms of $\mathbf{k}\cdot\mathbf{r}$ where the vector $\mathbf{k}$ is defined as,

$$
\mathbf{k} = -\gamma\int_0^t \vec{\mathbf{G}}(t)\,dt\,. \qquad [1.22]
$$

Eq. [1.21] can be rewritten as:

$$
s(\mathbf{k}) = \frac{\gamma^2\hbar^2}{4k_BT}\sin(\alpha_o)B_o\int e^{i\mathbf{k}\cdot\mathbf{r}}\rho_c(\mathbf{r})d^3r\,. \qquad [1.23]
$$

The spatial encoding functions from Eq. [1.9] are simplified as,

---

[3] Nonlinearity of $G(\mathbf{r})$ may occur at the edges of the MR scanner bore, and produce artifacts that can be corrected after the image is reconstructed.

$$E_{\mathbf{k}}(\mathbf{r}) \equiv \beta e^{i\mathbf{k}\cdot\mathbf{r}}, \qquad [1.24]$$

and the matrix equation for image reconstruction becomes:

$$\mathbf{s} = \mathbf{E}\boldsymbol{\rho}_c. \qquad [1.25]$$

The encoding functions are Fourier basis functions, and hence this method of spatial encoding is commonly called Fourier encoding. The elements in the signal vector $\mathbf{s}$ are the Fourier components of the coil-modulated spin density $\boldsymbol{\rho}_c$ evaluated at the corresponding "*k*-space" locations $\mathbf{k}$. An MR dataset is acquired by traversing *k*-space along various values of $\mathbf{k}$[4], and an image is reconstructed by applying an inverse Fourier transformation on the acquired dataset.

$$\begin{aligned} \boldsymbol{\rho}_c &= \mathbf{E}^{-1}\mathbf{s} \\ &= InverseFT(\mathbf{s}) \end{aligned}. \qquad [1.26]$$

In the special cases of regularly sampled *k*-space trajectories, the fast Fourier transformation (FFT) algorithm can be applied. Additionally, the Fourier transformation is a unitary transformation which provides an optimal noise averaging benefit. Here, the three necessary steps stated in Eq. [1.17] are efficiently accomplished without an explicit effort of determining $\mathbf{E}$, computing $\mathbf{E}^{-1}$, or minimizing the error involved.[5]

1.3.c.2 Field of View and Spatial Resolution

The image information attainable using the Fourier encoding and decoding scheme is summarized as follow: the field of view of the reconstructed image is determined by the *k*-space inter-sample separation $\Delta\mathbf{k}$,

$$Field\ of\ View = \frac{2\pi}{\Delta\mathbf{k}}, \qquad [1.27]$$

and the image spatial resolution is set by the extent of the *k*-space trajectory $\mathbf{k}_{max}$[6]

---

[4] Particular traversal sequences used in different *k*-space trajectories (e.g. rectilinear and spiral) are topics in later parts of the thesis.

[5] Substantial MR engineering efforts have been devoted to the design and building of linear magnetic gradients, so that image reconstruction in conventional MRI can be performed with the ease of FFT.

[6] The resolution and the field of view along the principal axes may be independently determined by having different values of $\mathbf{k}_{max}$ and $\Delta\mathbf{k}$ for each axis.

$$Pixel\ Size = \frac{\pi}{\mathbf{k}_{max}}. \qquad [1.28]$$

For regularly sampled (Cartesian) *k*-space trajectories, these relationships are rigorously derived from the Nyquist sampling theorem and the discrete Fourier series. First, sampling with an infinite impulse chain (i.e. $\mathbf{k} = \pm n\Delta\mathbf{k},\ n = 0,1,2,..,\infty$) is equivalent to a periodic replication of the object in the image domain. If the object is of finite length λ and the sampling interval in *k*-space satisfies the Nyquist criterion for $\Delta\mathbf{k} \le \frac{2\pi}{\lambda}$, then the object can be fully reconstructed without aliasing. Second, when a finite impulse chain is used (i.e. $\mathbf{k} = \pm n\Delta\mathbf{k}$, and $|\mathbf{k}| \le \mathbf{k}_{max}$), the voxels reconstructed by discrete Fourier representation are no longer ideal delta functions. Instead, they are sinc functions with zero crossings at integral multiples of $\frac{\pi}{\mathbf{k}_{max}}$, which typically defines the image pixel size.

For irregularly sampled (non-Cartesian) trajectories, the non-uniform sampling density across *k*-space makes it difficult to apply the straightforward relationships in Eq. [1.27] to describe the attainable image information content (20). This challenge and its counterpart in parallel MRI will be collectively addressed using the generalized linear inverse framework later in the thesis.

1.3.c.3 Limitations on Conventional MRI Speed

The imaging speed of conventional MRI is primarily limited by the sequential data acquisition scheme implicitly represented by Eqs. [1.22] and [1.24] where the Fourier-encoded data $s(\mathbf{k})$ are acquired one point at a time. To accelerate image acquisition for the same *k*-space coverage, conventional MRI requires stronger magnetic field gradients, faster gradient switching rates and/or more frequently applied RF pulses (which would result in higher RF power deposition). Unfortunately, any and all of these approaches can pose increasing risks of damaging the underlying biological tissues. In the next section, a safe alternative strategy to accelerate image acquisition is introduced: parallel MRI techniques in which MR data are acquired in parallel via the use of RF coil arrays.

1.3.d Parallel MRI

1.3.d.1 Spatial Encoding Using RF Coil Sensitivities

Parallel MRI techniques make use of RF coil arrays to share the burden of spatial encoding with magnetic field gradients. Individual coil elements have spatially varying sensitivity patterns, and the MR signal equation (Eq. [1.6]) is modified,

$$s_l(t) = \int C_l(\mathbf{r}) \sin\left(\alpha(\mathbf{r})\right) M_o(\mathbf{r}) e^{-i(\omega(\mathbf{r})-\omega_o)t} d^3r, \qquad [1.29]$$

where $s_l(t)$ represents the MR signal received by the l^{th} coil with spatial sensitivity $C_l(\mathbf{r})$. The values of $C_l(\mathbf{r})$ can be determined *a priori* using calibration data, which will be described later in the chapter. Other than the multi-coil detection, the data acquisition scheme in parallel MRI is similar to that of conventional MRI: a uniform RF excitation pulse is initially applied to rotate the net magnetization by a constant flip angle α_o, and magnetic field gradients are used to traverse *k*-space. In analogy to the steps taken in Eqs. [1.21] - [1.25], the MR signal equation for parallel imaging can be expressed as:

$$s_l(\mathbf{k}) = \frac{\gamma^2\hbar^2}{4k_BT} \sin(\alpha_o) B_o \int e^{i\mathbf{k}\cdot\mathbf{r}} C_l(\mathbf{r}) \rho(\mathbf{r}) d^3r \qquad [1.30]$$

and the spatial encoding functions are defined as follows:

$$E_{\mathbf{k},l}(\mathbf{r}) \equiv \beta C_l(\mathbf{r}) e^{i\mathbf{k}\cdot\mathbf{r}}. \qquad [1.31]$$

where the scalar β accounts for the constants outside the integral in Eq. [1.31]. Here, the MR signal is seen as a generalized projection of spin density onto the hybrid encoding function of magnetic field gradients and coil sensitivity. The extra index l in $E_{\mathbf{k},l}$ signifies that the number of encoding functions has increased by a factor equal to the number of array elements, L.

1.3.d.2 Acceleration in Imaging Speed

If a dataset acquired with a one-coil system is sufficient to reconstruct an image, then using an identical sampling trajectory in *k*-space, a dataset acquired with a multi-coil system must contain redundant spatial information. In the framework of the generalized linear inverse problem, the number of equations is increased by a factor of L while the number of

unknowns remains the same. The matrix system is overdetermined. In parallel imaging, this redundancy in spatial encoding is exploited to allow image acceleration. The *k*-space trajectory only needs to traverse a subset of the original *k*-space locations, resulting in a proportionally faster acquisition.

In principle, if there are a very large number of coil elements each with distinct sensitivity, the spatial encoding using magnetic field gradients can be omitted altogether. In such a scenario, MRI would be nearly instantaneous. In practice, the complementary use of magnetic field gradients is still desirable and necessary for reasons that will become apparent.

1.3.d.3 Parallel Image Reconstruction Methods

Image reconstruction in parallel MRI, like the generalized linear inverse framework represented in Eqs. [1.16] and [1.17] , can also be divided into three steps: a) calibration for the encoding matrix **E**; b) computing an inverse $\mathbf{E}^{-1}$; c) minimizing the error involved in the reconstruction.

1.3.d.3.1 Sensitivity Calibration to Obtain the Encoding Matrix E

COIL SENSITIVITY MAPS

Knowledge of the coil sensitivities $C_l(\mathbf{r})$ is required to formulate the encoding functions (Eq. [1.31]) which collectively constitute the encoding matrix **E**. These coil sensitivities can in principle be calculated if the coil array geometry and location are known. In practice, however, for flexible coil arrays whose positions vary from scan to scan, the coil sensitivity information is preferably recalibrated each time. The coil sensitivities can be calibrated from coil-modulated images $\rho_l(\mathbf{r})$, where

$$\rho_l(\mathbf{r}) = C_l(\mathbf{r})\rho(\mathbf{r}) \qquad [1.32]$$

is obtained using conventional MRI acquisition and image reconstruction methods (Eq. [1.26]). These coil images may have lower spatial resolution (i.e., smaller $\mathbf{k}_{max}$ in Eq. [1.28]

) than the accelerated diagnostic images, but are required to have a sufficient field-of-view (i.e., large enough $\Delta\mathbf{k}$ in Eq. [1.27]) to satisfy the Nyquist criterion. To eliminate the spin density component in $\rho_l(\mathbf{r})$, an additional image can be acquired using a bird-cage body coil which is designed to have a uniform RF spatial reception field, $C_{body-coil}(\mathbf{r}) = C_o$. A quotient is performed between the two coil images to obtain a scaled version of $C_l(\mathbf{r})$,

$$\frac{\rho_l(\mathbf{r})}{\rho_{body-coil}(\mathbf{r})} = \frac{C_l(\mathbf{r})\rho(\mathbf{r})}{C_{body-coil}(\mathbf{r})\rho(\mathbf{r})} = \frac{1}{C_o} C_l(\mathbf{r}) \qquad [1.33]$$

If a body-coil image is not available, a sum-of-squares combined image can be used to divide out the spin density,

$$\frac{\rho_l(\mathbf{r})}{\sqrt{\sum_l |\rho_l(\mathbf{r})|^2}} = \frac{C_l(\mathbf{r})\rho(\mathbf{r})}{\sqrt{\sum_l \left(|C_l(\mathbf{r})| \cdot |\rho(\mathbf{r})|\right)^2}} \approx \frac{1}{\sqrt{\sum_l |C_l(\mathbf{r})|^2}} C_l(\mathbf{r}) \qquad [1.34]$$

Since the multiplication of $\frac{1}{\sqrt{\sum_l |C_l(\mathbf{r})|^2}}$ is common to all coils, it can be incorporated in the formulation of an effective encoding function which differs from the original encoding function (Eq. [1.31]) as follows:

$$\tilde{E}_{\mathbf{k},l}(\mathbf{r}) = \frac{E_{\mathbf{k},l}(\mathbf{r})}{\sqrt{\sum_l |C_l(\mathbf{r})|^2}}. \qquad [1.35]$$

The effective spin density reconstructed by parallel MRI is expressed as,

$$\tilde{\rho}(\mathbf{r}) = \sqrt{\sum_l |C_l(\mathbf{r})|^2}\, \rho(\mathbf{r}). \qquad [1.36]$$

An interesting property is illustrated here that an arbitrary function can be used in lieu of $\frac{1}{\sqrt{\sum_l |C_l(\mathbf{r})|^2}}$, and $\rho(\mathbf{r})$ can be obtained by performing a multiplication of the same function to yield $\tilde{\rho}(\mathbf{r})$. This property will prove to be useful in Chapters 2-4.

External Sensitivity Calibration and Self-Calibration

Calibration data, which are used to reconstruct the coil images in Eq. [1.32], can be obtained from a separate scan before or after the image acquisition. Because of the requirement of external information, this approach is generally known as external calibration. Alternatively, the calibration scan can be incorporated as a part of the image acquisition, and the calibration data can be extracted from the image dataset. This approach is called auto-calibration or self-calibration[7]. The crucial difference between the external- and self-calibration approaches lies in the timing of the acquisition of calibration data relative to the image acquisition. These differences are discussed in detail in Chapter 2.

1.3.d.3.2 Image Reconstruction: Computing a Matrix Inverse $\mathbf{E}^{-1}$

Various parallel image reconstruction algorithms have been developed to solve the generalized linear inverse problem, and Sodickson *et al* has shown the linkage between some of the different approaches (7). Here, three major classes of parallel image reconstructions (full matrix inversion, *k*-space block-diagonalization, and image-domain block-diagonalization) are discussed with frequent reference to the central equation: $\mathbf{s} = \mathbf{E}\boldsymbol{\rho}$.

Full Matrix Inversion

The full matrix inversion approach entails a straightforward inversion of Eq. [1.14], finding a matrix inverse $\mathbf{E}^{-1}$ such that $\mathbf{E}^{-1}\mathbf{E} = \mathbf{I}$ and thus,

$$\boldsymbol{\rho}_{recon} = \mathbf{E}^{-1}\mathbf{s}, \qquad [1.37]$$

where $\mathbf{I}$ is an identity matrix. When the image acceleration factor is equal to the number of array elements L, then the encoding matrix $\mathbf{E}$ is square, and $\mathbf{E}^{-1}$ is uniquely determined. Often, however, the acceleration factor is less than L. $\mathbf{E}$ is rectangular with more rows than columns, and the matrix system is overdetermined. $\mathbf{E}^{-1}$ is no longer unique. Instead, the Moore-Penrose pseudo-inverse is used to provide a least-squares solution:

[7] For self-calibrating parallel MRI, methods exist that allow coil sensitivity calibration without explicitly reconstructing the calibration images. These methods however generally observe calibration requirements similar to those described in this section.

$$\mathbf{E}^{-1} = \left(\mathbf{E}^H \mathbf{E}\right)^{-1} \mathbf{E}^H \qquad [1.38]$$

where the superscript $(\cdot)^H$ denotes Hermitian conjugation. (This equation must be modified slightly to minimize error in the presence of noise correlations between array elements: see Section 1.5.c.3 to follow.) While it may be numerically unstable and computationally intensive to calculate the pseudo-inverse, the full matrix inverse approach has the appeal of a theoretically exact solution. Notable representatives of this approach include Subencoding (1), SENSE (3), Space-RIP (4) and GEM (7).

k-SPACE BLOCK-DIAGONALIZATION

SMASH and its derivatives rely on a different approach to matrix inversion using *k*-space block-diagonalization. In the *k*-space block-diagonalization approach, the encoding matrix $\mathbf{E}$ is first Fourier transformed to become $\mathbf{E}_{FT}$, where $\mathbf{E}_{FT} = \mathbf{EF}$ and $\mathbf{F}$ denotes a Fourier transformation matrix. Coil sensitivities are in general band-limited —a property that will be more fully explored later in the thesis — and as a result, the matrix $\mathbf{E}_{FT}$ is approximately band-diagonal. An inverse $\left(\mathbf{E}_{FT}\right)^{-1}_{block-diag}$ can be determined efficiently by applying either block-by-block inversion or sparse matrix techniques. $\mathbf{E}^{-1}$ can be obtained by performing another Fourier transformation as follows,

$$\begin{aligned} \mathbf{E} &= \mathbf{EFF}^{-1} \\ \mathbf{E}^{-1} &= \left(\mathbf{EFF}^{-1}\right)^{-1} \\ &= \mathbf{F}\left(\mathbf{EF}\right)^{-1} \\ &= \mathbf{F}\left(\mathbf{E}_{FT}\right)^{-1}_{block-diag} \end{aligned} \qquad [1.39]$$

The block-by-block inversion, while providing the advantages of numerical stability and computational efficiency, makes the inversion inexact,

$$\mathbf{E}^{-1}\mathbf{E} \approx \mathbf{I}. \qquad [1.40]$$

Tradeoffs between inexactness (artifact) and numerical stability will be an important subject in later chapters. Notable representatives of this *k*-space block-diagonalization approach include SMASH (2), GRAPPA (8), ASP (21), hybrid GEM (7), and generalized SMASH (9).

IMAGE-DOMAIN BLOCK-DIAGONALIZATION

A third approach to parallel image reconstruction is more restrictive than the other two, but it is included here in order to facilitate discussions in Chapter 6 where correspondence between parallel MRI and wireless communications is made. In the image-domain block-diagonalization approach, the coil sensitivity $C_l(\mathbf{r})$ is assumed to have limited spatial extent, and beyond some distance $\lambda_{limited\text{-}FOV}$ from $\mathbf{r}_l$, the value of $C_l(\mathbf{r})$ drops below a threshold value $C_{threshold}$.

$$C_l(\mathbf{r}_l \pm \Delta\mathbf{r}) \le C_{threshold}, \qquad \text{for } |\Delta\mathbf{r}| > \lambda_{limited\text{-}FOV} \qquad [1.41]$$

and $\lambda_{limited\text{-}FOV} \le \lambda_{full-FOV}$. As a result of the smaller field of view, the *k*-space sampling can be more sparsely without incurring aliasing. The coil images may be independently reconstructed as in conventional MRI, and are then combined after being appropriately shifted according to their center position $\mathbf{r}_l$. PILS is a representative of this image-domain block-diagonal approach (5).

1.3.d.3.3 Parallel MRI Error Estimation and Quantification

ERROR IN PARALLEL IMAGE RECONSTRUCTION

In general, there are two types of errors in parallel MR image reconstruction. The first type involves systematic errors that may result from an inaccurate coil sensitivity calibration or an inexact image reconstruction such as the block-diagonalization approaches. It is difficult to quantify these errors since they depend on sporadic events (e.g., sudden motion of the patient which shifts the coil arrays), or are related to the tradeoff between image artifact and signal-to-noise in an inexact reconstruction. These will be discussed more thoroughly in Chapters 3 and 5.

The second type of error is statistical error due to propagation of noise, and algorithms have been developed to minimize this type of error. In MR signal detection, noise manifests itself as a statistical fluctuation of voltage across the terminals of an RF coil, and the underlying stochastic process can be characterized experimentally. In practice, noise at a given RF coil is not temporally correlated. However, noise between the coil elements is

typically correlated, and noise covariance matrix $\tilde{\boldsymbol{\Psi}}$ can be defined where the entry $\tilde{\boldsymbol{\Psi}}_{ll'}$ is the noise correlation between coils l and l'. The overall noise covariance matrix for the signal vector **s** can be expressed as:

$$\boldsymbol{\Psi} = \tilde{\boldsymbol{\Psi}} \otimes \mathbf{Id}_k , \qquad [1.42]$$

where the direct product with the identity, $\mathbf{Id}_k$, indicates replication for all k-space indices.

Noise in the MR Image

In parallel MR images reconstructed using the full matrix inversion, the image noise covariance $\boldsymbol{\Lambda}$ can be expressed in terms of the encoding matrix inverse $\mathbf{E}^{-1}$ and the signal noise covariance matrix $\boldsymbol{\Psi}$,

$$\boldsymbol{\Lambda} = \left(\mathbf{E}^{-1}\right)\boldsymbol{\Psi}\left(\mathbf{E}^{-1}\right)^{H} . \qquad [1.43]$$

To achieve minimize noise covariance in the final image, noise decorrelation can be first performed on the MR signal, $\mathbf{s}_{decorr} = \mathbf{L}^{-1}\mathbf{s}$ and the encoding matrix $\mathbf{E}_{decorr} = \mathbf{L}^{-1}\mathbf{E}$ where the lower triangular matrix $\mathbf{L}$ is obtained from Cholesky decomposition of $\boldsymbol{\Psi}$,

$$\boldsymbol{\Psi} = \mathbf{L}\mathbf{L}^{H} . \qquad [1.44]$$

The minimum-variance version of Eq. [1.38] is,

$$\begin{aligned} \mathbf{E}^{-1}_{\text{min var}} &= \left(\mathbf{E}^{H}_{decor}\mathbf{E}_{decorr}\right)^{-1}\mathbf{E}^{H}_{decorr} \\ &= \left(\left(\mathbf{L}^{-1}\mathbf{E}\right)^{H}\left(\mathbf{L}^{-1}\mathbf{E}\right)\right)^{-1}\left(\mathbf{L}^{-1}\mathbf{E}\right)^{H} , \\ &= \left(\mathbf{E}^{H}\boldsymbol{\Psi}^{-1}\mathbf{E}\right)^{-1}\mathbf{E}^{H}\left(\mathbf{L}^{-1}\right)^{H} \end{aligned} \qquad [1.45]$$

and the new image noise variance matrix in the final image is,

$$\begin{aligned} \boldsymbol{\Lambda}_{\text{min var}} &= \left(\left(\mathbf{E}^{H}_{decorr}\mathbf{E}_{decorr}\right)^{-1}\mathbf{E}^{H}_{decorr}\right)\mathbf{I}\left(\left(\mathbf{E}^{H}_{decorr}\mathbf{E}_{decorr}\right)^{-1}\mathbf{E}^{H}_{decorr}\right)^{H} \\ &= \left(\mathbf{E}^{H}_{decorr}\mathbf{E}_{decorr}\right)^{-1} \\ &= \left(\left(\mathbf{L}^{-1}\mathbf{E}\right)^{H}\left(\mathbf{L}^{-1}\mathbf{E}\right)\right)^{-1} \\ &= \left(\mathbf{E}^{H}\boldsymbol{\Psi}^{-1}\mathbf{E}\right)^{-1} \end{aligned} . \qquad [1.46]$$

The final image reconstruction including noise correlations then becomes

$$\boldsymbol{\rho}_{\text{reconstructed}} = \mathbf{E}_{\text{minvar}}^{-1}\mathbf{s}_{decorr} = \left\{\left(\mathbf{E}^H\boldsymbol{\Psi}^{-1}\mathbf{E}\right)^{-1}\mathbf{E}^H\boldsymbol{\Psi}^{-1}\right\}\mathbf{s}. \qquad [1.47]$$

An important note should be made that the example shown here involves only linear operations. When the parallel image reconstruction involves non-linear operations (such as magnitude combination), the noise variance is no longer defined within traditional metrics, and thus will require new methods such as the one proposed in Chapter 5.

NOISE AMPLIFICATION IN PARALLEL MRI

Noise metrics have been developed for parallel imaging techniques whose noise characteristics have been characterized by Eq. [1.43]. These metrics typically focus on the amplification of noise in an image reconstructed from an undersampled dataset compared to that of a fully-sampled reference dataset. The noise variance in an image voxel, γ, is given by the diagonal element of $\boldsymbol{\Lambda}$,

$$\sigma^2 = \boldsymbol{\Lambda}_{\gamma\gamma}, \qquad [1.48]$$

and a noise amplification factor, *g*-factor, is defined as

$$g = \sqrt{\frac{\sigma_{accel}^2}{\sigma_{ref}^2 \cdot R}} = \frac{1}{\sqrt{R}} \cdot \frac{SNR_{ref}}{SNR_{accel}}, \qquad [1.49]$$

where σ_{accel}^2 and σ_{ref}^2 are the noise variances in the parallel and conventional MR images respectively, and R is the image acceleration factor between the parallel and reference images. In general, the decrease in SNR in a parallel MR image reconstruction is due two factors: the inherent loss of noise averaging due to the reduction of data samplings and the non-orthogonality of RF coil encoding. For example, the Fourier encoding functions in conventional MRI are orthogonal, allowing a unitary matrix inversion with optimal noise averaging. However, the generalized encoding functions in parallel MRI are not orthogonal because of the overlapping of broad coil sensitivities. As a result, the matrix inversion in parallel image reconstruction is no longer unitary. Only in the ideal case when the coil sensitivities are perfectly orthogonal would g-factor reach the theoretical lower bound of 1. In practice, the g-factor provides an internal assessment of the spatial encoding capability of a particular RF coil array. However, a more definitive assessment is to evaluate the absolute

SNR (or noise variances) of the image reconstruction. Paradoxically, a coil array carefully optimized for *g*-factor may yield a lower absolute SNR than an array whose g-factor is otherwise not optimized.

1.3.e Transmit Encoding

Spatial Encoding with Spatially-Selective RF Pulses

The remaining spatially-varying term in Eq. [1.6] is the flip angle $\alpha(\mathbf{r})$. This component does not provide an immediate benefit of accelerating image acquisition, and parallel MRI until recently has not incorporated this component. In fact, this thesis work assumes spatially uniform RF excitations. A portion of Chapter 7 proposes a strategy involving the use of various flip angles, but it is not intended for the purpose of spatial encoding. For the interest of completeness and also for future directions of MRI, it is important to note the potential of using RF pulses to performing additional spatial encoding.

Volume-selective RF pulses are commonly used to provide uniform excitation within a volume **V**,

$$\alpha(\mathbf{r}) = \begin{cases} \alpha_o, & \text{for } \mathbf{r} \in \mathbf{V} \\ 0, & \text{otherwise} \end{cases}. \qquad [1.50]$$

More complex excitation patterns can be achieved by using appropriate combinations of RF and gradient waveforms, or else by using RF coil arrays to transmit. Active research is exploring the expansion of spatial encoding capabilities to realize a full complement of encoding functions:

$$E_{\mathbf{k},l,m}(\mathbf{r}) \equiv \beta \sin\left(\alpha_m(\mathbf{r})\right) C_l(\mathbf{r}) e^{-i\mathbf{k}\cdot\mathbf{r}}. \qquad [1.51]$$

Here, the added index m denotes the different excitation patterns that can be applied at different time points (22), or else in different excitation coils (23,24). The number of basis functions in the new encoding matrix **E**, as well as its over-determinacy, has increased by a factor of m. When the extra encoding is applied at different time points, it comes at a cost of increasing the acquisition time by the same factor, but this approach may be used to tailor encoding functions so as to provide numerical stability that is not achievable otherwise.

When the extra encoding is applied using arrays of transmit coils, the duration of RF pulses and or the RF power deposition may be reduced for any given pulse profile (this approach is commonly referred to as "Transmit Parallel Imaging.") An in-depth exposition of the full potential of spatially varying RF excitation is beyond the scope of this dissertation. Nevertheless, the last dimension in MR spatial encoding and decoding is an important subject for ongoing research (23,24).

SECTION 1.4 General Summary

The organization of the thesis can be best presented in relation to the generalized linear inverse problem. Chapters 2-7, though designed to be individually self-contained, are collectively arranged in logical sequence to address the different elements of the inverse problem. Chapter 2 establishes an accurate and robust method for measuring $\mathbf{E}$. Chapter 3 proposes an efficient algorithm to invert $\mathbf{E}$ based on a special RF encoding characteristic. Chapter 4 focuses on a physical property of ρ that facilitates the matrix inversion. Chapter 5 analyzes the effects of noise and systematic errors on the reconstruction of ρ. Chapter 6 derives the theoretical limits on the overall inverse problem $\mathbf{s} = \mathbf{E}\rho$. Chapter 7 reports a practical case study in clinical cardiac imaging using the techniques developed in this thesis.

Chapter 1 References

1. Ra JB, Rim CY. Fast imaging using subencoding data sets from multiple detectors. Magn Reson Med 1993;30(1):142-5.
2. Sodickson DK, Manning WJ. Simultaneous acquisition of spatial harmonics (SMASH): fast imaging with radiofrequency coil arrays. Magn Reson Med 1997;38(4):591-603.
3. Pruessmann KP, Weiger M, Scheidegger MB, Boesiger P. SENSE: sensitivity encoding for fast MRI. Magn Reson Med 1999;42(5):952-62.
4. Kyriakos WE, Panych LP, Kacher DF, Westin CF, Bao SM, Mulkern RV, Jolesz FA. Sensitivity profiles from an array of coils for encoding and reconstruction in parallel (SPACE RIP). Magn Reson Med 2000;44(2):301-8.
5. Griswold MA, Jakob PM, Nittka M, Goldfarb JW, Haase A. Partially parallel imaging with localized sensitivities (PILS). Magn Reson Med 2000;44(4):602-9.
6. McKenzie CA, Yeh EN, Sodickson DK. Improved spatial harmonic selection for SMASH image reconstructions. Magn Reson Med 2001;46:831-836.
7. Sodickson DK, McKenzie C. A generalized approach to parallel magnetic resonance imaging. Med Phys 2001;28(8):1629-1643.
8. Griswold MA, Jakob PM, Heidemann RM, Nittka M, Jellus V, Wang J, Kiefer B, Haase A. Generalized autocalibrating partially parallel acquisitions (GRAPPA). Magn Reson Med 2002;47(6):1202-10.
9. Bydder M, Larkman DJ, Hajnal JV. Generalized SMASH imaging. Magn Reson Med 2002;47(1):160-70.
10. Lauterbur P. Image formation by induced local interactions: Examples employing NMR. Nature 1973;242:190.
11. Mansfield P, Grannell PK. NMR 'diffraction' in solids. J Phys C: Solid State Phys 1973;6:L422.
12. Damadian R, Goldsmith M, Minkoff L. NMR in cancer: XVI. FONAR image of the live human body. Physiol Chem Phys 1977;9(1):97-100, 108.
13. Bloomgarden DC, Fayad ZA, Ferrari VA, Chin B, Sutton MG, Axel L. Global cardiac function using fast breath-hold MRI: validation of new acquisition and analysis techniques. Magn Reson Med 1997;37(5):683-92.

14. Glover GH, Pelc NJ. A rapid-gated cine MRI technique. Magn Reson Annual 1988:299.
15. Ehman RL, Felmlee JP. Adaptive technique for high-definition MR imaging of moving structures. Radiology 1989;173(1):255-63.
16. Zhu Y, Hardy CJ, Sodickson DK, Giaquinto RO, Dumoulin CL, Kenwood G, Niendorf T, Lejay H, McKenzie CA, Ohliger MA and others. Highly parallel volumetric imaging with a 32-element RF coil array. Magn Reson Med 2004;52(4):869-77.
17. Margosian P, Schmitt F, Purdy DE. Fast MR imaging: Imaging with half the data. Health Care Instrum 1986;1:195-7.
18. Haacke EM, Brown RW, Thompson MR, Venkatesan R. Magnetic Resonance Imaging: Physical Principles and Sequence Design: Wiley & Sons; 1999.
19. Hoult DI, Chen CN, Sank VJ. The field dependence of NMR imaging. II. Arguments concerning an optimal field strength. Magn Reson Med 1986;3(5):730-46.
20. Pipe JG. Reconstructing MR images from undersampled data: data-weighting considerations. Magn Reson Med 2000;43:867-875.
21. Lee RF, Westgate CR, Weiss RG, Bottomley PA. An analytical SMASH procedure (ASP) for sensitivity-encoded MRI. Magn Reson Med 2000;43(5):716-725.
22. Kyriakos WE, Panych LP. Optimization of Parallel Imaging By Use of Selective Excitation. In: Proc 9th Annual Meeting ISMRM, Glasgow, Scotland, UK, 2001. p 768.
23. Katscher U, Bornert P, Leussler C, van den Brink JS. Transmit SENSE. Magn Reson Med 2003;49(1):144-50.
24. Zhu Y. Parallel excitation with an array of transmit coils. Magn Reson Med 2004;51(4):775-84.

CHAPTER 2. SELF-CALIBRATING NON-CARTESIAN PARALLEL IMAGING[8]

Image reconstruction for parallel MRI has been formulated in Chapter 1 as a linear inverse problem,

$$\mathbf{s} = \mathbf{E}\boldsymbol{\rho}, \qquad [2.1]$$

where the observation vector $\mathbf{s}$ corresponds to the MR signal acquired, the matrix $\mathbf{E}$ the generalized MR encoding matrix, and the unknown vector $\boldsymbol{\rho}$ the spin density of interest. This chapter is devoted to the development of an inherently self-calibrating strategy to determine $\mathbf{E}$.

SECTION 2.1 Introduction

The accuracy of coil sensitivity estimates is a major determinant of the quality of parallel magnetic resonance image reconstructions. While the level of tolerance for sensitivity miscalibration differs from technique to technique, any significant discrepancy in coil sensitivity references introduces systematic errors in reconstructed images while

[8] The work in this chapter has been adapted for publication as "Yeh EN, Stuber M, McKenzie CA, Botnar RM, Leiner T, Ohliger MA, Grant AK, Willig-Onwuachi JD, Sodickson DK. *Inherently Self-Calibrating Non-Cartesian Parallel Imaging.* Magn Reson Med. (In Press)"

degrading overall image quality. Self-calibrating parallel imaging techniques that employ variable-density *k*-space acquisition schemes have been demonstrated (1-4). Self-calibration eliminates the need for an external sensitivity reference, making parallel image reconstructions less susceptible to miscalibration and image degradation resulting from bulk patient motion.

Self-calibrating parallel image reconstructions have been commonly implemented for rectilinear (or Cartesian) trajectories. Phase-encoded lines in the outer *k*-space region are omitted at a chosen outer reduction factor, whereas those in the central *k*-space region remain densely sampled. The densely-sampled central lines are used for calibration, either through fitting directly in *k*-space (1-3), or through Fourier transformation to generate low-resolution *in vivo* sensitivity maps (4). The omitted phase-encoded lines are then reconstructed by a parallel imaging technique of choice.

It has been noted that non-Cartesian trajectories such as spiral and radial trajectories are logical candidates for self-calibration due to their characteristic oversampled *k*-space center (4). Even for accelerated acquisitions, the center of *k*-space will generally be sampled with sufficient density to enable the creation of reliable low-resolution maps of component coil sensitivities without aliasing artifacts. These low-resolution maps can then provide the coil sensitivity references required for reconstruction of the outer *k*-space signal data.

However, non-Cartesian *k*-space trajectories pose greater challenges for parallel image reconstruction than their Cartesian counterparts due to the memory requirements and computational demand of inverting large matrices. Recent work on non-Cartesian sensitivity encoding (non-Cartesian SENSE) using efficient iterative algorithms has brought non-Cartesian parallel image reconstructions into the realm of feasibility (5). In this work, images of accelerated spiral and radial acquisitions are reconstructed by combining self-calibrated sensitivities and non-Cartesian SENSE, verifying the inherently self-calibrating nature of the trajectories and demonstrating the feasibility of self-calibrated non-Cartesian parallel imaging.

SECTION 2.2 Methods

2.2.a *k*-Space Trajectories

Spiral and radial trajectories, two common non-Cartesian trajectories, were used in this work. The selected spiral trajectory was a multi-interleaf Archimedian spiral, described by the following general equations:

$$k_n(t) = \frac{k_{\max}}{\theta(T)}\theta(t)e^{i(\phi_n+\theta(t))}, \quad \left\{ \begin{array}{c} 0 \le t \le T \\ n = 1...N \\ \phi_n = 2\pi n / N \end{array} \right\} \qquad [2.2]$$

$$\theta(t) = \frac{\omega_o t}{\sqrt{1+\zeta t / T}}, \quad 0 \le t \le T. \qquad [2.3]$$

T is the duration of one interleaf, N is the number of spiral interleaves, and ϕ_n is a phase offset. The n^{th} interleaf trajectory $k_n(t)$ covers a disk of radius $k_{\max}$ centered at the origin of *k*-space (for simplicity of notation, k_{max} and any subsequent references to *k*-space index are expressed in units of $\frac{2\pi}{\text{Field of View}}$). $\theta(t)$ increases monotonically over time, and is proportional to the rotation angle and the radius of the spiral. The constant parameter ζ can be chosen to realize different types of spirals with various linear or angular velocities in k-space. ω_o is determined by ζ, T, N, and the target image matrix size:

$$\omega_o = \frac{2\pi}{T} \cdot \frac{(\text{Matrix Size})}{2N} \cdot \sqrt{1+\lambda} \qquad [2.4]$$

In our implementation, a ζ value of 3 and a Matrix Size of 512 were used. The value of $k_{\max}$ was Matrix Size/2 = 256. Each spiral data set consisted of 42 azimuthal interleaves with 6250 sampled data points on each interleaf.

The radial trajectory used in this work is described by Eq. [2.5],

$$k_n(t) = k_{\max}\Gamma(t)e^{i\phi_n}, \quad \left\{ \begin{array}{c} 0 \le t \le T \\ n = 1..N \\ \phi_n = \pi n / N \end{array} \right\}. \qquad [2.5]$$

$\Gamma(t)$ is a ramp function from –1 to 1, and k_{max} is set to 190. Each radial data set consisted of 380 projections with 760 points on each projection, (oversampled by a factor of 2 along the readout direction.) The projections are azimuthally separated by phase offset ϕ_n, where N is the number of projections.

2.2.b In vivo scans

In vivo data were acquired in a volume containing either the left or right coronary arteries of healthy adult volunteers. A 1.5T Gyroscan ACS-NT whole body MR system (Philips Medical Systems, Best, NL), equipped with a commercial five-element Synergy coil array was used for data acquisition. The array consists of two flexible circular elements placed on the chest wall and three rectangular elements contoured to the table and arranged left-to-right at the subject's back.

For spiral acqusitions, a navigator gated and corrected, ECG triggered 3D pulse sequence (6) was used. Data were acquired at a rate of two interleaves per R-R interval, and a total of 42 spiral interleaves were acquired. This sequence used the stack of spirals approach (7), with conventional phase encoding in the slice-selection direction (12 phase encode steps, 30 mm slab thickness) and variable angular speed spiral encoding in-plane (effective TE 1.5 ms, sampling window 70 ms, RF excitation angles = 45° and 60°, 360 mm x 360 mm FOV, 512 x 512 matrix).

For radial acquisitions, data were acquired at a rate of 17 projections per R-R interval, using a navigator gated and corrected, ECG triggered, arrhythmia rejected 3D steady-state free precession sequence (balanced TFE, TR=5.6ms, TE=2.8ms, RF excitation angle = 110°) (8). A total of 380 projections were acquired. This sequence also used the stack approach, with conventional phase encoding in the slice-selection direction (12 phase encode steps, 30 mm slab thickness).

In the twofold (threefold) accelerated cases only every second (third) interleaf/projection was acquired, analogous to omission of phase-encoded lines in the case of rectilinear trajectories.

2.2.c Sensitivity Extraction for Self-Calibration

The spiral and radial trajectories have densely sampled centers, such that even for accelerated acquisitions, the central *k*-space regions are still sufficiently sampled. Fig. 2.1 illustrates two-fold accelerated spiral and radial trajectories. k_{Nyquist} denotes the extent of the central regions from which unaliased low resolution coil sensitivities can be extracted and used as self-calibrated references for parallel imaging. To satisfy the Nyquist sampling criterion in the most straightforward sense, the sampling density inside the central region must be greater than or equal to 1.

The semilog graphs of Fig. 2.2 illustrate the sampling density for the actual trajectories (spiral and radial with 1-fold and 2-fold undersampling) as a function of the distance from the *k*-space origin. This local sampling density was determined by averaging the number of sampling points within the 4-by-4 vicinity of each Cartesian grid point. More sophisticated methods such as the use of Voronoi areas (9) were not used because the added precision gave no apparent benefit in the present case. The reference trajectories maintain a sampling density greater than 1, as mandated by a Nyquist-like criterion to prevent aliasing. However, for 2-fold undersampled trajectories, the density is less than 1 in the outer region of *k*-space. Starting from the center and moving outward radially in *k*-space, the sampling density changes from an oversampled condition to a critically sampled and eventually to an undersampled condition. A Nyquist-like threshold would suggest that the 2-fold undersampled spiral and radial trajectories should have sufficiently sampled regions up to $k_{\text{Nyquist}}=55$ and $k_{\text{Nyquist}}=110$, respectively.

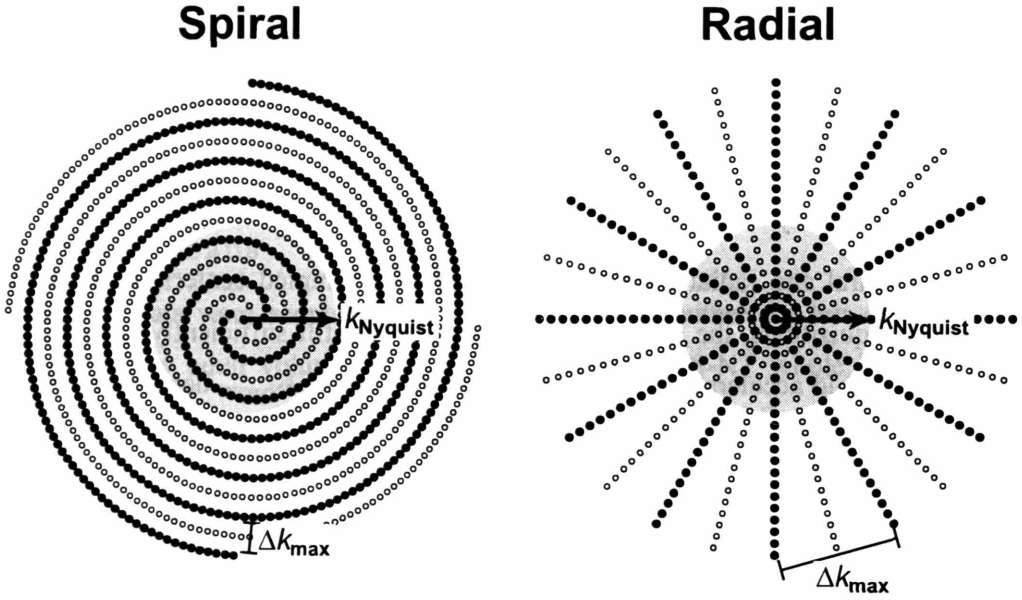

FIGURE 2.1 Self-Calibrating Spiral and Radial Trajectories

For spiral and radial trajectories, image acquisition can be accelerated by omitting interleaves or projections. a) Schematic of a twofold-accelerated spiral trajectory (reduced from 4 to 2 interleaves). b) Schematic of a twofold accelerated radial trajectory (reduced from 12 to 6 projections). Black dots represent k-space data points acquired, and gray dots represent k-space data points omitted. Even in an accelerated acquisition, the center of k-space (shaded regions) is still fully sampled up to a radius of $k_{Nyquist}$. Low-resolution in vivo sensitivities can be extracted from this region to permit self-calibrated parallel image reconstruction. Δk_{max} denotes the maximum separation of k-space points in the outer region. Both $k_{Nyquist}$ and Δk_{max} are important determinants of the quality of self-calibrating parallel image reconstructions.

In order to ensure accurate extraction of sensitivity information, we chose a more stringent sensitivity extraction cutoff k_{cutoff} at twice the Nyquist threshold, that is, by including only points with a local sampling density greater than 2. (To observe the Nyquist criterion, $k_{cutoff} \leq k_{Nyquist}$.) Consequently, coil sensitivity maps were extracted only from regions with k_{cutoff}=18 and k_{cutoff}=40 (k_{cutoff}=10 and k_{cutoff}=25), for the 2-fold (3-fold) undersampled spiral and radial trajectories, respectively. The extracted central k-space regions were then regridded with a Kaiser-Bessel kernel of width=3 and β=13.9086 (Table 2 of Ref. (10)). The resulting low-resolution images were then used as sensitivity references as

described in the following section. An alternative method to obtain the low-resolution sensitivity maps is to employ a direct matrix inversion. The small size of the extracted sensitivity data sets dramatically reduces the burden of the matrix inversion approach, rendering it feasible with current computer hardware.

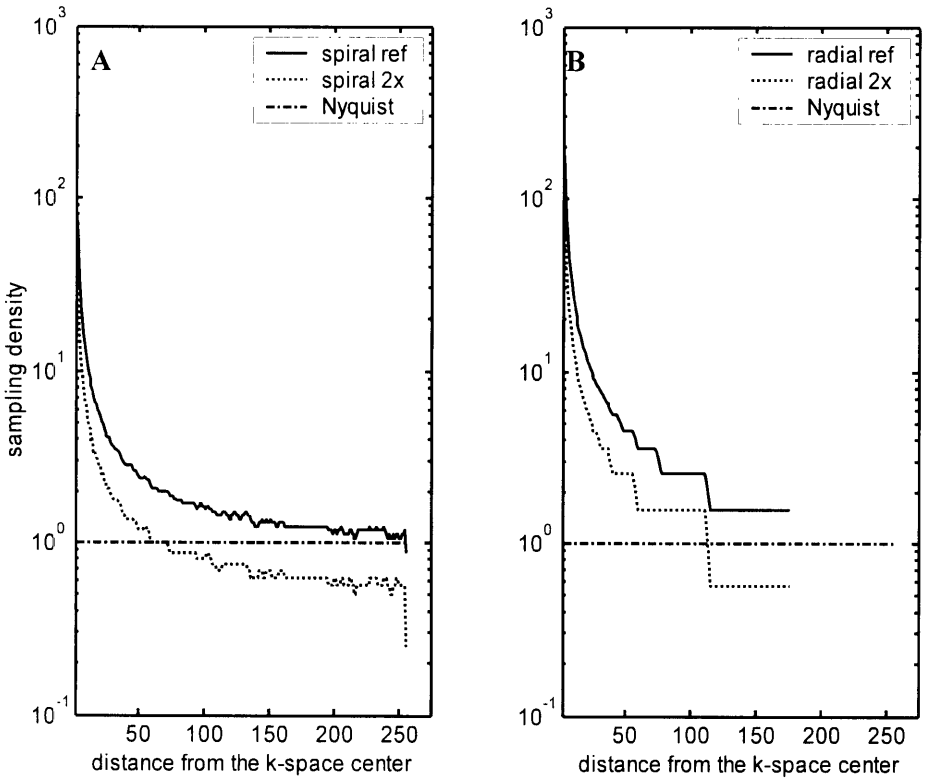

FIGURE 2.2 Sampling Density of Spiral and Radial Trajectories

Semilog plots of the sampling density of a) the unaccelerated and the 2-fold-accelerated spiral trajectories; and b) the unaccelerated and the 2-fold-accelerated radial trajectories. The unaccelerated trajectories maintain a sampling density greater than 1 everywhere – a Nyquist-like requirement. At twofold acceleration, the outer part of *k*-space becomes undersampled. However, the center of *k*-space is sufficiently sampled up to *k*=55 and *k*=110, for spiral and radial trajectories respectively. Note that a sampling density of 1 corresponds to a *k*-space separation of 2π/Field Of View.

2.2.d Image Reconstruction

Following the extraction of internal sensitivity maps, we performed parallel image reconstruction based on the conjugate-gradient (CG) matrix inversion approach of non-Cartesian SENSE (5), in which the generalized encoding matrix equation (Eq. [1.14]) is modified,

$$\left(\mathbf{E}^H \boldsymbol{\Psi}^{-1} \mathbf{E}\right) \boldsymbol{\rho} = \mathbf{E}^H \boldsymbol{\Psi}^{-1} \mathbf{s} \qquad [2.6]$$

and then solved iteratively. Here, $(\cdot)^H$ indicates a Hermitian transpose, and $(\cdot)^{-1}$ indicates a matrix inverse. $\boldsymbol{\Psi}$ is the sample noise covariance matrix (Eq. [1.42]) , $\boldsymbol{\rho}$ is a vector of image voxel values (Eq. [1.13]), $\mathbf{s}$ is a vector of measured signal values for parallel MRI (Eq. 1.30]), and the encoding matrix $\mathbf{E}$ has elements

$$\mathbf{E}_{(\kappa,l),\gamma} = e^{i\mathbf{k}_\kappa \mathbf{r}_\gamma} C_l(\mathbf{r}_\gamma) \qquad [2.7]$$

where $C_l(\mathbf{r}_\gamma)$ is the sensitivity of coil l at the center position $\mathbf{r}_\gamma$ of the γ^{th} image voxel. As demonstrated in Ref (5) and also in Section 1.3.d.3, the noise covariance matrix can be readily eliminated by creating a set of virtual receiver channels of zero noise correlation:

$$\begin{aligned} \mathbf{s}^{decorr} &= \mathbf{L}^{-1}\mathbf{s} \\ \mathbf{E}^{decorr} &= \mathbf{L}^{-1}\mathbf{E} \end{aligned} \qquad [2.8]$$

where the matrix $\mathbf{L}$ is obtained by Cholesky decomposition of $\boldsymbol{\Psi}$:

$$\boldsymbol{\Psi} = \mathbf{L}\mathbf{L}^H \qquad [2.9]$$

After substitution with Eq. [2.8] and dropping the superscript for decorrelation, Eq. [2.6] is simplified to:

$$\left(\mathbf{E}^H \mathbf{E}\right) \boldsymbol{\rho} = \mathbf{E}^H \mathbf{s} \qquad [2.10]$$

The noise decorrelation only needs to be performed once on the received MR signal data. The corresponding matrix E, formed by sensitivities extracted from the decorrelated data, has conveniently incorporated the effect of the multiplication of $\mathbf{L}^{-1}$, eliminating the need to perform an explicit matrix multiplication $\mathbf{L}^{-1}\mathbf{E}$.

In this work, the δ–criterion of convergence was set to 0.025 (Ref. (5), Appendix C). The matrix-vector multiplication on the right-hand side of Eq. [2.10] was accomplished using

the regridding procedure described in Ref. (5), which takes advantage of the harmonic terms in the encoding matrix to accelerate the computation. In lieu of repeated ungridding and regridding for the iterated multiplication on the left-hand side, the convolution approach described in (11) was used. This approach identifies a convolution kernel G in the multiplication by the composite matrix $\mathbf{E}^H\mathbf{E}$:

$$\begin{aligned}\left(\mathbf{E}^H\mathbf{E}\boldsymbol{\rho}\right)_\gamma &= \sum_l C_l^*(\mathbf{r}_\gamma)\sum_{\gamma'}\left(\sum_\kappa e^{-i\mathbf{k}_\kappa\left(\mathbf{r}_\gamma-\mathbf{r}_{\gamma'}\right)}\right)C_l(\mathbf{r}_{\gamma'})\boldsymbol{\rho}_{\gamma'} \\ &= \sum_l C_l^*(\mathbf{r}_\gamma)\left[\mathrm{G}\otimes\left(C_l\mathbf{s}\right)\right]_\gamma\end{aligned} \qquad [2.11]$$

The convolution kernel $\mathrm{G}(\mathbf{r}) = \sum_\kappa e^{-i\mathbf{k}_\kappa\mathbf{r}}$ is calculated once by gridding onto a Cartesian matrix twice the size of the target image in each dimension. The multiplication in Eq. [2.11] is then carried out by multiplying each trial image pixel by the corresponding pixel value of each coil sensitivity in turn, performing a Cartesian convolution with the kernel, multiplying again by the complex conjugate of the coil sensitivity, and summing over all coils. Some evidence exists that a tailored gridding-ungridding approach can outperform this convolution algorithm (12); however, the convolution approach was found to be efficient and easily coded in MATLAB (The Mathworks, Natick, MA) for our reconstructions.

Acquisition of a separate body coil image for determination of pure coil sensitivities $C_l(\mathbf{r}_\gamma)$ would defeat the purpose of self-calibration. Instead, the reference images extracted from the *k*-space center, as described in the previous section, were used directly for the multiplications in Eq. [2.11]. Following the conclusion of conjugate gradient iterations, the reconstructed image was postmultiplied by the sum of squares of these reference images to yield the final result. It has been demonstrated previously (4,13) that use of uncorrected low-resolution reference images followed by postmultiplication eliminates all dependence upon the underlying magnetization density in the reference images, and the same result may easily be shown to hold in the current case. Images formed using this approach will have the same appearance as images formed using relative coil sensitivities divided beforehand by the sum of squares of the reference images, but the potentially numerically unstable step of pixelwise division is avoided.

Fig. 2.3 summarizes the overall strategy of the self-calibrated non-Cartesian SENSE algorithm used in this work. For comparison with parallel image reconstructions, unaccelerated and accelerated signal data were reconstructed to a 512x512 in-plane image matrix using a standard gridding algorithm with a Kaiser-Bessel kernel of width=3 and β=13.9086 (Table 2 of Ref. (10)). A sum-of-squares combination was performed on the gridded component coil images. Self-calibrated parallel image reconstructions were also compared with externally calibrated parallel image reconstructions, in order to assess the accuracy of the extracted internal sensitivities. The external sensitivity maps were fully-sampled but low-resolution *in vivo* images obtained from separate acquisitions.

SECTION 2.3 Results

Fig. 2.4 compares two-fold accelerated reconstructions using the gridding method (a: spiral, d: radial), the parallel imaging method with self-calibrated sensitivity (b: spiral, e: radial) and the parallel imaging method with external sensitivity (c: spiral, f: radial). Simple regridding of the undersampled spiral acquisition (Fig. 2.4a) resulted, as expected, in appreciable spiral aliasing artifacts, which were removed by parallel image reconstructions using self-calibrated sensitivity (Fig. 2.4b) and external sensitivity (Fig. 2.4c). For the radial trajectory, only subtle radial streak artifacts (which appeared as pseudo-noise) were visible with simple regridding at two-fold acceleration (Fig. 2.4d). This reflects the well-known robustness of radial trajectories to undersampling. Both parallel image reconstructions using self-calibrated sensitivity (Fig. 2.4e) and external sensitivity (Fig. 2.4f) reduced these streak artifacts and preserved the high image quality. The numbers at the bottom right corner of the images in Fig. 2.4b, c, e, and f indicate iteration counts to reach the convergence criterion.

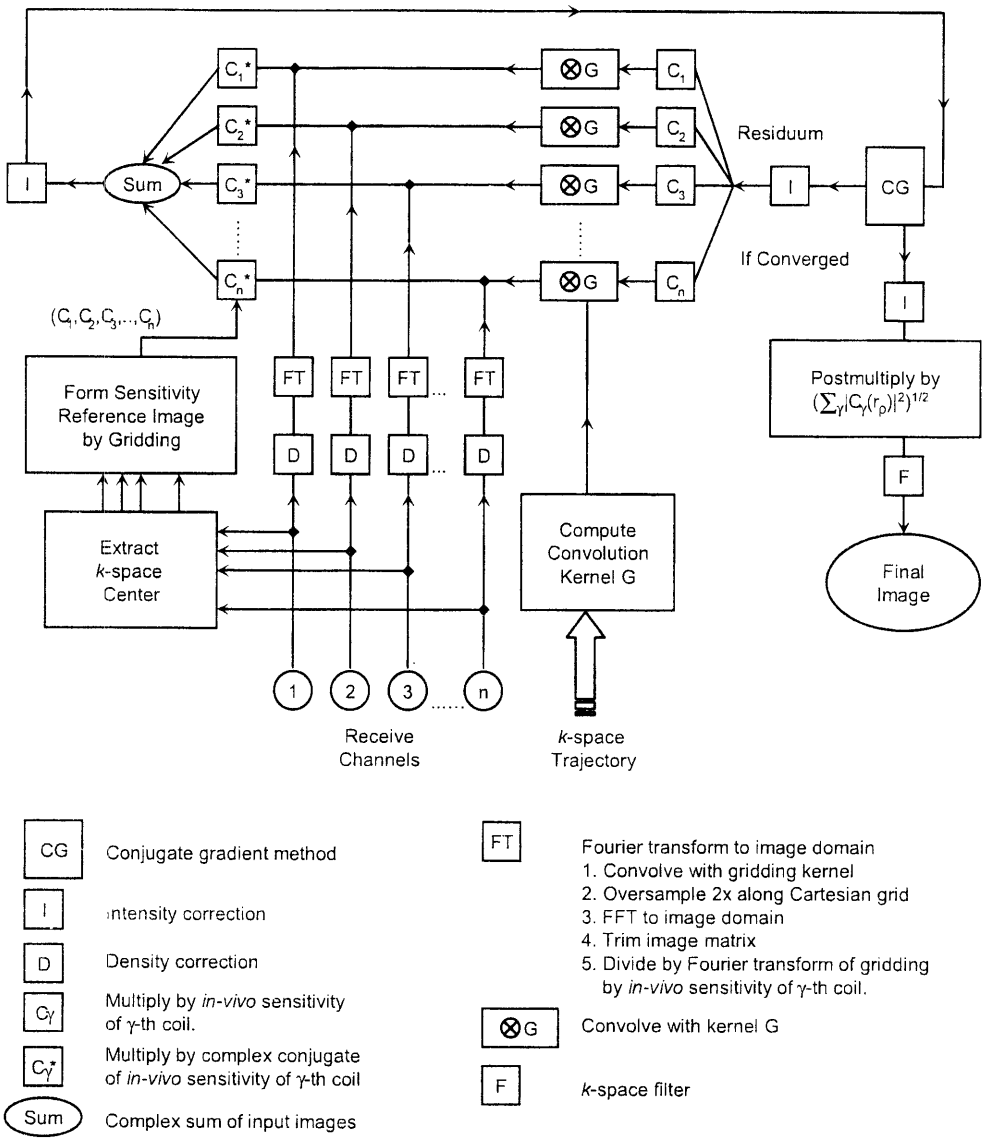

FIGURE 2.3 Schematic of Self-Calibrating CG-SENSE Algorithm

Summary of the algorithm for self-calibrated non-Cartesian parallel image reconstructions. The CG-SENSE algorithm described in (5) uses a separately acquired sensitivity reference. In our self-calibrating approach, *in vivo* sensitivity maps are extracted from the densely-sampled k-space and are used in place of the external reference. An additional post-multiplication step is required in the self-calibrated case to remove underlying magnetization density in the extracted sensitivity references.

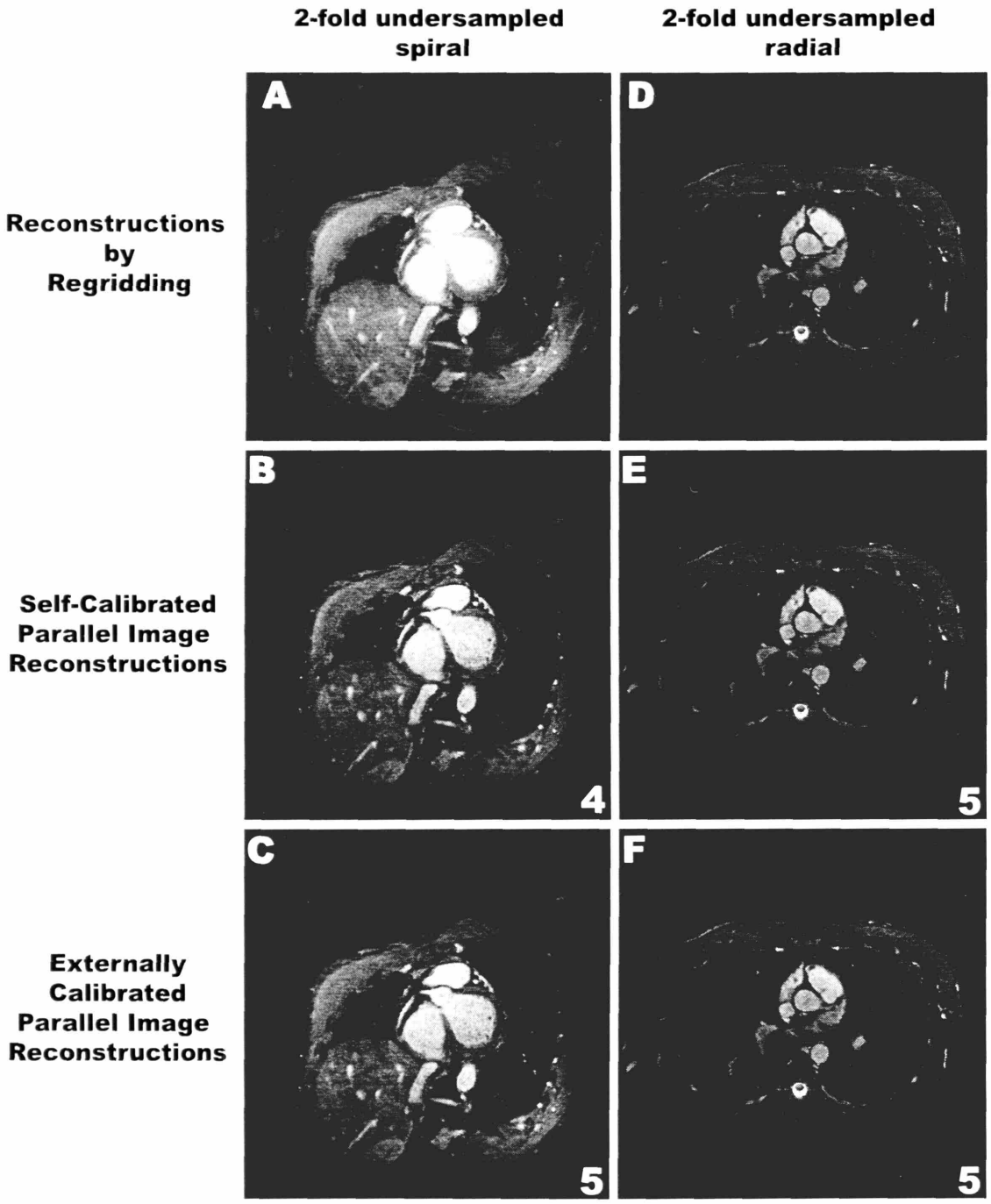

FIGURE 2.4 2x Self-calibrated and External Calibrated Spiral and Radial Images

Two-fold accelerated in vivo images showing the right (a-c) and the left main (d-f) coronary artery in a healthy adult subject. a,d) spiral (a) and radial (d) images reconstructed with a convolution-based gridding method without any parallel

reconstruction algorithm; b,e) spiral (b) and radial (e) images reconstructed using self-calibrated parallel imaging; c,f) spiral (c) and radial (f) images reconstructed using externally-calibrated parallel imaging. The streaking artifacts in panels a and d, which result from azimuthal undersampling, are noticeably reduced in panels b, c, e and f. Moreover, the image quality of self-calibrated parallel image reconstructions (b) and (e) is comparable with externally-calibrated counterparts (c) and (f), respectively. The numbers at the bottom right corner of the images in panels b, c, e, and f indicate iteration counts to reach the convergence criterion.

Fig. 2.5 compares image intensity profiles taken from the central horizontal lines (line number 256 of 512) of images reconstructed by the conventional gridding method and the self-calibrating parallel imaging method for twofold accelerated spiral (a) and twofold accelerated radial (b) trajectories. Parallel imaging results in different types of image quality improvement for spiral and radial datasets. For the undersampled spiral datasets (Fig. 2.5a), the self-calibrated parallel image reconstruction shows higher spatial resolution that the regridded counterpart (e.g. notice the sharper peak near location 230). For the undersampled radial datasets (Fig. 2.5b), the self-calibrated parallel image reconstruction shows decreased pseudo-noise background in noise-dominated regions. Higher levels of undersampling, perhaps with larger numbers of array elements, will clearly be required to make best use of parallel imaging to remove more substantial streaking artifacts.

Fig. 2.6 shows a comparison of unaccelerated spiral (a) and radial (d) images with self-calibrated parallel image reconstructions at various acceleration factors. Apart from the expected SNR loss compared to the unaccelerated image, the 2- and 3-fold accelerated spiral images (Fig. 2.5b and c) and radial images (Fig. 2.5e and f) show preserved image quality for depiction of the right and left coronary arteries. Once again, the numbers in selected images indicate iteration counts to reach the convergence criterion.

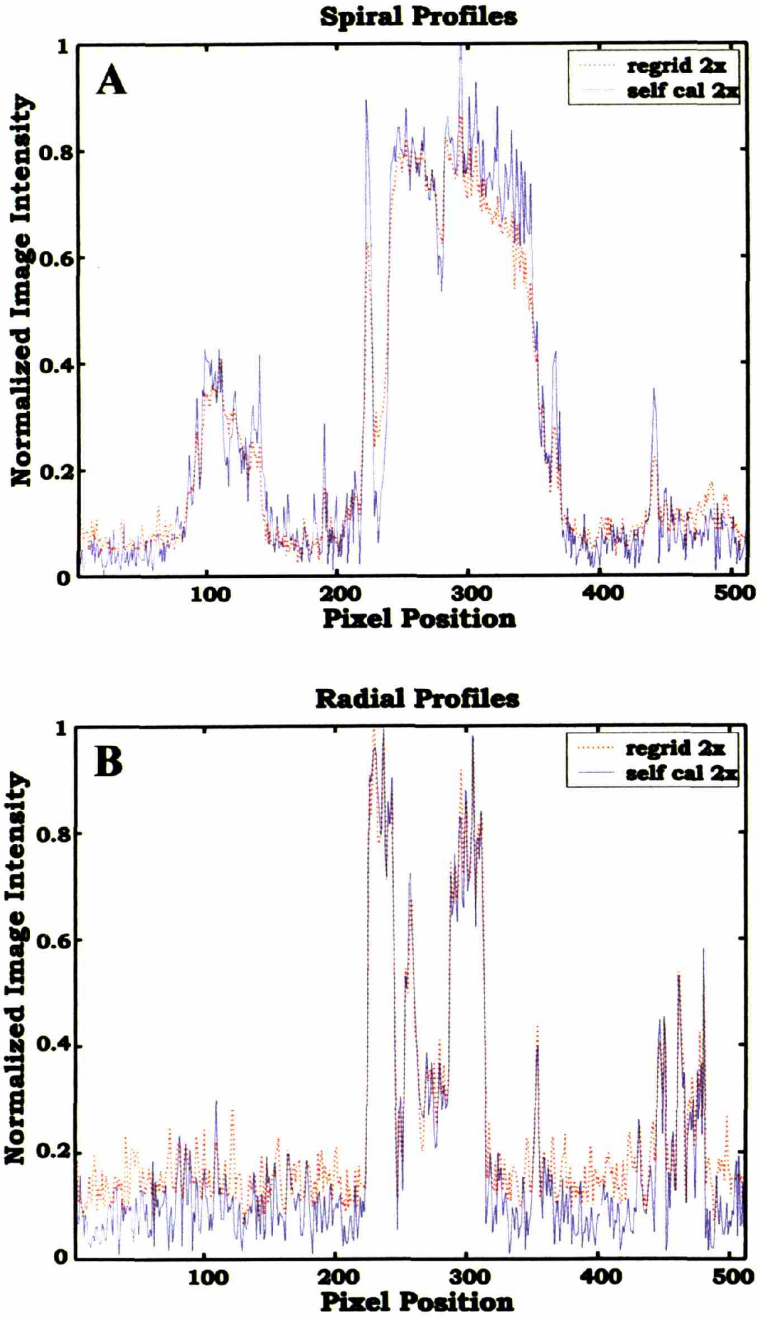

FIGURE 2.5 Image Intensity Profiles of 2x Spiral and Radial Images

Image intensity profiles taken from the central horizontal lines of images reconstructed from twofold undersampled spiral (a) and radial (b) datasets. Reconstruction with a convolution-based gridding method is shown by the grey line, and that of self-calibrated parallel imaging is shown by the black line.

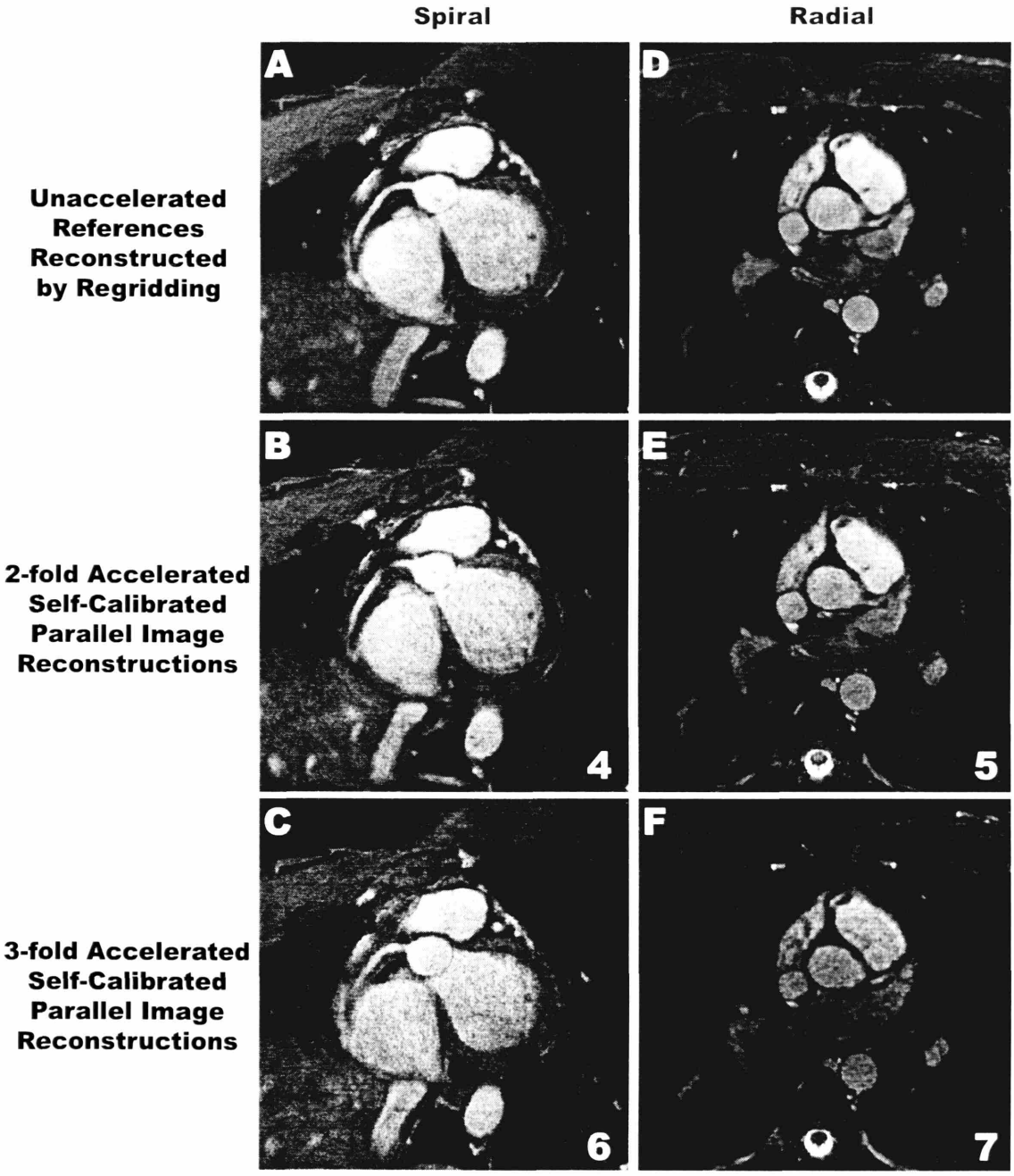

FIGURE 2.6 2x and 3x Spiral and Radial Parallel Image Reconstructions

Details from *in vivo* images comparing various acceleration factors. a,d) unaccelerated reference spiral (a) and radial (d) images. b,e) 2-fold accelerated spiral (b) and radial (e) images using self-calibrated parallel imaging; c,f) 3-fold accelerated spiral (c) and 3-fold accelerated radial (f) images using self-calibrated parallel imaging. The numbers at the bottom right corner of the images in panels b, c, e, and f indicate iteration counts to reach the convergence criterion.

SECTION 2.4 Discussion

These initial results demonstrate the potential of self-calibrated non-Cartesian parallel imaging as a viable means of obtaining accelerated datasets, for example for high-quality coronary MR angiography. Such an approach is time-efficient (requiring no more time than the undersampled acquisition itself), and excludes the potential for geometry mismatches that can hamper traditional parallel imaging calibrations.

In this work, an iterative non-Cartesian SENSE algorithm was used to illustrate the principle and demonstrate the feasibility of inherent self-calibration. Alternative algorithms such as PARS (14), SMASH (15), or GRAPPA (16) may also be used.

2.4.a Criteria for Sensitivity Extraction from Undersampled Trajectories

Apart from an intrinsic SNR loss, the principal constraint on acceleration factors achievable with inherently self-calibrated non-Cartesian parallel imaging is related to the spatial frequency content of the coil sensitivities. First of all, the central region of Nyquist or greater k-space density must extend far enough to represent faithfully the spatial variations of coil sensitivities. A more subtle constraint, which might manifest itself at higher accelerations, may be appreciated from the schematic trajectories in Fig. 2.1: the maximum separation Δk_{max} of the sampling points in the outer region must be smaller than the radius $k_{Nyquist}$ of the fully-sampled central region. ($\Delta k_{max} \leq k_{Nyquist}$) Since the extracted coil sensitivities by definition will have no spatial frequency content beyond $k_{Nyquist}$, they cannot be used to span distances in k-space larger than $k_{Nyquist}$ without introducing imperfections into the reconstruction. The balance of $k_{Nyquist}$ and Δk_{max} is determined by the level of undersampling (see Fig. 2.1), and this balance constitutes an additional limit on the degree of acceptable undersampling.

For low acceleration factors where $k_{Nyquist}$ is adequately larger than Δk_{max}, a user-defined sensitivity extraction cutoff k_{cutoff} may be flexibly chosen such that:

$$\Delta k_{max} \leq k_{cutoff} \leq k_{Nyquist} \qquad [2.12]$$

As illustrated in Fig. 2.4, the self-calibrating parallel image reconstructions and the externally calibrated reconstructions have comparable image quality, despite the difference in the method and resolution of the sensitivity calibration. Qian et al (17) have recently studied the effect of k-space cutoff on reconstructed image quality for self-calibrated spiral trajectories, finding that an optimum cutoff could be defined for particular trajectories and image content. Their reported optima occurred at substantially lower values of k_{cutoff} than were used here, but the error minima were comparatively broad for *in vivo* imaging situations. Thus, in general, once the criterion imposed by Eq. [2.12] is satisfied, fine-tuning for an optimal k_{cutoff} may not yield much added benefit, though this remains a subject for further study. Other implementation-specific considerations (e.g. speed and memory, error tolerance of extraction method) may favor one value of k_{cutoff} over others.

For the spiral trajectory employed in this work, there is sufficient central *k*-space density to reconstruct *in vivo* sensitivity maps of matrix size 18x18 at an acceleration factor of two. Other than omitting spiral interleaves, no pulse sequence modifications were required, since the principal spatial variations in coil sensitivities are typically well-represented at this level of spatial resolution. However, at a higher acceleration factor of 3, the fully-sampled central region is reduced in size to 10x10. At an even higher acceleration, the region of sufficient sampling may become so small that the low-resolution sensitivity maps may no longer adequately represent the actual coil sensitivities, while at the same time the size of the fully sampled region may begin to approach the maximum *k*-space separation. Therefore, for self-calibrated spiral acquisitions with higher acceleration factors, trajectory modification may be necessary to ensure that the sufficiently sampled region of *k*-space is large enough to represent the low-resolution coil sensitivities. Variable-density spiral trajectories (18), though not originally proposed for applications related to parallel imaging, may be a good match for self-calibrated non-Cartesian parallel imaging.

For radial trajectories, because of the even more densely-sampled center, *in vivo* sensitivity maps of sizes 40x40 and 25x25 were extracted for acceleration factors of 2 and 3,

respectively. Accurate sensitivity maps can be extracted from datasets with even higher accelerations without modification of the trajectories.

2.4.b Effect of Parallel Imaging on Different Non-Cartesian Trajectories

Non-Cartesian parallel imaging, irrespective of the sensitivity calibration method, offers different qualitative improvements for different non-Cartesian trajectories. Even though the focus of this work is not to evaluate the effectiveness of parallel imaging on various non-Cartesian trajectories, preliminary observations can be made from Fig. 2.4 and 5. For the twofold undersampled spiral trajectory, the image reconstructed by the gridding method shows both considerable aliasing artifacts (Fig. 2.4a) and reduction in image resolution (Fig. 2.5a). Parallel imaging is effective in both removing the artifacts (Fig. 2.4b and 2.4c) and improving the image resolution (Fig. 2.5a).

For the twofold undersampled radial trajectory, the image reconstructed by the gridding method (Fig. 2.4d and 2.5b) has an elevated pseudo-noise background due to radial streaking artifacts but the image resolution is otherwise unaffected. This preservation of image resolution in the signal-rich region comes at the expense of increased artifacts in the noise-dominated region. Given the relative robustness of radial trajectories subjected to undersampling, there is less room for improvement in the signal-rich region for parallel imaging. In fact, Fig. 2.5b shows an almost perfect tracking in the central region between the image profiles of the gridding method and the self-calibrated parallel imaging method. However, in the noise-dominated regions, parallel imaging shows an appreciable reduction of pseudo-noise (Fig 3.4e, 3.4f and 3.5b).

It should be noted that even with nominally fully-sampled non-Cartesian trajectories, residual aliasing artifacts may remain due to inherent constraints in the traditional regridding procedure (10). Self-calibrated parallel imaging, without the burden of acquiring a separate sensitivity reference, can readily be used to reduce these residual alasing artifacts.

While the current work has focused on exploring the desirable properties of spiral and radial trajectories, analogous benefits may be expected, in general, for any arbitrary trajectory containing a sufficiently densely sampled *k*-space center.

SECTION 2.5 Conclusions

Preliminary results from *in vivo* image reconstructions demonstrate that self-calibrated spiral and radial parallel imaging are feasible, allowing accelerated high-resolution scans without the acquisition of any additional calibration data. Accelerated 3D coronary MR angiography studies were demonstrated here. The intrinsic self-calibrating nature of spiral and radial trajectories also makes them a natural choice for dynamic imaging applications, body screening studies, or other areas in which traditional sensitivity calibrations must contend with physiologic motion.

SECTION 2.6 Future Directions

A logical extension of this self-calibrating work is to determine the theoretical minimal requirements for sensitivity calibration information. The minimal calibration requirements for existing self-calibrating techniques have already been clearly stated in Section 2.5. However, it is conceivable that an unconventional self-calibrating approach may require less or even no sensitivity calibration. Two plausible approaches, one linear and one non-linear, are discussed here for future explorations.

2.6.a Recursive Auto-calibration with N^{th} Order Root

In SMASH and related parallel imaging methodologies, omitted signal data $s_l(\mathbf{k}+\Delta\mathbf{k})$ are reconstructed by a linear combination of signal data acquired at a nearby *k*-space neighbor $s_l(\mathbf{k})$:

$$s_l(\mathbf{k}+\Delta\mathbf{k}) \approx \sum_{l'} w_{l,l'}^{(\Delta\mathbf{k})} s_{l'}(\mathbf{k}). \qquad [2.13]$$

The complex weights, $w_{l,l'}^{(\Delta\mathbf{k})}$ (denoted by the superscript $^{(\Delta\mathbf{k})}$ for a particular *k*-space separation), are computed from the coil sensitivities by performing a least-squares fit:

$$C_l(\mathbf{r})e^{i\Delta\mathbf{k}\cdot\mathbf{r}} \approx \sum_{l'} w_{l,l'}^{(\Delta\mathbf{k})} C_{l'}(\mathbf{r}). \qquad [2.14]$$

This relationship can be expressed in matrix form,

$$\begin{aligned} \mathbf{CD}^{(\Delta\mathbf{k})} &= \mathbf{W}^{(\Delta\mathbf{k})}\mathbf{C} \\ \mathbf{W}^{(\Delta\mathbf{k})} &= \mathbf{CD}^{(\Delta\mathbf{k})}\mathbf{C}^H\left(\mathbf{CC}^H\right)^{-1} \end{aligned} \qquad [2.15]$$

where the entries of **C** , **D,** and **W** are defined as follows,

$$\begin{aligned} C_{l,\gamma} &= C_l(\mathbf{r}_\gamma) \\ D_{\gamma\gamma}^{(\Delta\mathbf{k})} &= e^{i\Delta\mathbf{k}\cdot\mathbf{r}_\gamma} \\ W_{l,l'}^{(\Delta\mathbf{k})} &= w_{l,l'}^{(\Delta\mathbf{k})} w_{l,l'} \end{aligned} \quad . \qquad [2.16]$$

It has been speculated (19) that by recursively applying Eq. [2.13], a series of omitted signal data at equidistant *k*-space interval can be reconstructed:

$$s_l(\mathbf{k}+n\Delta\mathbf{k}) \approx \sum_{l''} w_{l,l''}^{(\Delta\mathbf{k})} \sum_{l''^{-1}} w_{l'',l''^{-1}}^{(\Delta\mathbf{k})} \cdots \sum_{l'} w_{l'',l'}^{(\Delta\mathbf{k})} s_{l'}(\mathbf{k}). \qquad [2.17]$$

In matrix form, this would imply that the knowledge of the weight matrix **W** for a particular **Δk** would allow the computation for weight matrices for arbitrary *n***Δk**,

$$\mathbf{W}^{(n\Delta\mathbf{k})} = \left(\mathbf{W}^{(\Delta\mathbf{k})}\right)^n. \qquad [2.18]$$

If Eq. [2.18] were true, it would have two very dramatic implications. First, this would potentially allow an indefinite number of recursive reconstructions, and MR data acquired at a single *k*-space location could reconstitute an entire dataset. This would violate the spirit that the number of observations must be greater than the number of unknowns for any invertible system. However, a potential explanation of the paradox of Eq. [2.18] would be that since the data reconstruction is only a least-squares fit (as indicated by the approximate equality in Eqs. [2.13] and [2.14]), error propagation and amplification would prevent an indefinite recursive reconstruction. The use of a small number of recursions ($n = 2$) has been reported (19).

The second implication comes from a minor rearrangement of Eq. [2.18], that a lower order **W** could be computed by taking the n^{th} root of a higher order **W**,

$$\mathbf{W}^{(\Delta \mathbf{k})} = \sqrt[n]{\mathbf{W}^{(n\Delta \mathbf{k})}} . \qquad [2.19]$$

This would be especially attractive for an undersampled trajectory which was not typically self-calibrating. For example, in a regularly twofold undersampled dataset, the weight matrix for the 1st spatial harmonic $\mathbf{W}^{(+1)}$ would be required for parallel image reconstruction. If Eq. [2.19] were true, then $\mathbf{W}^{(+1)}$ could be computed by taking the square root of $\mathbf{W}^{(+2)}$,

$$\mathbf{W}^{(+1)} = \sqrt{\mathbf{W}^{(+2)}} . \qquad [2.20]$$

The remaining uncertainties would be the signs of the eigenvalues of $\mathbf{W}^{(+1)}$, which could be determined by adding a very small amount of *a priori* information (20).

A closer examination of Eq. [2.15], however, suggests that neither Eqs. [2.18] or [2.19] could be true in general. In a simple case that $n = 2$ and $\Delta\mathbf{k} = +1$,

$$\begin{aligned} \mathbf{W}^{(+1)} &= \mathbf{C}\mathbf{D}^{(+1)}\mathbf{C}^{H}\left(\mathbf{C}\mathbf{C}^{H}\right)^{-1} \\ \left(\mathbf{W}^{(+1)}\right)^{2} &= \mathbf{C}\mathbf{D}^{(+1)}\mathbf{C}^{H}\left(\mathbf{C}\mathbf{C}^{H}\right)^{-1}\mathbf{C}\mathbf{D}^{(+1)}\mathbf{C}^{H}\left(\mathbf{C}\mathbf{C}^{H}\right)^{-1} \end{aligned} \qquad [2.21]$$

and

$$\mathbf{W}^{(+2)} = \mathbf{C}\mathbf{D}^{(+2)}\mathbf{C}^{H}\left(\mathbf{C}\mathbf{C}^{H}\right)^{-1} . \qquad [2.22]$$

In a special case that,

$$\mathbf{C}^{H}\left(\mathbf{C}\mathbf{C}^{H}\right)^{-1}\mathbf{C} = \mathbf{I} , \qquad [2.23]$$

then

$$\begin{aligned} \left(\mathbf{W}^{(+1)}\right)^{2} &= \mathbf{C}\mathbf{D}^{(+1)}\mathbf{C}^{H}\left(\mathbf{C}\mathbf{C}^{H}\right)^{-1}\mathbf{C}\mathbf{D}^{(+1)}\mathbf{C}^{H}\left(\mathbf{C}\mathbf{C}^{H}\right)^{-1} \\ &= \mathbf{C}\mathbf{D}^{(+1)}\mathbf{D}^{(+1)}\mathbf{C}^{H}\left(\mathbf{C}\mathbf{C}^{H}\right)^{-1} \\ &= \mathbf{C}\mathbf{D}^{(+2)}\mathbf{C}^{H}\left(\mathbf{C}\mathbf{C}^{H}\right)^{-1} \\ &= \mathbf{W}^{(+2)} \end{aligned} \qquad [2.24]$$

where

$$\mathbf{D}^{(+2)} \equiv \mathbf{D}^{(+1)}\mathbf{D}^{(+1)} . \qquad [2.25]$$

However, unless **C** happened to be an invertible square matrix which allows the distribution of the inverse within the parenthesis in Eq. [2.23], the relationship remains an inequality in general,

$$\mathbf{C}^H \left(\mathbf{C}\mathbf{C}^H\right)^{-1} \mathbf{C} \neq \mathbf{I}. \qquad [2.26]$$

Then again, $\mathbf{C}^H \left(\mathbf{C}\mathbf{C}^H\right)^{-1} \mathbf{C}$ may only need to be approximately equal to the identity matrix to allow the n^{th} root operation in Eq. [2.20]. Early attempts at calibration-free parallel image reconstructions as part of this thesis work met with limited success, and, despite the subsequent claims advanced by another group in recent conferences (e.g., (19)), it has yet to be shown rigorously how to guarantee such an approximation without obtaining explicit knowledge of **C**.

2.6.b Nonlinear Search for Parameterized Coil Sensitivity

A non-linear iterative approach for calibration-free parallel image reconstruction has also being tested as part of this thesis work, but definitive conclusions are deferred to future studies. In this approach, some a priori information about coil geometry was incorporated into coil models from which coil sensitivities could be calculated using a finite set of parameters, and a non-linear search was performed within the possible range of the parameter values. An evaluation function was used to quantify the degree of self consistency of the calculated sensitivities against the undersampled dataset. Starting with rigid coil arrays, the location and conductor geometry of the array would be pre-determined. Coil sensitivities could be computed using the Biot-Savart law and the principle of reciprocity. The assumption of rigidity could be relaxed to accommodate flexible or otherwise mobile coil arrays, and in this case additional search parameters would be required to specify the position of each coil element and/or the curvature due coil bending.

Nonlinear searches are in general computationally intensive and may not yield unique solutions. However, the ability to perform entirely calibration-free parallel imaging is increasingly appealing especially for highly accelerated studies in which calibration time

becomes a significant portion of the overall examination time. Thus, the search for nonlinear self-calibrating approaches is likely to continue in times to come.

Chapter 2 References

1. Jakob PM, Griswold MA, Edelman RR, Sodickson DK. AUTO-SMASH: a self-calibrating technique for SMASH imaging. SiMultaneous Acquisition of Spatial Harmonics. Magma 1998;7(1):42-54.
2. Heidemann R, Griswold M, Haase A, Jakob PM. VD-AUTO-SMASH Imaging. Magn Reson Med 2001;45:1066-1074.
3. Griswold MA, Jakob PM, Heidemann RM, Nittka M, Jellus V, Wang J, Kiefer B, Haase A. Generalized autocalibrating partially parallel acquisitions (GRAPPA). Magn Reson Med 2002;47(6):1202-10.
4. McKenzie CA, Yeh EN, Ohliger MA, Price MD, Sodickson DK. Self calibrating parallel imaging with automatic coil sensitivity extraction. Magn Reson Med 2002;47:529-538.
5. Pruessmann KP, Weiger M, Bornert P, Boesiger P. Advances in sensitivity encoding with arbitrary k-space trajectories. Magn Reson Med 2001;46:638-651.
6. Bornert P, Stuber M, Botnar RM, Kissinger KV, Koken P, Spuentrup E, Manning WJ. Direct comparison of 3D spiral vs. Cartesian gradient-echo coronary magnetic resonance angiography. Magn Reson Med 2001;46(4):789-94.
7. Irarrazabal P, Nishimura DG. Fast three dimensional magnetic resonance imaging. Magn Reson Med 1995;33(5):656-62.
8. Leiner T, van Yperen G, Eggers H, Yeh EN, Kissinger KV, Katsimaglis G. A Novel Real-Time R-Wave Gating Algorithm for Detection of Heart Rate Variability: Impact on Free-Breathing, Navigator Gated Coronary Artery Imaging. In: Proc. 12th Annual Meeting ISMRM, Toronto, Canada, 2003.
9. Bornert P, Schomberg H, Aldefeld B, J. G. Improvements in spiral MR imaging. Magma 1999;9:29-41.
10. Jackson JI, Meyer CH, Nishimura D, Macovski A. Selection of a convolution function for Fourier inversion using gridding. IEEE Trans Med Imaging 1991;10(3):473-478.
11. Wajer FTAW, Pruessmann KP. Major Speedup of Reconstruction for Sensitivity Encoding with Arbitrary Trajectories. In: Proc. 9th Annual Meeting ISMRM, Glasgow, Scotland, 2001. p 767.

12. Eggers H, Boernert P, Boesiger P. Comparison of Gridding- and Convolution-Based Iterative Reconstruction Algorithms For Sensitivity-Encoded Non-Cartesian Acquisitions. In: Proc. 10th Annual Meeting ISMRM, Honolulu, Hawaii, USA, 2002. p 743.
13. Sodickson DK, McKenzie C. A generalized approach to parallel magnetic resonance imaging. Med Phys 2001;28(8):1629-1643.
14. Yeh EN, McKenzie CA, Lim D, Ohliger MA, Grant AK, Willig J, Rofsky NM, Sodickson DK. Parallel imaging with Augmented Radius in k-Space (PARS). In: Proc 10th Annual Meeting ISMRM, Honolulu, Hawaii USA, 2002. p 2399.
15. Lee RF, Hardy CJ, Bottomley PA. Radial SMASH for Parallel Back Projection Reconstruction MRI. In: Proc. 11th Annual Meeting ISMRM, Toronto, Canada, 2003. p 2350.
16. Griswold M, Heidemann R, Jakob PM. Direct Parallel Imaging Reconstruction of Radially Sampled Data using GRAPPA with Relative Shifts. In: Proc. 11th Annual Meeting ISMRM, Toronto, Canada, 2003. p 2349.
17. Qian Y, Zhang Z, Stenger VA, Wang Y. Self-calibrated spiral SENSE. Magn Reson Med 2004;52(3):688-92.
18. Sussman MS, Stainsby JA, Robert N, Merchant N, Wright GA. Variable-density adaptive imaging for high-resolution coronary artery MRI. Magn Reson Med 2002;48(5):753-64.
19. Griswold M, Heidemann R, Jakob PM. The GRAPPA Operator. In: Proc. 11th Annual Meeting ISMRM, Toronto, Canada, 2003. p 2348.
20. Blaimer M, Breuer F, Heidemann R, Muller M, Griswold M. Is Parallel MRI Without a Priori Information Possible? In: Proc. 12th Annual Meeting ISMRM, Kyoto, Japan, 2004. p 2416.

CHAPTER 3. IMAGE RECONSTRUCTION WITH *k*-SPACE LOCALITY CONSTRAINT[9]

This chapter is devoted to the development of a stable and efficient algorithm for solving the matrix inversion for the generalized MR equation, $\mathbf{s} = \mathbf{E}\boldsymbol{\rho}$, especially in the general case when a direct matrix inversion of $\mathbf{E}$ is neither desirable nor feasible.

SECTION 3.1 Introduction

There are two practical challenges in the direct inversion of the generalized encoding matrix $\mathbf{E}$. First, this matrix inversion can be memory- and computation-intensive, particularly for non-Cartesian MR signal data. Second, at high acceleration factors, the encoding matrix becomes poorly conditioned, making the inversion numerically unstable, and therefore leading to high noise amplification.

In the special case when datasets are Cartesian sampled in at least one direction, it is possible to reduce the memory and computational burden of the encoding matrix inversion

[9] The work in this chapter has been adapted for publication as "Yeh EN, McKenzie CA, Ohliger MA, Sodickson SK. Parallel magnetic resonance imaging with Adaptive Radius in *k*-Space (PARS): Constrained Image Reconstruction using *k*-space Locality in Radiofrequency Coil Encoded Data. Mag Reson Med. (In Press)"

by applying a fast Fourier transform (FFT) in the Cartesian sampled directions (1-4). For other more general trajectories, a simple FFT cannot be applied; instead, an iterative approach using conjugate gradient techniques and gridding has been proposed (5).

In an effort to improve numerical stability, matrix regularization methods are commonly used. However, many of these methods – for example, truncation of unstable singular values in a singular value decomposition (SVD) – are themselves memory- and computation-intensive, potentially annulling the advantages provided by the iterative approach.

Parallel magnetic resonance imaging with Adaptive Radius in *k*-Space (PARS) (6), the technique to be described in this work, provides a simultaneous solution to these two challenges by efficiently inverting the encoding matrix while ensuring numerical stability. In PARS, omitted signal data are reconstructed using only acquired signal data that lie within a small (and adjustable) radius in *k*-space from each omitted signal datum. A localized encoding matrix is created and inverted, and the omitted data are reconstructed locally. This process is repeated for each missing *k*-space location until a complete dataset is reconstructed.

Instead of reconstructing the complete dataset with a direct matrix inversion, PARS performs point-by-point data reconstruction by inverting many small matrices. As a result, it eliminates the need to store and manipulate the prohibitively large encoding matrix. The independent matrix inversions allow the computation to be easily distributed across a parallel computing environment. More importantly, PARS explicitly uses the physical principle of *k*-space locality, which asserts that in the reconstruction of an omitted datum, the contribution of other signal data diminishes as a function of the *k*-space separation between the omitted point and the signal data used in the reconstruction. PARS efficiently eliminates the less relevant data and their corresponding signal equations, thereby improving the conditioning of the localized encoding matrices. This matrix regularization, unlike mathematically-based approaches such as truncated SVD, is founded upon a physical property of RF coils. While previous parallel imaging techniques have either implicitly or explicitly used *k*-space locality

(3,7-10), the PARS implementation with an adaptive *k*-space radius allows an intuitive and flexible handle to harness *k*-space locality.

Preliminary implementations of PARS have been described, with a minimum of methodological detail, in a recent clinical comparative study (11). In this work, we provide a full theoretical description of the PARS technique. We formulate the algorithm using the perspective of *k*-space locality, and propose an empirical approach to establish a suitable *k*-space radius. Next we report the results of phantom and *in vivo* experiments using PARS on undersampled Cartesian datasets. Images reconstructed using PARS are compared to those reconstructed with SMASH and SENSE techniques. In addition, we use PARS to reconstruct undersampled spiral datasets to illustrate the versatility of the technique in handling multi-dimensionally accelerated non-Cartesian datasets. Lastly, we discuss how PARS is related to other traditional and parallel image reconstruction techniques in order to characterize the associated tradeoffs between Signal-to-Noise Ratio (SNR) and residual aliasing artifact.

SECTION 3.2 Theory

As a review of Eq. [1.30], the MR signal data received in an RF detector coil can be expressed as:

$$s_l(\mathbf{k}) = \int e^{i\mathbf{k}\cdot\mathbf{r}} C_l(\mathbf{r})\rho(\mathbf{r})d\mathbf{r} \qquad [3.1]$$

where $s_l(\mathbf{k})$ is the signal received in the l^{th} coil at *k*-space position $\mathbf{k}$, C_l is the coil sensitivity of the l^{th} coil and ρ is the excited spin density at position-space vector $\mathbf{r}$.

In parallel imaging, some of the *k*-space sampling locations are omitted in order to accelerate image acquisition. PARS reconstructs these omitted data points by linearly combining the acquired data in the *k*-space vicinity defined by the *k*-space radius k_R.

$$\sum_{\Delta\mathbf{k}} \sum_{l'=1}^{L} w_{\Delta\mathbf{k},l'} s_{l'}\left(\mathbf{k}_{recon} - \Delta\mathbf{k}\right) = s_l\left(\mathbf{k}_{recon}\right), \qquad \left\|\Delta\mathbf{k}\right\| \le k_R \qquad [3.2]$$

Here, $w_{\Delta \mathbf{k},l'}$ are complex weights to be derived in Eqs. [3.3]-[3.11]. l' is the summation variable for the component coils. $s_{l'}(\mathbf{k}_{recon} - \Delta\mathbf{k})$ are the data acquired at k-space offset $\Delta\mathbf{k}$ with respect to $\mathbf{k}_{recon}$. $\| \cdot \|$ denotes Euclidian distance.

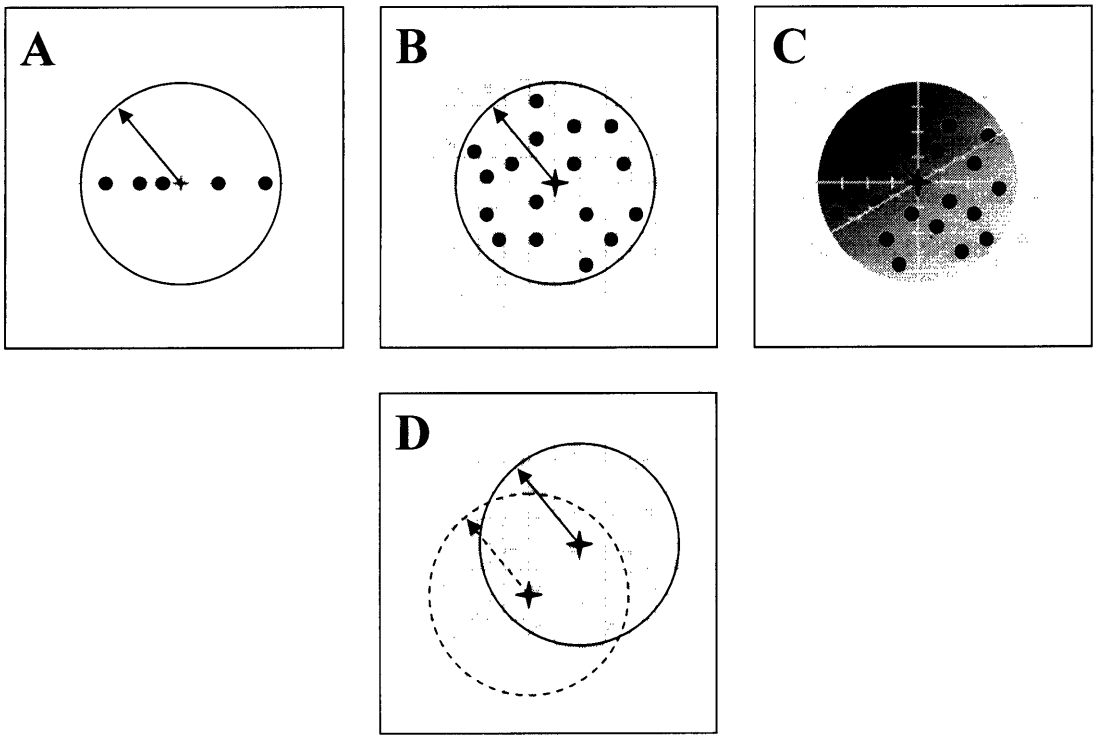

FIGURE 3.1 Schematic of the PARS Algorithm

Schematic illustration of the PARS algorithm applied to 1-, 2-, and 3-dimensional non-Cartesian sampling patterns (a-c). K-space sampling locations are represented by solid dots, colored black if lying within the k-space radius (kR = 4) and gray if lying outside. PARS selects only proximal signal data (black dots) for the reconstruction of the omitted data of interest (indicated by the star at the center). The sliding kernel approach of PARS is illustrated in (d): after an omitted datum is reconstructed, the circle (or sphere) is moved to the next k-space location to be reconstructed. The process is repeated until the dataset is complete.

Fig. 3.1 illustrates the application of the k-space locality constraint in 1-, 2- and 3-dimensional data acquisition schemes. MR signal data are acquired at k-space locations

represented by solid dots. The unit distance on the Cartesian grid is conventionally defined as $\frac{2\pi}{Field\ of\ View}$. In this example, we select k_R to be 4, or $\frac{8\pi}{Field\ of\ View}$. Sampling points lying within the circle (or sphere) of radius k_R are drawn in black, and their corresponding signal data are used in the reconstruction of $s_l(\mathbf{k}_{recon})$. This process is repeated for each $\mathbf{k}_{recon}$ until a complete dataset is reconstructed. Here, $\mathbf{k}_{recon}$ are set to coincide with the Cartesian grid points, so that a component coil image for the l^{th} coil can be obtained by taking the FFT of the PARS reconstructed signal set $s_l(\mathbf{k}_{recon})$.

The complex weights $w_{\Delta k,,l'}$ are computed by performing a least-squares fit that satisfies the following equation:

$$\sum_{\Delta\mathbf{k}}\sum_{l'=1}^{L} w_{\Delta\mathbf{k},l'} e^{i(-\Delta\mathbf{k})\cdot\mathbf{r}} C_{l'}(\mathbf{r}) \approx C_l(\mathbf{r}), \qquad \|\Delta\mathbf{k}\| \le k_R \qquad [3.3]$$

Details of the least-squares fitting procedure are presented later in Eqs. [3.8] - [3.11].

By substituting Eq. [3.3] into the signal equation (Eq. [3.1]), we obtain:

$$\begin{aligned} s_l(\mathbf{k}_{recon}) &= \int e^{i\mathbf{k}_{recon}\cdot\mathbf{r}} C_l(\mathbf{r})\rho(\mathbf{r})d\mathbf{r}, \qquad \|\Delta\mathbf{k}\| \le k_R \\ &\approx \int e^{i\mathbf{k}_{recon}\cdot\mathbf{r}} \sum_{\Delta\mathbf{k}}\sum_{l'=1}^{L} w_{\Delta\mathbf{k},l'} e^{i(-\Delta\mathbf{k})\cdot\mathbf{r}} C_{l'}(\mathbf{r})\rho(\mathbf{r})d\mathbf{r} \\ &\approx \sum_{\Delta\mathbf{k}}\sum_{l'=1}^{L} w_{\Delta\mathbf{k},l'} \int e^{i\mathbf{k}_{recon}\cdot\mathbf{r}} e^{i(-\Delta\mathbf{k})\cdot\mathbf{r}} C_{l'}(\mathbf{r})\rho(\mathbf{r})d\mathbf{r} \\ &\approx \sum_{\Delta\mathbf{k}}\sum_{l'=1}^{L} w_{\Delta\mathbf{k},l'} \int e^{i(\mathbf{k}_{recon}-\Delta\mathbf{k})\cdot\mathbf{r}} C_{l'}(\mathbf{r})\rho(\mathbf{r})d\mathbf{r} \\ &\approx \sum_{\Delta\mathbf{k}}\sum_{l'=1}^{L} w_{\Delta\mathbf{k},l'} s_{l'}(\mathbf{k}_{recon}-\Delta\mathbf{k}) \end{aligned} \qquad [3.4]$$

In the limit where k_R is set to be minimal and if only one term remains in the first summation series $\sum_{\Delta\mathbf{k}}$, i.e. only the nearest neighbor point contributes to the reconstruction of a given missing point,

$$s_l(\mathbf{k}_{recon}) \approx \sum_{l'=1}^{L} w_{l'} s_{l'}(\mathbf{k}_{nearest-neighbor}) \qquad [3.5]$$

then the PARS reconstruction converges to SMASH (Fig 3.4b). However, this special convergence does not occur if there are two or more equidistant nearest neighbors, which is generally the case for undersampled Cartesian trajectories (Figs. 3.4a and 3.4c). In the opposite limit where k_R is infinite, the reconstruction becomes a "strong" version of SENSE in which a full complement of encoding functions are transformed by least-squares fitting to ideal voxel shape functions. An analogous derivation showing these convergences has been reported in Ref. (3). Another interesting limit is when the number of coils L in the second summation series $\sum_{l'=1}^{L}$ becomes one (as in non-parallel imaging), in which case PARS converges to a variant of the Block Uniform ReSampling (BURS) reconstruction (12).

$$s(\mathbf{k}_{recon}) \approx \sum_{\Delta\mathbf{k}} w_{\Delta\mathbf{k}} s(\mathbf{k}_{recon} - \Delta\mathbf{k}), \qquad \|\Delta\mathbf{k}\| \le k_R \qquad [3.6]$$

In our current implementation of PARS, component images are first reconstructed coil-by-coil and are then combined as the sum-of-squares, a strategy that has been reported in Refs. (9) and (13) and that serves to improve the quality of the least-squares fit. In a coil-by-coil reconstruction, a different set of weights is calculated for each coil dataset (Eq. [3.3]), yielding a weight matrix table **W**:

$$\mathbf{W}_{l,(\Delta k,l')} = \left[w_{\Delta k,l'} \right]_{for\ the\ l^{th}\ coil\ dataset}. \qquad [3.7]$$

With appropriate discretization of the continuous position vector **r** to selected voxel locations $\mathbf{r}_\gamma$, Eq. [3.3] can be reformulated into the following matrix representation:

$$\mathbf{WE} \approx \mathbf{C} \qquad [3.8]$$

where the entries of the encoding matrix **E** are:

$$\mathbf{E}_{(\Delta\mathbf{k},l'),\gamma} = e^{i(-\Delta\mathbf{k})\cdot\mathbf{r}_\gamma} C_{l'}(\mathbf{r}_\gamma), \qquad [3.9]$$

and the entries of the coil sensitivity matrix **C** are:

$$\mathbf{C}_{l,\gamma} = C_l(\mathbf{r}_\gamma). \qquad [3.10]$$

The least-squares solution for **W** is derived by taking the Moore-Penrose pseudo-inverse,

$$\begin{aligned} &\mathbf{WE} \approx \mathbf{C} \\ &\mathbf{W} = \mathbf{CE}^H \left(\mathbf{EE}^H\right)^{-1}. \end{aligned} \qquad [3.11]$$

SECTION 3.3 Methods

Two sets of experiments were performed with Cartesian and non-Cartesian data acquisitions respectively. Image reconstruction algorithms in this work were implemented using MATLAB (MathWorks, Natick, MA, USA) on a Windows-based AMD Athlon XP 2500+ system.

3.3.a Cartesian Sampled Data

DATA ACQUISITION

The first set of experiments was performed on a 1.5T TwinSpeed System (GE Healthcare, Waukesha, WI, USA). Data were acquired in a 14.8 x 15 x 37.2 cm rectangular phantom using a coil array of eight independently-positionable elements (Model NMSC-010B-1.5TGE, Nova Medical, Inc., Wakefield, MA, USA). Each coil element measured 8 x 18 cm. The eight elements were divided into two sets of 4-element arrays each of 32 x 18 cm total extent, positioned on the top and bottom of the phantom. A 3-D spoiled gradient echo pulse sequence was used (TE = 2.9 ms, TR = 6.2 ms, RF excitation angle = 15°, 380 mm x 380 mm FOV, 256 x 256 matrix, 16 slices, 4mm slice thickness). Data were acquired in an axial volume with frequency encoding performed in the foot-head direction. The data acquisitions were accelerated 1- to 4-fold in the left-right direction. A low-resolution coil sensitivity reference was acquired in a separate scan.

In vivo scans of a healthy adult volunteer were performed on the same GE scanner, and the pulse sequence parameters, coil configuration and acceleration factors were set up to match those of the phantom experiment (with the exception of a slightly smaller 340 mm x 340 mm FOV).

DATA RECONSTRUCTION AND ANALYSIS

PARS reconstructions using k_R's from 1 to 18 were performed on the phantom datasets. The PARS reconstructed sum-of-squares images were quantitatively compared to unaccelerated fully sampled sum-of-squares reference images by calculating total error power as follows:

$$Total\ Error\ Power = \frac{\sum_{x,y \in FOV} \left| Reference(x,y) - PARS(x,y) \right|^2}{\sum_{x,y \in FOV} \left| Reference(x,y) \right|^2} \qquad [3.12]$$

Here, the summation $\sum_{x,y \in FOV}$ spans the entire field of view (FOV). The k_R that yielded the least total error power at a particular acceleration factor was designated as the "minimal-error" k_R.

This empirically determined minimal-error k_R was then used in the PARS reconstruction of the *in vivo* datasets. PARS-reconstructed *in vivo* images were qualitatively compared to SENSE-reconstructed images.

3.3.b Non-Cartesian Sampled Data

Data Acquisition

The second set of experiments was performed on a 1.5T Gyroscan ACS-NT whole body MR system (Philips Medical Systems, Best, NL). *In vivo* data were acquired in a volume containing the coronary arteries of healthy adult volunteers with a commercial five-element Synergy coil array (two flexible circular elements placed on the chest wall and three rectangular elements contoured to the table and arranged left-to-right at the subject's back). Navigator gated and corrected, ECG triggered 3D spiral pulse sequences were used with conventional phase encoding in the slice-selection direction (13 phase encode steps, 30 mm slab thickness along the approximately superior-inferior direction) (14). One spiral interleaf was acquired per R-R interval, using variable angular speed spiral encoding in-plane (effective TE 1.5 ms, sampling window 20 ms, RF excitation angle = 90°, 360 mm x 360 mm FOV, 512 x 512 matrix). A total of 42 spiral interleaves were acquired in a fully sampled

dataset. Threefold acceleration was achieved by acquiring only every third of the spiral interleaves.

Data Reconstruction and Analysis

Low-resolution *in vivo* sensitivity maps were extracted from the densely sampled *k*-space center using methods described in Ref. (15). SVD conditioning (truncation of singular values less than 0.01 of the maximum singular value) was used to further enhance the stable inversion of the localized encoding matrices. Three comparative PARS reconstructions were performed with *k*-space radii k_R = 1, 2, 3.

Section 3.4 Results

Fig. 3.2 illustrates the contribution of neighboring data in the reconstruction of an omitted datum in a twofold undersampled dataset. Complex weights used by parallel image reconstructions were calculated based on simulated coil sensitivities (**a-c**), or acquired coil sensitivities (**d-f**). Three reconstruction methods were used in calculating the weights: **a**,**d**) SENSE, **b**,**e**) PARS with k_R = 1, and **c**,**f**) PARS with k_R = 5. The omitted datum to be reconstructed was located at k = 0, and MR data were acquired at k = -127, -125,..., 125, 127 (a two-fold accelerated acquisition). The magnitude of the weights of one of eight coils is plotted. *K*-space locality of RF coil encoded data is demonstrated by the diminishing contribution of signal data as a function of *k*-space separation from the omitted datum (**a**,**d**). PARS effectively enforces this *k*-space locality by allowing a finite number of non-zero values at the center but setting all other weights to zero, as illustrated by the central spikes whose widths are equal to twice the chosen k_R value (i.e. 2 in (**b**,**e**) and 10 in (**c**,**f**), respectively).

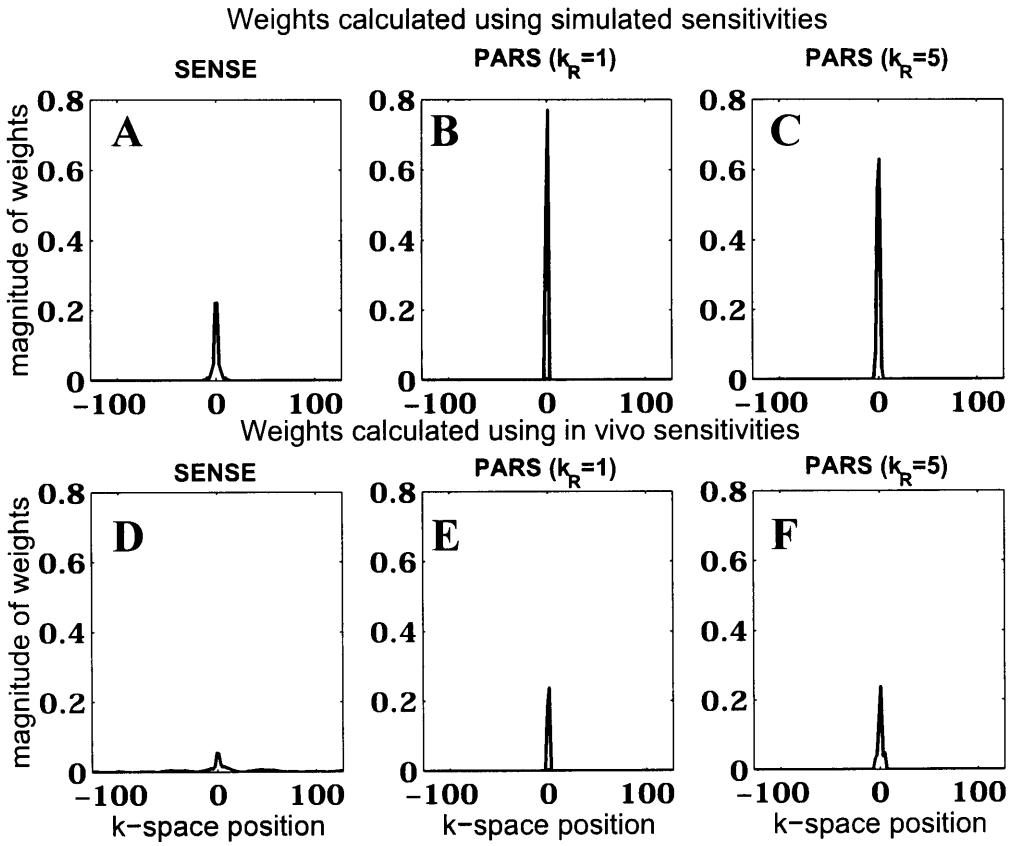

FIGURE 3.2 Principle of k-Space Locality in Parallel MRI

Illustration of the inherent *k*-space locality in parallel MRI. Complex reconstruction weights were calculated based on a-c) simulated coil sensitivities, and d-e) acquired coil sensitivities. Three reconstruction methods were used: a,d) SENSE, b,e) PARS with k_R = 1, and c,f) PARS with k_R = 5. The omitted datum was located at k = 0, and MR data were acquired at k = -127, -125,..., 125, 127 (a 2-fold undersampling). The magnitude of the weights of one of eight coils is plotted as a function of *k*-space position.

Fig. 3.3 illustrates the effects of two types of noise (noise in signal data and in coil sensitivities) for SENSE and PARS image reconstructions of a simulated 3-fold one-dimensionally accelerated dataset. Signal data noise was simulated with standard deviations equal to 0.01 (**a**), 0.02 (**b**) and 0.05 (**c**) of the maximum image intensity. The square root of the total error power is plotted on a log-log scale as a function of sensitivity noise with standard deviations ranging from 10^{-4} to 10^{-1} of the maximum coil sensitivity.

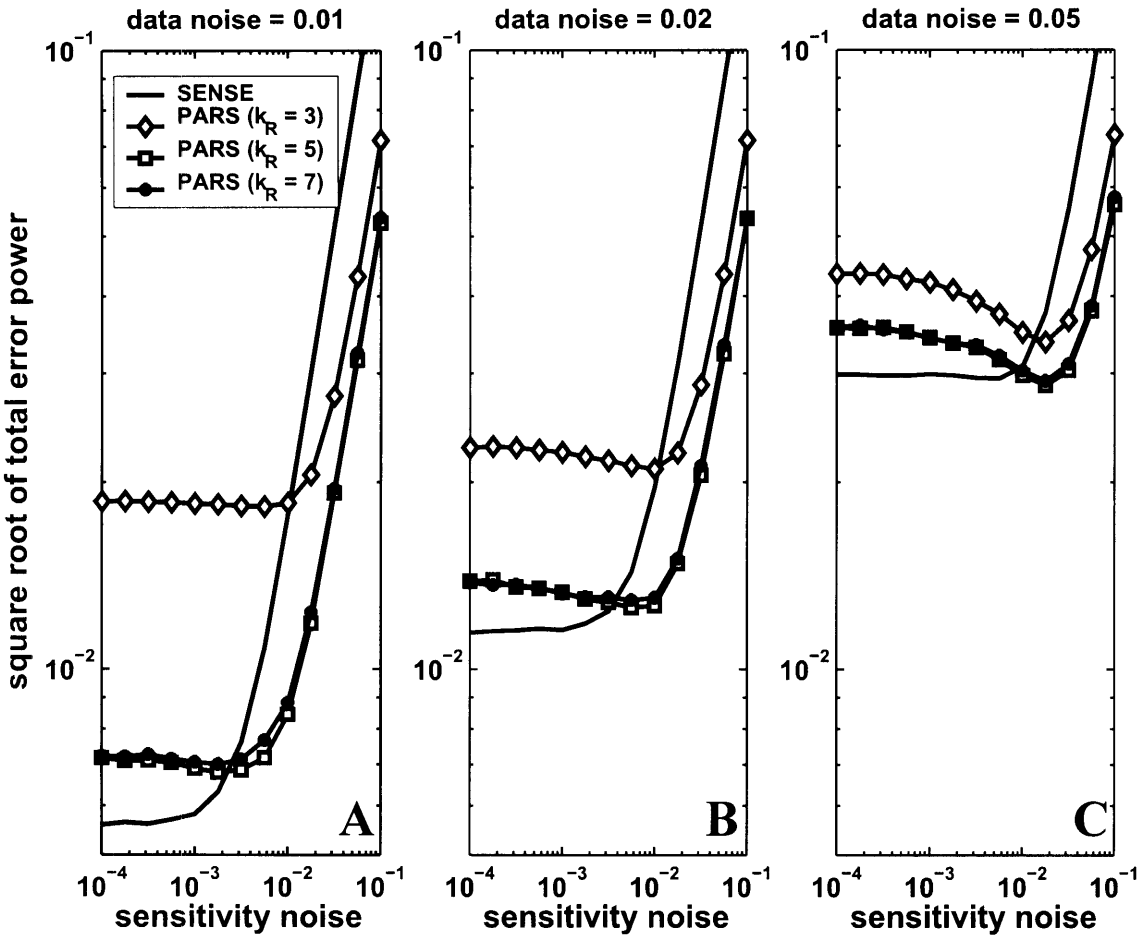

FIGURE 3.3 Total Error Power vs Sensitivity Noise

Illustration of the effect of signal data noise and sensitivity noise in SENSE and PARS image reconstructions. Three-fold one-dimensionally-accelerated datasets were simulated with signal data noise standard deviations equal to 0.01 (a), 0.02 (b) and 0.05 (c) of the maximum image intensity, and coil sensitivities were simulated with noise standard deviations ranging from 10^{-4} to 10^{-1} of the maximum coil sensitivity. The square root of the total error power in the reconstructed images is plotted on a log-log scale as a function of sensitivity noise.

Fig. 3.4 plots the total error power as a function of the *k*-space radius k_R in the phantom experiments. The datasets were regularly undersampled in the left-right direction by factors of two (a), three (b), and four (c). PARS reconstructions with a range of k_R were performed, and the total error power was calculated as described by Eq. [3.12]. Similarly, SMASH and SENSE reconstructions were performed. The corresponding total error power

is plotted. Different acceleration factors yielded different "minimal-error" k_R's. As shown in this figure, the total error initially decreases and then increases as a function of k-space radius. Relatively broad minima occur at some mid-range k-space radii. The total error power of SMASH and SENSE are consistently higher than those of the PARS minima.

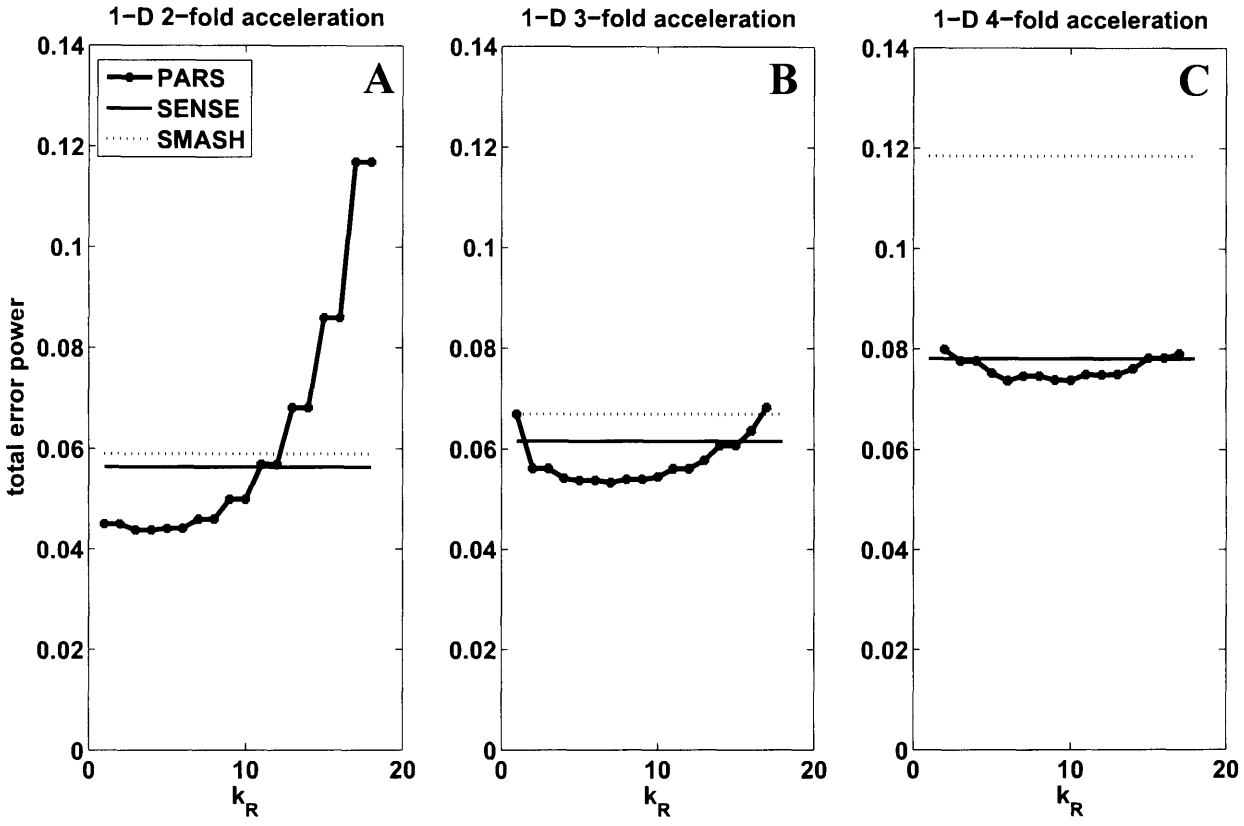

FIGURE 3.4 **Total Error Power vs k-space Radius**

Total error power as a function of the k-space radius k_R in PARS reconstructions. Phantom datasets were undersampled in one dimension on a Cartesian grid, and image reconstructions were performed using PARS with a range of k-space radii. The total error power of PARS, SENSE, and SMASH reconstructions were calculated by a pixel-by-pixel subtraction against a fully-sampled reference image (see text). The minimal total error power occurred at k_R = 3 for 2-fold acceleration; at k_R = 7 for 3-fold acceleration; and at k_R = 9 for 4-fold acceleration.

Fig. 3.5 illustrates the PARS reconstructions of 1-D accelerated *in vivo* data. The empirically determined "minimal-error" *k*-space radii were used. For twofold acceleration, $k_R = 3$ (**a**); for threefold acceleration, $k_R = 7$ (**b**); and for fourfold acceleration, $k_R = 9$ (**c**). SENSE image reconstructions (**d-f**) at the corresponding acceleration factors are displayed for comparison. Corresponding computation times of different techniques are shown in Table 3.1.

Fig. 3.6 illustrates PARS reconstructions of 2-D accelerated non-Cartesian *in vivo* data. A fully sampled spiral image (**a**) and PARS reconstructed images for threefold undersampled spiral trajectories **(b-d)** using different k_R's are compared. k_R's used for the PARS reconstructions were 1 (**b**), 2 (**c**) and 3 (**d**). Corresponding computation times of different techniques are shown in Table 3.2.

	2-fold	**3-fold**	**4-fold**
SMASH	5.0	5.9	6.2
PARS ($k_R = 3$)	11.1	6.3	7.0
PARS ($k_R = 7$)	57.4	32.1	27.5
SENSE	5.1	4.0	3.6

TABLE 3.1 **Reconstruction Times (in sec) for Undersampled Cartesian Trajectories.**

	3-fold
PARS ($k_R = 1$, using 1 processor)	13
PARS ($k_R = 1$, using 2 parallel processors)	7
PARS ($k_R = 2$, using 1 processor)	75
PARS ($k_R = 2$, using 2 parallel processors)	38
Iterative SENSE (using 1 processor)	3

TABLE 3.2 **Reconstruction Times (in min) for Undersampled Spiral Trajectories.**

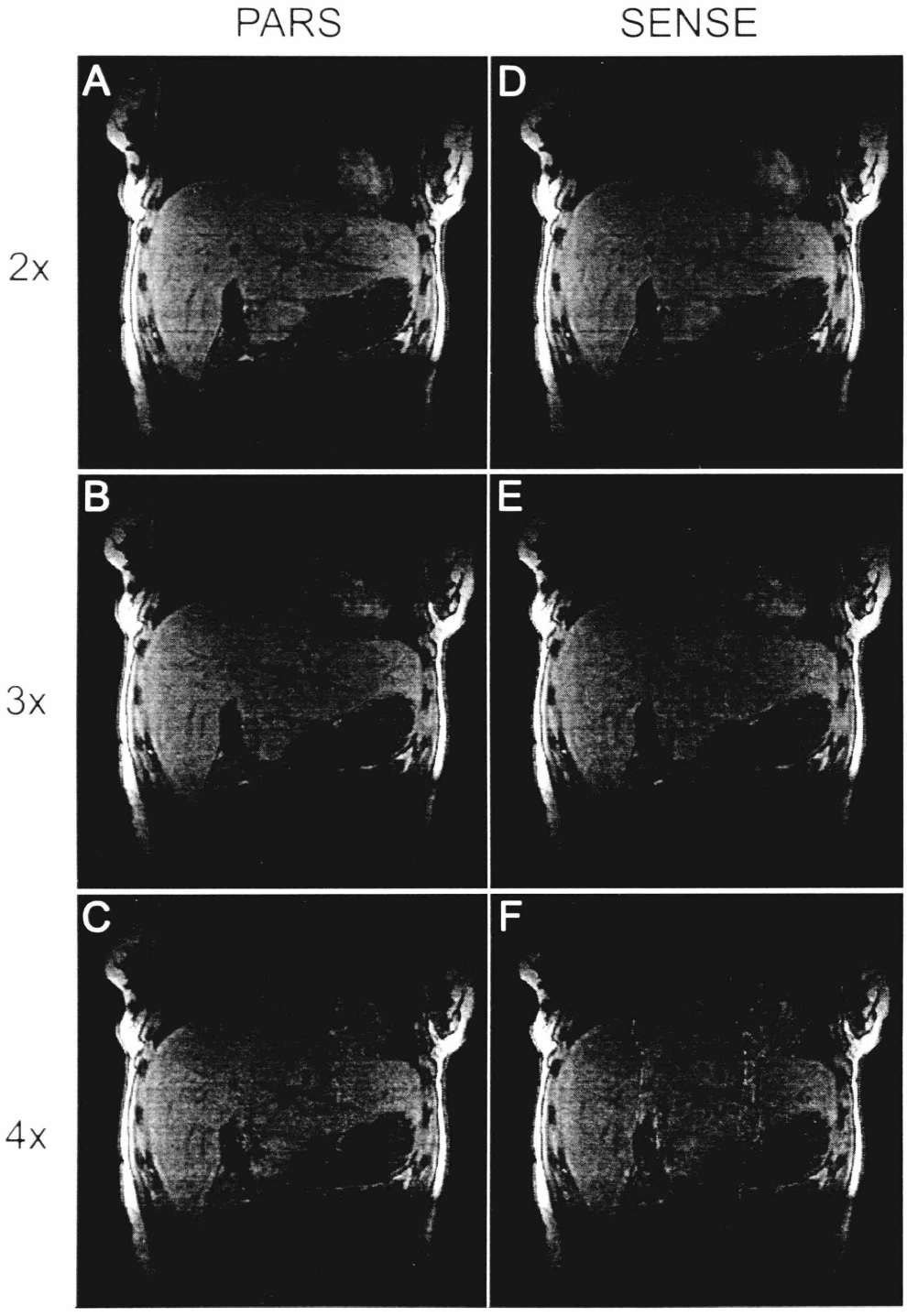

FIGURE 3.5 In Vivo Image Comparisons of PARS and SENSE

Comparison of parallel image reconstructions of in vivo datasets at various acceleration factors. a-c) PARS reconstructions using the "minimal error" k_R obtained from the phantom experiment (k_R = 3 for twofold acceleration (a), k_R = 7 for threefold acceleration (b), and k_R = 9 for fourfold acceleration (c)). d-f) SENSE reconstructions at the corresponding acceleration factors.

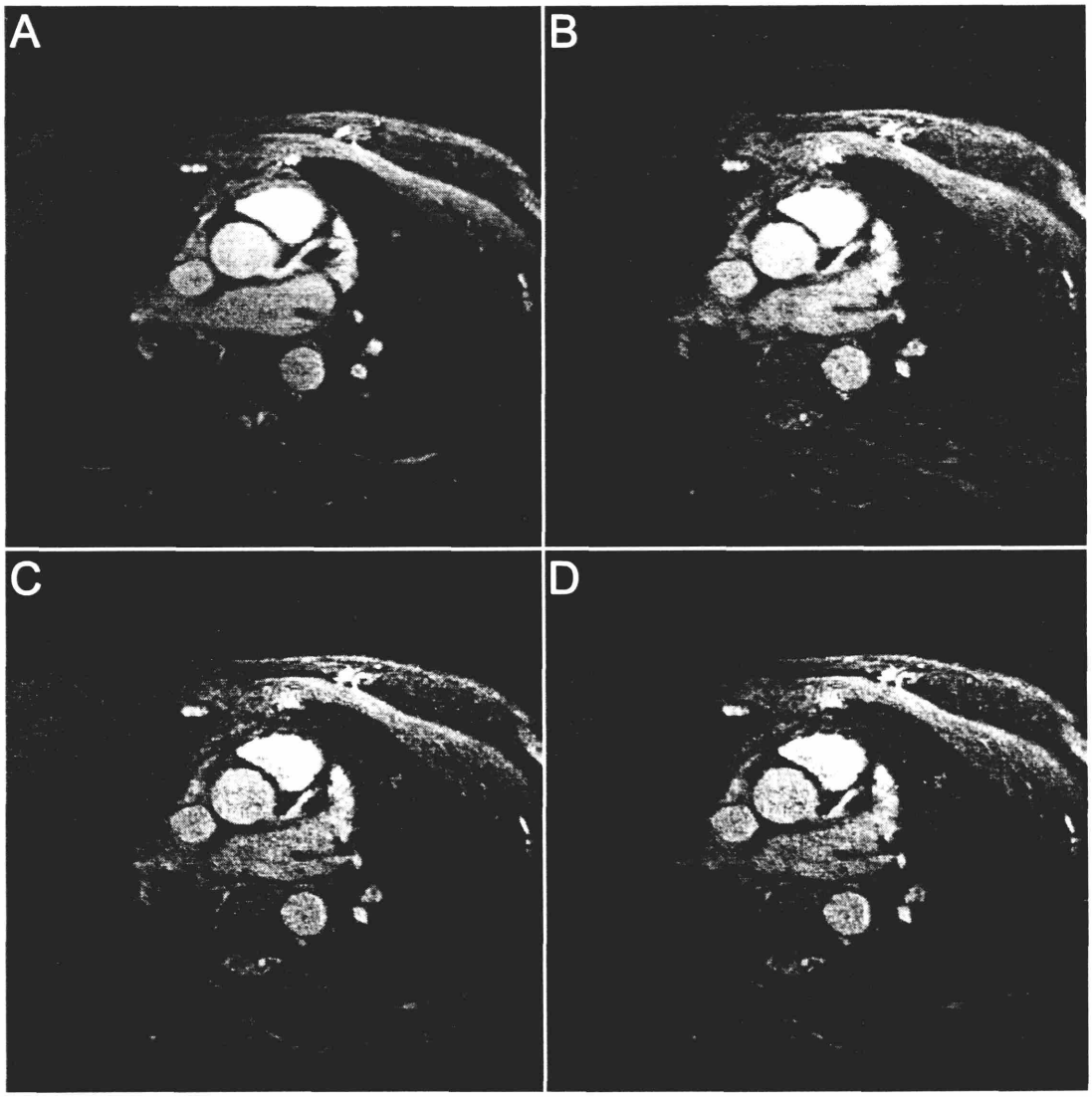

FIGURE 3.6 PARS Reconstructions Using Different k-space Radii

PARS reconstructions of data acquired with 2-D accelerated non-Cartesian trajectories. Unaccelerated reference image (a) and PARS reconstructed images of threefold accelerated spiral trajectories with *k*-space radii k_R=1 (b), k_R=2 (c), k_R = 3 (d).

SECTION 3.5 Discussion

3.5.a k-space locality and computational efficiency

By imposing the *k*-space locality constraint, PARS exploits the physical characteristics of RF coil sensitivity encoding to improve parallel image reconstruction. It has been shown in Ref. (7) that RF surface coils of simple conductor geometry have sensitivity profiles that are smooth in the object domain and band-limited in *k*-space. The effect of multiplication of the imaged object by these coil sensitivities (e.g. Eq. [3.1]) is therefore a finite-kernel convolution in *k*-space. The original Fourier components of the object of interest are locally spread in the acquired MR signal data. Conversely, acquired signal data proximal to a given omitted signal datum are expected to have the greatest contribution in reconstructing that datum, as is shown in Fig. 3.2. Exploiting this physical property dramatically reduces the computational burden associated with inverting the full non-Cartesian encoding matrix while preserving the dominant behavior of the full inverse. In addition, the PARS sliding-kernel approach allows data to be directly reconstructed on a Cartesian grid, eliminating the need to regrid the reconstructed data points.

3.5.b Effect of noise and artifact on total error

In a noise-free scenario, the choice of k_R is analogous to the width of the convolution kernel in non-parallel image reconstruction approaches such as the gridding algorithm (16). For a gridding reconstruction, increasing the kernel width results in reducing the artifact power. The benefit of minimizing artifact comes at a cost in computation time and memory. In the gridding algorithm, it has been shown that an infinite sinc function, i.e. $k_R = \infty$, is the ideal kernel, in spite of the long computation time. The same may be argued for k_R in PARS, as long as the noise-free assumption holds.

Once noise is introduced into coil sensitivities (as shown in Figs. 4.2d-f and 4.3a-c), however, the *k*-space locality constraint imposed by PARS becomes a powerful tool: a larger k_R inevitably includes diminishingly smaller coefficients of the noise-corrupted sensitivities and leads to a more inaccurate encoding matrix, counterbalancing the benefit of artifact

reduction. Thus, the truncation of the inverse problem at a modest k_R not only improves computational tractability but also serves to regularize the inversion. The accuracy of the inversion is improved in exchange for a moderate level of artifact, which can be tuned to fall underneath the baseline noise level. In certain special scenarios, as illustrated in Fig. 3.3c where PARS image reconstructions achieve minimal error around sensitivity noise = $2\text{x}10^{-2}$, PARS performance may be paradoxically improved by injecting some low level of noise in the coil sensitivity. The numerical conditioning effect of noise has been previously reported in Ref. (17), and its overall effect is analogous to that of numerical conditioning procedures that have begun to be applied in many current parallel imaging algorithms (for example, Tikhonov regularization, c.f. (18)).

Traditional conditioning methods also have the potential to complement the inherent PARS regularization. When comparing the effects of conditioning between PARS and other parallel imaging reconstructions, it is important to note that the computational feasibility of traditional conditioning methods is strictly dictated by the size and structure of the encoding matrix. In Cartesian sampling where the encoding matrix can be partitioned simply by performing an FFT, traditional conditioning methods can be easily implemented for most parallel imaging techniques. In non-Cartesian sampling where simple block diagonalization by FFT is not available, however, the *k*-space locality constraint in PARS provides an enabling advantage by allowing a different local partitioning of the prohibitively large matrix, thereby facilitating additional numerical conditioning. Furthermore, the use of independent matrix inverses provides a high degree of flexibility, including the ability to apply variable conditioning thresholds for different *k*-space clusters.

3.5.c Total error power

The total error power calculation used in this work constitutes a single integrated metric to quantify the overall error in parallel image reconstruction. This metric measures the combined effect of artifact and noise amplification. The commonly used geometry factor (g-factor) only accounts for noise amplification, and therefore is not adequate to characterize

parallel imaging techniques that trade artifact for improved matrix inversion accuracy and/or reduced noise amplification.

PARS reconstructions using a very small *k*-space radius are typically relatively immune to error in coil sensitivities, which can be advantageous for noise-prone coil sensitivity calibrations (Fig. 3.3). However, because of the limited number of encoding functions, the least-squares fit in Eq. [3.3] may not be very good. Consequently, the artifact term dominates in the total error calculation. As the *k*-space radius increases, more equations are included in the least-squares fit, resulting in a better fit with decreased residual artifact. However, the amplification of noise or errors in coil sensitivities increases and becomes dominant.

As expected, the SMASH reconstruction has a relatively large artifact power due to the constraint of using only the nearest neighbor. In the special case of $k_R = 1$ at 3-fold acceleration (Fig. 3.4b), PARS converges to SMASH because at any omitted data location, only one acquired MR signal datum can be reached by a *k*-space radius of 1. The SENSE reconstruction used in this work is a weak case of SENSE which, unlike the strong version, has some degrees of freedom to optimize SNR. Nonetheless, the total error power of SENSE is higher than the minimal-error PARS reconstruction in the phantom experiments.

Fig. 3.3 illustrates the tradeoff between artifact power and error amplification at various simulated noise values. SENSE is a so-called "exact" reconstruction such that in the limit of infinite SNR in both sensitivity and signal data, the total error approaches zero (that is, ignoring the often modest variances from any chosen target image associated with reconstructed point spread functions). On the other hand, since PARS (like other constrained parallel imaging techniques) has a non-zero artifact power for limited *k*-space radius, the total error in the limit of infinite SNR asymptotically approaches the value of that residual artifact power. However, at typical *in vivo* operating SNR (e.g. SNR < 100), the total error power is dominated by error resulting from noisy sensitivity and signal data, and in this case, PARS can demonstrate definitive advantages over an exact reconstruction.

3.5.d Qualitative image comparisons

For *in vivo* datasets acquired on Cartesian trajectories, PARS reconstructed images show reduced noise amplification and increased immunity to coil sensitivity error as compared with corresponding SENSE images. At higher acceleration factor (e.g. three- and four-fold), the noise reduction is more pronounced visually. Also, because the sensitivity reference was acquired in a separate scan, image registration is a particular problem at the edges of the object. This calibration error results in conspicuous artifacts in the reconstructed images, in particular for the four-fold SENSE reconstruction. This challenge has been addressed for SENSE-like reconstructions by implementing techniques for sensitivity extrapolation and smoothing. On the other hand, PARS automatically accomplishes the same effect through the *k*-space locality constraint.

For the *in vivo* spiral datasets, the PARS reconstructed images demonstrate the principle of *k*-space locality in two dimensions. The PARS threefold accelerated reconstruction using k_R=1 has the highest visible noise background whereas those of k_R=2 and k_R=3 show comparable image quality. Also, the *k*-space radius can be made adaptive in this example. As shown in Fig. 3.4, in the 1-D case, the "minimal-error" k_R is different for different undersampling factors. Since the spiral trajectory (as well as other non-Cartesian trajectories) has variable local sampling density, it is possible to have an adaptive k_R that varies as a function of the local sampling density.

On the other hand, Fig. 3.4 also illustrates that at a given acceleration factor, the total error power varies slowly around the "minimal-error" k_R. These broad minima suggest that a "good-enough" k_R can be coarsely determined, with some tolerance to moderate variations in acceleration and other scanning parameters (e.g. FOV and image plane orientation). Once a "good-enough" k_R has been determined for a given coil array, the same k_R can be routinely used for PARS reconstructions, without the need for careful optimization.

3.5.e Characteristics of magnitude noise in sum-of-square combination

GRAPPA (9) and PARS share the feature that reconstructions are performed in a coil-by-coil fashion followed by sum-of-squares combination. In this case, the noises across the reconstructed component coil images are correlated and have non-identical variances (13). The effect of sum-of-squares combination on non-white, non-identical noises has not been fully characterized, since existing work only addresses the special case when the coil noises are uncorrelated and of identical variance (19,20). Preliminary work on the development of a new generalized model for magnitude noise analysis will be presented in Chapter 5 of this thesis. This new analysis is required to determine the theoretical effect of varying *k*-space radius on the SNR of PARS reconstructions. In the meantime, the total error power calculation proposed in this work serves as a convenient and, in some ways more relevant, metric to empirically determine the "minimal-error" *k*-space radius.

3.5.f PARS and BURS

PARS, in its application of *k*-space locality and choice of kernel size, bears a close analogy with the Block Uniform ReSampling (BURS) algorithm, (12,21,22) a "regridding" algorithm for non-parallel imaging. As shown in Eq. [3.6], PARS may be formulated as a generalization of BURS that incorporates coil sensitivities in forming the coil-gradient modulated encoding functions. The addition of the coil dimension in PARS expands the number of encoding functions by a factor equal to the number of coils. In the case of an accelerated acquisition, the expanded encoding function set in PARS enables a successful reconstruction of the undersampled data.

3.5.g Iterative and non-iterative approaches to non-Cartesian parallel imaging

In addressing the computational burden of 2-D non-Cartesian imaging, an iterative variant of SENSE has been proposed to avoid the creation and manipulation of the generalized encoding matrix. This implementation of SENSE (5) employs repeated gridding

and ungridding procedures within a conjugate gradient algorithm. In our implementations using MATLAB, iterative SENSE reconstructions tended to have a shorter total run time than PARS reconstructions. This is demonstrated in Table 4.2. (Computation times in both Table 4.1 and Table 4.2 were benchmarked using prototype Matlab code with little optimization – absolute performances are typically many times faster when implemented and optimized using low-level languages such as C.) However, because PARS involves inverting many small and independent matrices, the algorithm is massively parallelizable for a distributed computing environment (23). This is also demonstrated in Table 4.2. In the 2D non-Cartesian image reconstructions, PARS simply distributes the point-by-point data reconstructions across parallel processors with minimal overhead. Moreover, instead of requiring complete acquisition of the full data set prior to the initiation of image reconstruction, the PARS reconstruction can begin as soon as a local cluster of acquired signal data becomes available. This is expected to provide advantages for low-latency reconstructions in real-time applications of self-calibrating parallel imaging.

The advantage of only requiring a small subset of acquired data to reconstruct any particular *k*-space point will become increasingly important as parallel imaging expands to the realm of three-dimensionally accelerated non-Cartesian trajectories. For example, a 256x256x256 volumetric dataset acquired with a multi-element coil array will occupy on the order of gigabyte of storage space. Even simple operations such as loading and storing the dataset in a conventional memory space will require special effort in system engineering. Algorithms such as PARS, which can judiciously partition the dataset and distribute the computational burden to parallel processors will be much easier to implement. Lastly, unlike the iterative conjugate gradient approach, PARS computes the actual reconstruction weights that are responsible for noise amplifications, permitting explicit *g*-factor maps to be calculated accordingly (24). This property may prove useful in verifying for non-Cartesian trajectories the SNR advantages that are expected from two- and three-dimensional acceleration (25). Appendix A describes a general strategy to calculate the noise amplification in PARS reconstruction.

SECTION 3.6 Conclusions

We have outlined the theory and implementation of the PARS algorithm, which exploits the common physical characteristic of *k*-space locality that is inherent in RF coil encoded data. Instead of inverting a prohibitively large encoding matrix, the PARS algorithm partitions the inversion burden into manageable and distributable independent matrix inverses. These small inversions are not only computationally efficient, but also have a desirable regularization effect which is critical for parallel imaging at high acceleration factors. As parallel imaging expands to highly accelerated 3-D trajectories with many-element coil arrays, PARS promises an attractive solution to critical issues such as data volume, computability, numerical stability, and the desirable balance of SNR and artifact power.

SECTION 3.7 Appendix A

A GENERAL STRATEGY TO CALCULATE G-FACTOR FOR PARS RECONSTRUCTIONS

The PARS weight matrices, computed by independent inversions of localized encoding matrices (Eq. [3.11]), can be collectively arranged to form a reconstruction matrix $\mathbf{\Omega}$, such that:

$$\mathbf{s}_l^{recon} = \mathbf{\Omega}\mathbf{s}^{acq} \qquad [3.13]$$

In a coil-by-coil reconstruction, $\mathbf{s}_l^{recon}$ is the PARS reconstructed signal vector of the l^{th} component coil, and $\mathbf{s}^{acq}$ is the acquired signal vector from the coil array. The size of $\mathbf{\Omega}$ is potentially very large, as in the case of non-Cartesian multi-dimensional trajectories. However, $\mathbf{\Omega}$ is extremely sparse because of the PARS k-space locality constraint, with the degree of sparseness of $\mathbf{\Omega}$ determined by the k-space radius k_R. A coil image is reconstructed by performing an inverse Fourier transformation on $\mathbf{s}_l^{recon}$,

$$\boldsymbol{\rho}_l = \mathbf{F}\mathbf{s}_l^{recon} = \mathbf{F}\mathbf{\Omega}\mathbf{s}^{acq} \qquad [3.14]$$

Here, $\boldsymbol{\rho}_l$ is the component coil image, and $\mathbf{F}$ is the inverse Fourier transform matrix. $\mathbf{\Lambda}_{PARS}$, the noise covariance matrix for the component coil image, is expressed as:

$$\mathbf{\Lambda}_{PARS} = \mathbf{F}\mathbf{\Omega}\mathbf{\Psi}\left(\mathbf{F}\mathbf{\Omega}\right)^H \qquad [3.15]$$

where Ψ is the noise covariance matrix of the acquired signal, and $(\cdot)^H$ is the Hermitian conjugate operator. When a Cholesky factorization is performed

$$\mathbf{\Psi} = \mathbf{L}\mathbf{L}^H \qquad [3.16]$$

to decorrelate and normalize noise in the acquired signal (5), Eq. [3.15] simplifies to:

$$\mathbf{\Lambda}_{PARS} = \mathbf{F}\hat{\mathbf{\Omega}}\hat{\mathbf{\Omega}}^H\mathbf{F}^H \qquad [3.17]$$

where $\hat{\mathbf{\Omega}} = \mathbf{\Omega}\mathbf{L}$. The γ^{th} diagonal element of $\mathbf{\Lambda}_{PARS}$ corresponds to the noise power at the γ^{th} voxel location, and can be computed as follows:

$$\begin{aligned}\left(\mathbf{\Lambda}_{PARS}\right)_{\gamma,\gamma} &= \left(\mathbf{F}\hat{\mathbf{\Omega}}\hat{\mathbf{\Omega}}^{H}\mathbf{F}^{H}\right)_{\gamma,\gamma} \\ &= \sum_{n}\left|\left(\mathbf{F}\hat{\mathbf{\Omega}}\right)_{\gamma,n}\right|^{2} \\ &= \sum_{n}\left|\sum_{m}\mathbf{F}_{\gamma,m}\hat{\mathbf{\Omega}}_{m,n}\right|^{2}\end{aligned} \qquad [3.18]$$

The double summations here can be implemented efficiently in computation and memory storage by taking advantage of the sparseness of $\hat{\mathbf{\Omega}}$ and the fast Fourier transform (FFT). Finally, g_γ, the g-factor at the γ^{th} voxel location, can be expressed as:

$$g_\gamma = \frac{\sqrt{\left(\mathbf{\Lambda}_{PARS}\right)_{\gamma,\gamma}}}{\sqrt{R}\sqrt{\left(\mathbf{\Lambda}_{Ref}\right)_{\gamma,\gamma}}} \qquad [3.19]$$

where R is the acceleration factor and $\mathbf{\Lambda}_{Ref}$ is the noise covariance matrix of the unaccelerated reference image.

While Eqs. [3.15]-[3.19] present a g-factor calculation strategy for PARS reconstructed component coil images, the g-factor for the final PARS sum-of-squares image requires additional calculations that are beyond the scope of this manuscript. The sum-of-squares combination of coil images, performed at the very end of the PARS algoirthm, involves nonlinear magnitude and square root operations which perturb the noise statistics. A strategy that accounts for these additional effects will be studied in detail in Chapter 5.

Chapter 3 References

1. Pruessmann KP, Weiger M, Scheidegger MB, Boesiger P. SENSE: sensitivity encoding for fast MRI. Magn Reson Med 1999;42(5):952-62.
2. Kyriakos WE, Panych LP, Kacher DF, Westin CF, Bao SM, Mulkern RV, Jolesz FA. Sensitivity profiles from an array of coils for encoding and reconstruction in parallel (SPACE RIP). Magn Reson Med 2000;44(2):301-8.
3. Sodickson DK, McKenzie C. A generalized approach to parallel magnetic resonance imaging. Med Phys 2001;28(8):1629-1643.
4. Ra JB, Rim CY. Fast imaging using subencoding data sets from multiple detectors. Magn Reson Med 1993;30(1):142-5.
5. Pruessmann KP, Weiger M, Bornert P, Boesiger P. Advances in sensitivity encoding with arbitrary k-space trajectories. Magn Reson Med 2001;46:638-651.
6. Yeh EN, McKenzie CA, Lim D, Ohliger MA, Grant AK, Willig J, Rofsky NM, Sodickson DK. Parallel imaging with Augmented Radius in k-Space (PARS). In: Proc 10th Annual Meeting ISMRM, Honolulu, Hawaii USA, 2002. p 2399.
7. Bydder M, Larkman DJ, Hajnal JV. Generalized SMASH imaging. Magn Reson Med 2002;47(1):160-70.
8. Sodickson DK, Manning WJ. Simultaneous acquisition of spatial harmonics (SMASH): fast imaging with radiofrequency coil arrays. Magn Reson Med 1997;38(4):591-603.
9. Griswold MA, Jakob PM, Heidemann RM, Nittka M, Jellus V, Wang J, Kiefer B, Haase A. Generalized autocalibrating partially parallel acquisitions (GRAPPA). Magn Reson Med 2002;47(6):1202-10.
10. Wang Y. Description of parallel imaging in MRI using multiple coils. Magn Reson Med 2000;44(3):495-9.
11. McKenzie CA, Lim D, Ransil BJ, Morrin M, Pedrosa I, Yeh EN, Sodickson DK, Rofsky NM. Shortening MR image acquisition time for volumetric interpolated breath-hold examination with a recently developed parallel imaging reconstruction technique: clinical feasibility. Radiology 2004;230(2):589-94.

12. Moriguchi H, Duerk JL. Modified block uniform resampling (BURS) algorithm using truncated singular value decomposition: fast accurate gridding with noise and artifact reduction. Magn Reson Med 2001;46:1189-1201.
13. McKenzie CA, Ohliger MA, Yeh EN, Price MD, Sodickson DK. Coil-by-coil image reconstruction with SMASH. Magn Reson Med 2001;46(3):619-23.
14. Bornert P, Stuber M, Botnar RM, Kissinger KV, Koken P, Spuentrup E, Manning WJ. Direct comparison of 3D spiral vs. Cartesian gradient-echo coronary magnetic resonance angiography. Magn Reson Med 2001;46(4):789-94.
15. Yeh EN, Stuber M, McKenzie CA, Ohliger MA, Grant AK, Willig J, Sodickson DK. Self-Calibrated Spiral Parallel Imaging. In: Proc 10th Annual Meeting ISMRM, Honolulu, Hawaii USA, 2002. p 2390.
16. Jackson JI, Meyer CH, Nishimura D, Macovski A. Selection of a convolution function for Fourier inversion using gridding. IEEE Trans Med Imaging 1991;10(3):473-478.
17. Sodickson DK. Tailored SMASH image reconstructions for robust in vivo parallel MR imaging. Magn Reson Med 2000;44(2):243-51.
18. Lin FH, Kwong KK, Belliveau JW, Wald LL. Parallel imaging reconstruction using automatic regularization. Magn Reson Med 2004;51(3):559-67.
19. Gudbjartsson H, Patz S. The Rician distribution of noisy MRI data. Magn Reson Med 1995;34:910-914.
20. Constantinides CD, Atalar E, McVeigh ER. Signal-to-noise measurements in magnitude images from NMR phased arrays. Magn Reson Med 1997;38(5):852-7.
21. Rosenfeld D. An optimal and efficient new gridding algorithm using singular value decompostion. Magn Reson Med 1998;40:14-23.
22. Rosenfeld D. New approach to gridding using regularization and estimation theory. Magn Reson Med 2002;48:193-202.
23. Cohen S, Grant AK, Yeh EN, Joshi S, Sodickson DK. A Parallel Computing Solution for Rapid Reconstruction of Highly Accelerated Volumetric Parallel MRI Data. In: Proc 12th Annual Meeting ISMRM, Kyoto, Japan, 2004. p 2631.

24. Yeh EN, McKenzie CA, Grant AK, Ohliger MA, Willig J, Sodickson DK. Generalized Noise Analysis for Magnitude Image Combinations in Parallel MRI. In: Proc. 11th Annual Meeting ISMRM, Toronto, Canada, 2003. p 21.

25. Weiger M, Pruessmann KP, Boesiger P. 2D SENSE for faster 3D MRI. Magma 2002;14(1):10-9.

CHAPTER 4. IMAGE RECONSTRUCTION USING PRIOR PHASE INFORMATION[10]

This chapter is devoted to the development of an integrated approach which efficiently incorporates phase information into parallel image reconstruction. In the generalized matrix equation for parallel MRI:

$$\mathbf{s} = \mathbf{E}\rho, \qquad [4.1]$$

all three components (the signal vector s, the encoding matrix **E** and the spin density ρ) are intrinsically complex-valued. However, if the phase of ρ can be accurately determined *a priori*, the real and imaginary components of **s** and **E** can be separated, facilitating a better-conditioned matrix inversion.

SECTION 4.1 Introduction

Parallel MRI techniques utilize prior knowledge of coil sensitivities in order to reduce the *k*-space sampling density required for image reconstruction (1-9). Other techniques have

[10] The work in this chapter has been adapted for publication as "Willig-Onwuachi JD, Yeh EN, Grant AK, Ohliger MA, McKenzie CA, Sodickson SK. Phase-Constrained Parallel MRI Image Reconstruction. J Magn Reson. (In Review)" ENY was primarily responsible for the work in the Theory section while JDW was responsible for designing and implementing the experiments and data analysis described in the Methods and Results sections.

also used different types of prior knowledge to reduce the amount of data required. Constrained reconstructions (10), for example, reconstruct *k*-space lines not acquired during the scan using *a priori* knowledge about the underlying spin density. Phase-constrained (commonly referred to as partial-Fourier) techniques, in particular, like the Margosian (11,12) or Projection Onto Convex Sets (POCS) (13-16), exploit the assumption that a conjugate (Hermitian) symmetry is embedded in MR signal data. With an accurate knowledge of a slowly varying phase map, these techniques only require data acquisition in half of *k*-space to reconstruct a full image.

The complementary use of prior knowledge available for partial-Fourier imaging and for parallel MR has many potential benefits. For example, the two methods can be combined to further reduce imaging time, and various methods of combination have been demonstrated to improve the performance of real-time imaging (17) and the spatial resolution of single-shot imaging (18,19). In spite of some early empirical success, proper combination of the two techniques is not in general straightforward. Instead, rigorous mathematical treatment is warranted in order to avoid unsuspecting pitfalls as well as to harness the full combined potential of the two approaches.

To date, the parallel MR and partial-Fourier reconstructions are performed in two separate steps. The order of the steps, however, is primarily determined by the type of parallel image reconstruction being used. For parallel imaging techniques that reconstitute omitted data points in *k*-space (e.g. SMASH and GRAPPA), it is natural to perform the parallel reconstruction first, followed by the partial-Fourier reconstruction. On the other hand, when using a pixel-by-pixel reconstruction method like Cartesian SENSE, the partial-Fourier technique generally precedes the parallel reconstruction in order to first produce an aliased image. The parallel image technique can then "unfold" the aliased image pixel by pixel. Additionally, careful planning is required because a particular strategy of combining partial-Fourier and parallel MR will alter the allowable *k*-space sampling patterns and the feasible methods for measuring the phase map and coil sensitivities. For these reasons, creating general procedures for partial Fourier parallel MRI can become an interesting and non-trivial exercise.

Further complications for SENSE-like applications are associated with the extraction of the required phase map from the intermediate aliased image. In this case, the critical assumption of a slowly varying phase may no longer to true. The phase of an aliased image, in fact, depends on both the phase *and* the magnetization density of the object being imaged. A naïve Margosian or POCS reconstruction based on an incorrect phase map introduces severe systematic errors in the final image reconstruction.

To illustrate this potential pitfall, consider a pixel of an intermediate image reconstructed from an N-fold regularly undersampled dataset. The complex value of the pixel is the summation of the spin density (magnitude, ρ, and phase, φ) from N aliased locations labeled by indices η,

$$\rho e^{i\varphi} = \sum_{\eta=1}^{N} \rho_\eta e^{i\varphi_\eta} . \qquad [4.2]$$

The pixel phase can be written as

$$\varphi = \arctan\left(\frac{\sum_{\eta=1}^{N} \rho_\eta \sin\varphi_\eta}{\sum_{\eta=1}^{N} \rho_\eta \cos\varphi_\eta} \right). \qquad [4.3]$$

Note that the spatial variation of φ depends on the variation of the phases *and* the magnitudes at the N aliasing points. While the phase of the fully sampled image may vary slowly, it is difficult to assume that the phase of the aliased image will vary slowly as well. At high acceleration factors where N is sufficiently large, the phase φ at each aliased pixel becomes more statistically uncorrelated, and a low-resolution phase map is no longer an accurate estimate of the high-resolution version.

The phase equation (Eq. [4.3]) does not imply that a segmented partial-Fourier SENSE reconstruction will necessarily fail or cannot be modified to be more robust. When N is very small (e.g. $N = 2$), it is conceivably that the assumption for slowly varying phase may still be true in the aliased image. It should be noted, however, that for such a combination strategy, where a partial-Fourier reconstruction of an aliased image is required, disentangling the magnitude and phase information opens up the possibility of serious errors.

In this chapter, an integrated approach is proposed to combine parallel MRI and phase-constrained concepts into a single reconstruction that rigorously incorporates the phase constraint to avoid potential phase aliasing problems. In addition, this general formalism enables the reconstruction of a wide variety of *k*-space trajectories. The theory of phase-constrained parallel MR image reconstructions will be discussed, implementations in phantoms and *in vivo* will be demonstrated, caveats and limits for practical implementation will be outlined, and potential tailored sequences will be suggested. Our earlier work in this area was presented at the 2003 ISMRM conference (20). Further studies have appeared subsequently exploring combined partial-Fourier parallel MRI methods (21-23).

SECTION 4.2 Theory

4.2.a Phase-Constrained Equations and Image Reconstruction

As already stated in Eq. [1.30], the MR signal can be expressed as an integral of the spin density, ρ, against the coil sensitivity, C_l, and the complex sinusoidal modulations induced by the gradient coils,

$$s_l(\mathbf{k}) = \int e^{i\mathbf{k}\cdot\mathbf{r}} C_l(\mathbf{r})\rho(\mathbf{r})d\mathbf{r}\,, \qquad [4.4]$$

and subsequently rewritten in the form of a matrix equation:

$$\mathbf{s} = \mathbf{E}\boldsymbol{\rho}\,. \qquad [4.5]$$

where the encoding matrix, $\mathbf{E}$, which contains the coil sensitivity and gradient coil modulations, has matrix elements defined by:

$$\mathbf{E}_{(\kappa,l),\gamma} = e^{i\mathbf{k}_\kappa\cdot\mathbf{r}_\gamma} C_l(\mathbf{r}_\gamma)\,. \qquad [4.6]$$

Eq. [4.5] can be written in explicit real representation as

$$\begin{bmatrix} \mathrm{Re}(\mathbf{s}) \\ \mathrm{Im}(\mathbf{s}) \end{bmatrix} = \begin{bmatrix} \mathrm{Re}(\mathbf{E}) & -\mathrm{Im}(\mathbf{E}) \\ \mathrm{Im}(\mathbf{E}) & \mathrm{Re}(\mathbf{E}) \end{bmatrix} \begin{bmatrix} \mathrm{Re}(\boldsymbol{\rho}) \\ \mathrm{Im}(\boldsymbol{\rho}) \end{bmatrix}. \qquad [4.7]$$

Eq. [4.7] will be important for comparison with an analogous phase-constrained equation below (Eq. [4.10]).

The complex image intensity can be written in terms of its magnitude and phase: $\rho(\mathbf{r}) = \hat{\rho}(\mathbf{r})e^{i\varphi(\mathbf{r})}$, where $\hat{\rho}(\mathbf{r})$ is a real quantity proportional to the spin density, and $\varphi(\mathbf{r})$ is the image phase. We can then rewrite Eq. [4.5] as

$$\mathbf{s} = \mathbf{E}\rho = \mathbf{E}\boldsymbol{\Phi}\hat{\rho}, \qquad [4.8]$$

where $\rho \equiv \boldsymbol{\Phi}\hat{\rho}$, $\mathbf{E}\boldsymbol{\Phi}$ is the new encoding matrix, and $\boldsymbol{\Phi}$ is a diagonal matrix containing the common fully encoded (unaliased) phase with matrix elements defined by:

$$\boldsymbol{\Phi}_{\gamma\gamma'} \equiv \begin{Bmatrix} e^{i\varphi(\mathbf{r}_\gamma)}, & \gamma = \gamma' \\ 0, & \gamma \neq \gamma' \end{Bmatrix}. \qquad [4.9]$$

Eq. [4.8] is a complex matrix equation, but can be written in an explicit real representation as

$$\begin{bmatrix} \mathrm{Re}(\mathbf{s}) \\ \mathrm{Im}(\mathbf{s}) \end{bmatrix} = \begin{bmatrix} \mathrm{Re}(\mathbf{E}\boldsymbol{\Phi}) \\ \mathrm{Im}(\mathbf{E}\boldsymbol{\Phi}) \end{bmatrix} \hat{\rho}, \qquad [4.10]$$

or alternatively,

$$\bar{\mathbf{s}} = \bar{\mathbf{E}}\hat{\rho} \quad \text{where} \quad \bar{\mathbf{E}} \equiv \begin{bmatrix} \mathrm{Re}(\mathbf{E}\boldsymbol{\Phi}) \\ \mathrm{Im}(\mathbf{E}\boldsymbol{\Phi}) \end{bmatrix} \quad \text{and} \quad \bar{\mathbf{s}} \equiv \begin{bmatrix} \mathrm{Re}(\mathbf{s}) \\ \mathrm{Im}(\mathbf{s}) \end{bmatrix}. \qquad [4.11]$$

Maximal SNR is achieved by using a modified Moore-Penrose pseudoinverse (3,7)

$$\bar{\mathbf{E}}_{\text{inverse}} = \left(\bar{\mathbf{E}}^{\dagger}\bar{\boldsymbol{\Psi}}^{-1}\bar{\mathbf{E}}\right)^{-1}\bar{\mathbf{E}}^{\dagger}\bar{\boldsymbol{\Psi}}^{-1}, \qquad [4.12]$$

where $\bar{\boldsymbol{\Psi}}$ is a modified version of the noise covariance matrix (Eq. [1.42]) representing the correlation of noise between the real and imaginary channels:

$$\bar{\boldsymbol{\Psi}} = \begin{bmatrix} \left\langle \overline{\mathrm{Re}\, n_l \, \mathrm{Re}\, n_{l'}} \right\rangle & \left\langle \overline{\mathrm{Im}\, n_l \, \mathrm{Re}\, n_{l'}} \right\rangle \\ \left\langle \overline{\mathrm{Re}\, n_l \, \mathrm{Im}\, n_{l'}} \right\rangle & \left\langle \overline{\mathrm{Im}\, n_l \, \mathrm{Im}\, n_{l'}} \right\rangle \end{bmatrix} \otimes \mathbf{Id}_{\mathbf{k}}. \qquad [4.13]$$

The brackets with an overbar, $\left\langle \overline{\cdot} \right\rangle$, indicate a time average over noise samples, n. A subset of coil indices, l and l', is shown to indicate the matrix structure, and the direct product with the identity, $\mathbf{Id}_{\mathbf{k}}$, indicates that these elements are replicated for all k-space indices. This inversion, as shown, is like SENSE but can be tuned to be more SMASH-like or GRAPPA-like by inverting smaller subblocks of the encoding matrix (7). As an illustration, derivations for PARS reconstruction using a priori phase information are shown in a later section.

In practice, $\bar{\Psi}$ may be measured by acquiring noise records in all coils, (e.g. in a short noise-only scan), separating them into real and imaginary parts, and computing the relevant correlations. This procedure is essentially equivalent to the one used for unconstrained reconstructions, but with separated real and imaginary channels.

The solution vector $\hat{\rho}$ in the phase-constrained problem (Eq. [4.10]) is half the size of the solution vector in the standard problem (Eq. [4.7]). The *a priori* knowledge of the phase map has effectively eliminated half of the unknowns by setting up $\hat{\rho}$ to be strictly real. In other words, the constrained problem is twice as overdetermined as the unconstrained problem, and the level of undersampling at which the encoding matrix remains invertible is twice what it is for the unconstrained case, assuming the constraint is valid and the rows of $\bar{\mathbf{E}}$ are linearly independent (as discussed below). This implies that up to half as many *k*-space sampling points may be omitted. In additional, at a given acceleration factor, more degrees of freedom are available for SNR optimization—leading to reductions in noise amplification, as compared with the unconstrained case alone. Note also that because of the use of the generalized encoding matrix, this method allows for a one-step calculation of the noise amplification from the acquired MR signal to the final image pixel.

The expression for SNR in the constrained reconstruction is analogous to that for the unconstrained case. The SNR loss compared to a fully gradient-encoded image is quantified by the noise amplification factor, or geometry factor, g (3). In order to calculate the g-factor, we first express the noise variance, σ_γ^2, in any voxel γ of the reconstructed image as the diagonal element of a transformed noise covariance matrix, as in (3):

$$\begin{aligned}\sigma_\gamma^2 &= \left(\bar{\mathbf{E}}_{\text{inverse}}\bar{\Psi}\bar{\mathbf{E}}_{\text{inverse}}^{\dagger}\right)_{\gamma\gamma} \\ &= \left(\left(\left(\bar{\mathbf{E}}^{\dagger}\bar{\Psi}^{-1}\bar{\mathbf{E}}\right)^{-1}\bar{\mathbf{E}}^{\dagger}\bar{\Psi}^{-1}\right)\bar{\Psi}\left(\left(\bar{\mathbf{E}}^{\dagger}\bar{\Psi}^{-1}\bar{\mathbf{E}}\right)^{-1}\bar{\mathbf{E}}^{\dagger}\bar{\Psi}^{-1}\right)^{\dagger}\right)_{\gamma\gamma} \\ &= \left(\bar{\mathbf{E}}^{\dagger}\bar{\Psi}^{-1}\bar{\mathbf{E}}\right)_{\gamma\gamma}^{-1}\end{aligned} \qquad [4.14]$$

The g-factor is then proportional to the ratio of the noise standard deviation, σ_γ, to the corresponding $\sigma_\gamma^{\text{full}}$, which would have been obtained in an unaccelerated reconstruction. This ratio is scaled by the square root of the acceleration factor, R, to account for a loss in temporal averaging and yield a pure measure of the SNR loss from geometric factors alone:

$$g = \frac{1}{\sqrt{R}} \frac{\sigma_\gamma}{\sigma_\gamma^{\text{full}}}. \qquad [4.15]$$

The value of σ_γ in the numerator of Eq. [4.15] may be calculated from $\bar{\mathbf{E}}_{\text{inverse}}$ and $\bar{\Psi}$ as shown in Eq. [4.14]. The value of $\sigma_\gamma^{\text{full}}$ may be calculated using the unconstrained version of Eq. [4.14] with R=1. For k-space trajectories on a Cartesian grid, $\sigma_\gamma^{\text{full}}$ reduces to the square root of the simplified expression in Eqs. 20-21 of (3), which can be written in the current notation as

$$\sigma_\gamma^{\text{full}} = \frac{1}{\sqrt{N_{pix}}} \left(\sum_l \sum_{l'} C_l^*(\mathbf{r}_\gamma) \Psi_{ll'}^{-1} C_{l'}(\mathbf{r}_\gamma) \right)^{-1/2}. \qquad [4.16]$$

Here the elements of the standard noise resistance matrix, $\Psi_{ll'} = \langle n_l n_{l'} \rangle$, describe correlations among complex noise records, and N_{pix} is the number of pixels in the phase-encode direction.

The phase variations in Φ may arise from the transmit RF phase, gradient non-linearities, susceptibility variations, special techniques such as flow encoding, or various other sequence-dependent factors. Independently acquired phase information, for example from a body coil image, may be used to generate Φ for a phase-constrained (also referred to in this paper simply as constrained) reconstruction. Additional images are not, however, required. Measuring the coil sensitivities *in vivo* (7) can provide both the sensitivity and phase calibration.

For *in vivo* sensitivity calibration, reference component-coil images in the target image plane are obtained either from a separate acquisition (external calibration) or from a set of central k-space lines (self-calibration) (24). These reference images, which may be of

lower spatial resolution than the target image, not only can be used for sensitivity calibration but also contain information about the complex spin density. Consequently, an encoding matrix constructed using *in vivo* sensitivities already contains the phases needed for the constrained reconstruction,[11] and no phase estimation is required.

Mathematically, the *in vivo* sensitivities can be expressed as:

$$C_l^{in-vivo}(\mathbf{r}) = C_l(\mathbf{r})\rho^{low-res}(\mathbf{r}), \qquad [4.17]$$

and the MR signal equation (Eq. [4.4]) as:

$$\begin{aligned} s_l(\mathbf{k}) &= \int e^{i\mathbf{k}\cdot\mathbf{r}} C_l(\mathbf{r}) \frac{\rho^{low-res}(\mathbf{r})}{\rho^{low-res}(\mathbf{r})} \rho(\mathbf{r}) d\mathbf{r} \\ &= \int e^{i\mathbf{k}\cdot\mathbf{r}} C_l^{in-vivo}(\mathbf{r}) \frac{\rho(\mathbf{r})}{\rho^{low-res}(\mathbf{r})} d\mathbf{r}, \\ &= \int e^{i\mathbf{k}\cdot\mathbf{r}} C_l^{in-vivo}(\mathbf{r}) \rho^{quotient}(\mathbf{r}) d\mathbf{r} \end{aligned} \qquad [4.18]$$

where

$$\rho^{quotient}(\mathbf{r}) = \frac{\rho(\mathbf{r})}{\rho^{low-res}(\mathbf{r})}. \qquad [4.19]$$

Similarly, the modified encoding matrix $\mathbf{E}^{\text{in-vivo}}$ can account for the effect of the *in vivo* sensitivities:

$$\mathbf{E}_{(\kappa,l),\gamma}^{in-vivo} = e^{i\mathbf{k}_\kappa\cdot\mathbf{r}_\gamma} C_l^{in-vivo}(\mathbf{r}_\gamma). \qquad [4.20]$$

Finally, Eq. [4.5] can be rewritten as

$$\mathbf{s} = \mathbf{E}^{in-vivo}\boldsymbol{\rho}^{quotient}, \qquad [4.21]$$

The low-resolution spin density typically has the same phase variation as the full-resolution spin density, $\rho^{low-res}(\mathbf{r}) = \hat{\rho}^{low-res}(\mathbf{r})e^{i\varphi(\mathbf{r})}$, where $\hat{\rho}^{low-res}(\mathbf{r})$ is a real quantity. When this condition is in fact true, the vector $\boldsymbol{\rho}^{quotient}$ is strictly real since it is the quotient of two real quantities,

[11] With the assumptions that the phase properties of the reference and acquisition sequences match and that the resolution of the reference data is sufficient.

$$\rho^{quotient}(\mathbf{r}) = \frac{\rho(\mathbf{r})}{\rho^{low-res}(\mathbf{r})} = \frac{\hat{\rho}(\mathbf{r})e^{i\varphi(\mathbf{r})}}{\hat{\rho}^{low-res}(\mathbf{r})e^{i\varphi(\mathbf{r})}} = \frac{\hat{\rho}(\mathbf{r})}{\hat{\rho}^{low-res}(\mathbf{r})}. \quad [4.22]$$

The constrained form of Eq. [4.21] follows naturally:

$$\begin{bmatrix} \mathrm{Re}(\mathbf{s}) \\ \mathrm{Im}(\mathbf{s}) \end{bmatrix} = \begin{bmatrix} \mathrm{Re}\left(\mathbf{E}^{in-vivo}\right) \\ \mathrm{Im}\left(\mathbf{E}^{in-vivo}\right) \end{bmatrix} \boldsymbol{\rho}^{quotient}. \quad [4.23]$$

As has been described in earlier work (7), after obtaining a solution for $\rho^{quotient}(\mathbf{r})$, all factors originating from the reference spin density may be removed by post-multiplication, $\rho(\mathbf{r}) = \rho^{low-res}(\mathbf{r})\rho^{quotient}(\mathbf{r})$.[12]

4.2.b *k*-Space Trajectories and Symmetry

When using this technique only for improved parallel imaging, the benefits resulting from constrained versus unconstrained reconstruction depend both upon the sensitivity patterns of the coil array and upon the symmetry of the data about k=0. To maximally benefit from the constraint, both the real and the imaginary components of each encoding function (or, equivalently, each row of real-value $\bar{\mathbf{E}}$) should be linearly independent.

The condition of linear independence, however, breaks down in a plausible scenario when the coil sensitivity $C_l(\mathbf{r})$ is purely real *and* the sampling trajectory contains k-space conjugate pairs $\mathbf{k}_\alpha = -\mathbf{k}_\beta$, resulting degenerate encoding functions,

$$e^{i\mathbf{k}_\alpha \cdot \mathbf{r}_\gamma} C_l\left(\mathbf{r}_\gamma\right) = \left(e^{i\mathbf{k}_\beta \cdot \mathbf{r}_\gamma} C_l\left(\mathbf{r}_\gamma\right)\right)^*. \quad [4.24]$$

[12] In practice, this is done by multiplying by the square root of the sum of the squared reference images.

Numerically real sensitivities do occur in selected circumstances, for example along an axis of symmetry oriented in the direction of the main magnetic field, but in most cases of practical interest coil sensitivities will have distinct phases, allowing improved reconstruction of full-Fourier trajectories. For numerically real sensitivities, trajectories that do not include *k*-space conjugate pairs guarantee distinct encoding functions, and may yield additional gains. For complex sensitivities, the distinctness of encoding functions has a more complicated dependence on coil geometry, acceleration factor, image plane orientation, and *k*-space trajectory.

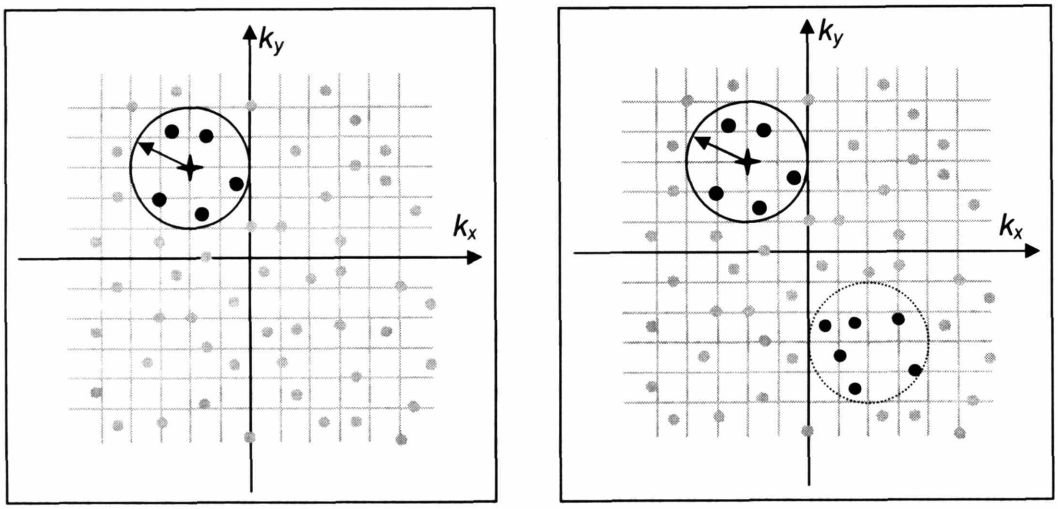

FIGURE 4.1 Schematic of PARS combined with Phase Constraint

Schematic illustration of the PARS algorithm applied without (a) and with (b) phase-constraint. *K*-space sampling locations are represented by solid dots, colored black if lying within the *k*-space radius ($k_R = 4$) and gray if lying outside. a) The original PARS selects only proximal signal data (black dots) with the circle (solid) for the reconstruction of the omitted data of interest (indicated by the star at the center). b) The combined PARS and phase-constraint adds a second circle (dotted) in the conjugate symmetric neighborhood, i.e. $(k_x, k_y) = (-k_x, -k_y)$.

4.2.c PARS Reconstruction Using A Priori Phase Information

The generalized encoding matrix formalism allows flexible combination of the phase-constraint method with a parallel imaging algorithm of choice. In particular, the

effectiveness of the PARS reconstruction (Chapter 3) can be enhanced when *a priori* phase information is available. Conceptually, the conjugate relationship places *k*-space points into the same effective neighborhood as points with inverted **k** vector, and the *k*-space locality principle can be readily extended to the conjugate neighborhood. In Fig. 4.1, the PARS sliding window is modified to incorporate the phase-constraint, in which a second circle selects relevant data in the conjugate neighborhood for PARS image reconstruction.

Derivations of the phase-constraint PARS theory are presented here. The modified MR signal equation (Eq. [4.18]), which expresses the received MR signals in terms of the *in vivo* coil sensitivities $C_l^{in-vivo}(\mathbf{r})$ and the real quantity $\rho^{quotient}(\mathbf{r})$, provides an intuitive handle to exploit conjugate symmetry, such that

$$\begin{aligned} s_l(\mathbf{k}) &= \int e^{i\mathbf{k}\cdot\mathbf{r}} C_l^{in-vivo}(\mathbf{r})\rho^{quotient}(\mathbf{r})d\mathbf{r} \\ s_l(-\mathbf{k}) &= \int e^{-i\mathbf{k}\cdot\mathbf{r}} C_l^{in-vivo}(\mathbf{r})\rho^{quotient}(\mathbf{r})d\mathbf{r} \\ s_l^*(-\mathbf{k}) &= \int \left(e^{-i\mathbf{k}\cdot\mathbf{r}} C_l^{in-vivo}(\mathbf{r})\rho^{quotient}(\mathbf{r})\right)^* d\mathbf{r} \\ &= \int e^{i\mathbf{k}\cdot\mathbf{r}} \left(C_l^{in-vivo}(\mathbf{r})\right)^* \rho^{quotient}(\mathbf{r})d\mathbf{r} \end{aligned}, \qquad [4.25]$$

where $(ab)^* = a^*b^*$ for any complex numbers a and b.

The complex conjugation of the coil sensitivities in Eq. [4.25] effectively doubles the number of encoding functions that can be used for PARS reconstruction, and the new coil sensitivities $\bar{C}_l^{in-vivo}(\mathbf{r})$ are complex conjugate pairs of the original $C_l^{in-vivo}(\mathbf{r})$:

$$\bar{C}_l^{in-vivo}(\mathbf{r}) \equiv \begin{Bmatrix} C_l^{in-vivo}(\mathbf{r}), & 1 \le l \le L \\ \left(C_{l-L}^{in-vivo}(\mathbf{r})\right)^*, & L < l \le 2L \end{Bmatrix}. \qquad [4.26]$$

Similarly, the PARS least-squares fit equation (Eq. [3.3]) is expanded to

$$\sum_{\Delta\mathbf{k}} \sum_{l'=1}^{2L} w_{\Delta\mathbf{k},l'} e^{i(-\Delta\mathbf{k})\cdot\mathbf{r}} \bar{C}_{l'}^{in-vivo}(\mathbf{r}) \approx C_l^{in-vivo}(\mathbf{r}), \qquad [4.27]$$

and the PARS reconstruction equation (Eq. [3.4]) to:

$$s_l(\mathbf{k}_{recon}) = \sum_{\Delta\mathbf{k}} \left(\sum_{l'=1}^{L} w_{\Delta\mathbf{k},l'} s_{l'}(\mathbf{k}_{recon} - \Delta\mathbf{k}) + \sum_{l'=L}^{2L} w_{\Delta\mathbf{k},l'} s_{l'-L}^*(-\mathbf{k}_{recon} - \Delta\mathbf{k}) \right), \qquad [4.28]$$

where $\|\Delta\mathbf{k}\| \leq k_R$ denotes all acquired data points within a k-space radius k_R of reconstruction $\mathbf{k}_{recon}$ and its conjugate counterpart $-\mathbf{k}_{recon}$.

In summary, as shown by Eqs. [4.27] and [4.28], the incorporation of the phase-constraint to the PARS algorithm requires minimal modification, and would merit future investigation to quantify the potential benefits.

SECTION 4.3 Methods

Simulations were performed to test the basic theory for phase-constrained parallel image reconstruction. Simulation results were then verified with phantom and *in vivo* experiments.

For the simulations in Fig. 4.2, a slowly varying phase (a linear phase ramp from $-\pi$ to π) along both axes with the period equal to the FOV) was imposed on a real-valued 64 x 64 voxel image. This complex image was multiplied by coil sensitivities calculated using the Biot-Savart Law for a planar array of four overlapping loop elements. The simulated loops were 20 cm x 9 cm, spaced by 7.2 cm in the narrow dimension, and located 10 cm from a coronal image plane. The principal axis of the array and the phase-encode axis were oriented in the left-right direction. The FOV was 30 cm square. Resulting component coil images were Fourier transformed, and various combinations of phase-encode lines were selected to mimic undersampled datasets.

For the simulations in Fig. 4.3, a real-valued 128 x 128 voxel image was multiplied by simulated coil sensitivities. The virtual array consisted of four 24 cm x 8.4 cm elements spaced by 6.72 cm, and it was situated 4.8 cm away from a coronal image plane. The FOV and orientation were the same as for Fig. 4.2. Fourier decimation was used to simulate undersampling.

The experimental phantom (Fig. 4.4) and *in vivo* data (Fig. 4.5 and Table 4.1) were acquired on a GE TwinSpeed 1.5T imaging system with EXCITE technology (GE Medical Systems, Milwaukee, Wisconsin, USA) using an FSE-XL sequence with TE = 42 ms (phantom) or 60 ms (*in vivo*), TR = 1000 ms, echo train length = 4 (phantom) or 8 (*in vivo*), bandwidth = +/-31.25 kHz, FOV = 340 mm (phantom) or 370 mm (*in vivo*), slice thickness = 5 mm, and matrix size = 256 x 128 (phantom) or 256 x 192 (*in vivo*). These data were acquired using a custom designed coil array (Nova Medical, Inc., Wakefield, Massachusetts, USA) with four independently-positionable 89 mm x 178 mm rectangular elements and low input-impedance preamplifiers. The elements were arranged in a non-overlapping fashion in the left-right direction across the bottom of the phantom or the back of a healthy volunteer. The image plane was coronal and parallel to the array plane. Two separate fully sampled data sets were acquired in each case. One was Fourier decimated to yield regularly undersampled data (e.g. for R=4 in Fig. 4.4, every fourth phase-encode line was used, for a total of 32). The other was used for coil sensitivity and phase calibration. This method provides an identical target image for various sampling and reconstruction schemes allowing straightforward comparison, while in theory mimicking the exact behavior of directly acquired aliased data. The calibrations for Fig. 4.4 and Table 4.1 employed full resolution along the phase-encode direction. Calibration data for Fig. 4.5 had one-twelfth the spatial resolution of the undersampled data in the phase-encode direction.

Images were generated using both phase-constrained and unconstrained reconstructions. The traditional encoding matrix $\mathbf{E}$ or the constrained encoding matrix $\bar{\mathbf{E}}$ was formed as outlined in the *Theory* section, inverted, and multiplied by the appropriate signal vector to yield an image. A serial combination of standard Margosian (10) and unconstrained reconstructions was used for Fig. 4.2. g-factor maps were calculated using Eq. [4.15]. Changes in SNR relative to baseline (R=1) images that result from noise amplification can be computed from the inverse of the ratio of noise levels, $SNR/SNR^{full}=\sigma^{full}/\sigma$(3). The g-factor already contains this information (Eq. [4.15]), and thus was used to compute the decreases in SNR shown in Table 4.1 (see Eq. 24 from (3)):

$$\left\langle \frac{SNR}{SNR^{(R=1)}} \right\rangle_{pix} = \left\langle \frac{1}{g} \right\rangle_{pix} \frac{1}{\sqrt{R}} . \qquad [4.29]$$

Here the angle brackets represent an average over all pixels. Average increases in SNR resulting from application of the phase constraint were computed by averaging a pixel-by-pixel ratio of the unconstrained to constrained g-factor maps over the image plane

$$\left\langle \frac{SNR^{pc}}{SNR^{uc}} \right\rangle_{pix} = \left\langle \frac{g^{uc}}{g^{pc}} \right\rangle_{pix}, \qquad [4.30]$$

where *pc* (*uc*) stands for phase-constrained (unconstrained). For unaccelerated magnitude images, the SNR was calculated by selecting signal and noise-only regions and accounting for the Rician distribution of noise using the methods in (25).

SECTION 4.4 Results

Fig. 4.2 demonstrates how a simple serial combination of partial-Fourier and image-space parallel reconstructions can introduce errors. In this case, the Margosian reconstruction of an aliased image, (a), does not faithfully reproduce the original partial-FOV image, (b), even though the full-FOV image phase is slowly varying. The errors seen in (a) are propagated through the unconstrained parallel reconstruction, (d), but do not appear in the constrained reconstruction, (e). The central eight lines of the phase were used for the constrained reconstruction—the same number of lines used by the Margosian (even-numbered lines of the central 16). The simulated phase here is slowly varying—completely specified in the central eight lines of the Fourier transform. The standard single-coil Margosian reconstruction is shown for reference in Fig. 4.2c.

Fig. 4.3 displays g-factor maps for simulations using unconstrained and phase-constrained reconstructions with different two-fold and three-fold undersampling schemes. The 1st and 3rd columns contain the results for a phase-encode scheme with lines placed symmetrically about k=0 (each line +k has a paired conjugate line –k) for R=2 and R=3, respectively. The 2nd and 4th columns contain results for corresponding asymmetric (unpaired) phase-encode schemes. Grayscale images of the g-factor are shown for unconstrained and constrained reconstructions. Note that R=2 plots are scaled differently than R=3 plots for better visualization. As expected, noise amplification is reduced with

constrained versus unconstrained reconstruction for all trajectories shown (mean g labeled below each plot). It can also be seen that the noise amplification is reduced most for the asymmetric trajectories.

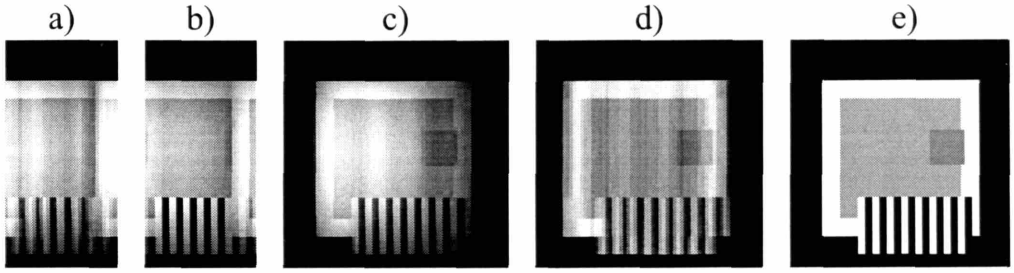

FIGURE 4.2 Simulations of Partial Fourier Image Reconstructions

Simulated illustration of partial-Fourier error when reconstructing an aliased image. Half-FOV images from one component coil are shown comparing a) a Margosian reconstructed half-FOV image using even lines k={–8,–6...28,30} to b) the original half-FOV image, lines k={–32,–30...28,30}. c) A single coil standard Margosian reconstruction of lines k={–4,–3...29,30} is shown for reference. Full-FOV images reconstructed from lines k={–8,–6...28,30} are shown using: d) serial Margosian and unconstrained reconstructions and e) phase-constrained reconstruction (with low-resolution phase calibration). Phase-encode direction is left-right.

Fig. 4.4 displays phase-constrained reconstructions of four-coil phantom data with acceleration factors ranging from one to eight. Unconstrained images for R of one to four show the usual degradation in SNR as the acceleration factor approaches the total number of coils. In comparison, the constrained reconstructions show a more gradual degradation in apparent SNR as the acceleration factor is increased. Additionally, the constrained reconstructions here remain artifact-free up to R=8 (twice the coil count). Fig. 4.5 illustrates the improved image quality for *in vivo* four-coil data with fixed acceleration, R=4, using a coil/phase calibration at one-twelfth resolution along the phase encode axis (i.e. 16 phase encode lines were used for calibration).

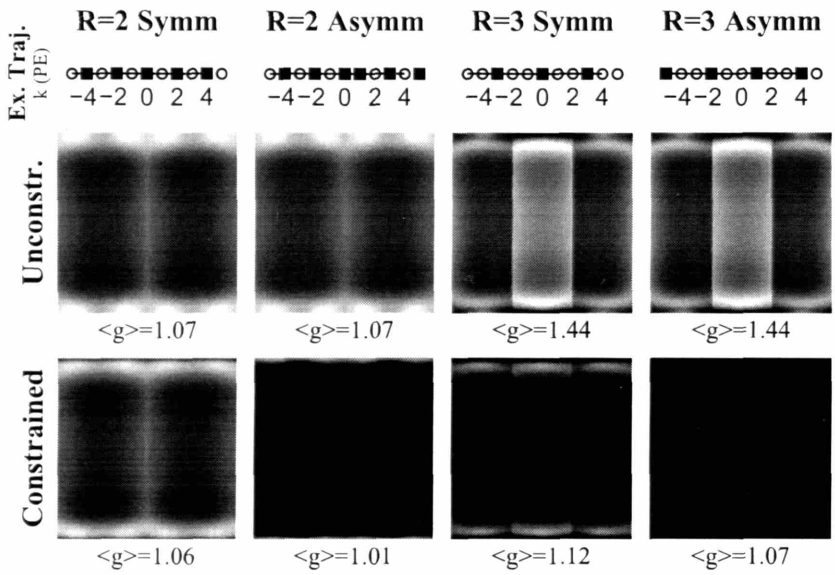

FIGURE 4.3 Noise in Parallel Image Reconstructions with and without Phase Constraint

Comparison of noise amplification using unconstrained and phase-constrained parallel image reconstructions for simulated data at two-fold and three-fold acceleration. The selected undersampling schemes are: *R*=2 symmetric (1st column), *R*=2 asymmetric (2nd column), *R*=3 symmetric (3rd column), and *R*=3 asymmetric (last column). Simplified illustrations of each phase encoding (PE) trajectory is shown along the top row. Solid squares (empty circles) indicate data points acquired (skipped). Second and third row: g-factor maps for unconstrained and constrained reconstructions, respectively, with mean g-factor labeled below each. Note: *R*=3 plots are scaled differently than *R*=2 plots.

Rows 1 and 2 of Table 4.1 quantify, for an *in vivo* dataset, the decrease in average SNR at acceleration factors of one to four resulting from g-factor alone (described above and seen qualitatively in Fig. 4.4). These numbers are relative to the SNR of the respective R=1 reconstruction for each method, estimated to be 54 and 75 for the unconstrained and constrained methods, respectively. This difference results from a noise filtering effect (discussed later) intentionally excluded from these calculations. Row 3 of Table 4.1 illustrates the average increase in SNR from applying the constraint for R =1 to 4, again only including g-factor effects.

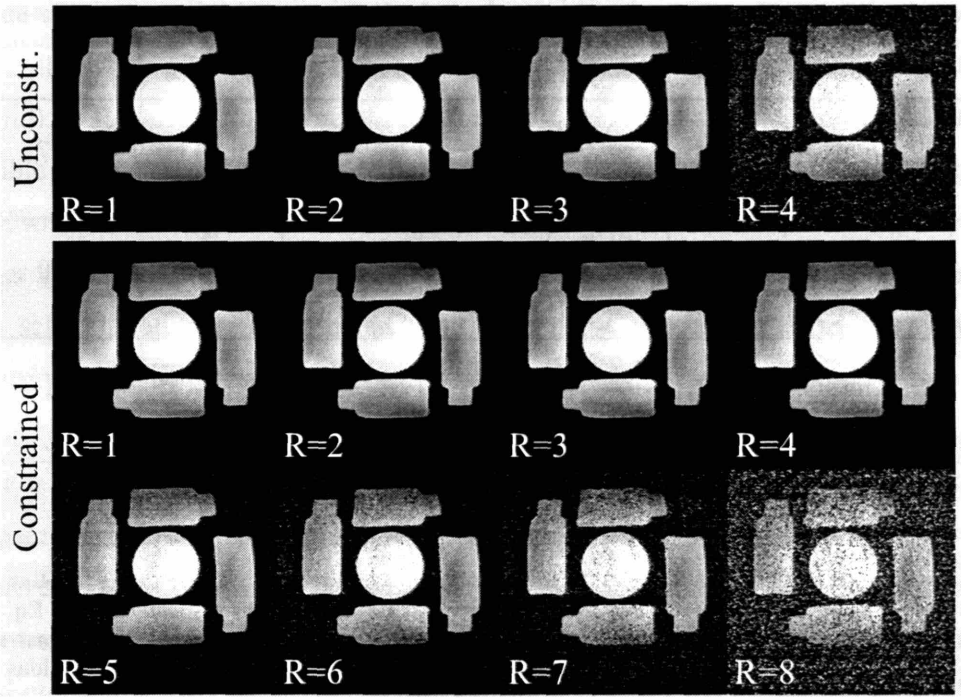

FIGURE 4.4 Phantom Images from Phase-Constraint Parallel Image Reconstructions

Phantom images from constrained parallel reconstructions (bottom two rows) of four-channel data with acceleration factor, *R*, of 1 through 8. Unconstrained reconstructions are shown in the top row for *R* of 1 through 4.

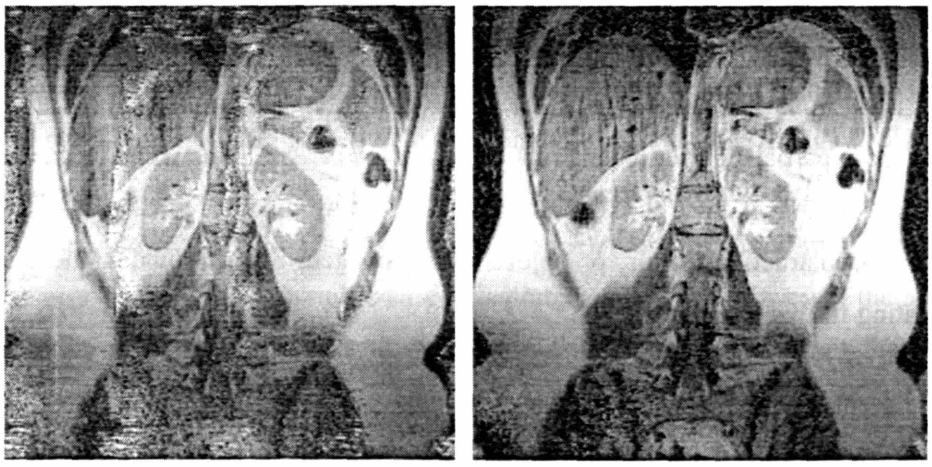

FIGURE 4.5 In-Vivo Images from Phase-Constraint Parallel Image Reconstructions

Accelerated *in vivo* images with *R*=4 and four coils comparing unconstrained (left) and constrained (right) reconstructions. 16 phase encode lines were used for coil and phase calibration.

	R=1	R=2	R=3	R=4
Unconstrained SNR, $\left\langle \frac{SNR}{SNR^{(R=1)}} \right\rangle_{pix}$	1	0.643	0.417	0.244
Constrained SNR, $\left\langle \frac{SNR}{SNR^{(R=1)}} \right\rangle_{pix}$	1	0.675	0.500	0.372
Change in SNR, $\left\langle \frac{SNR^{pc}}{SNR^{uc}} \right\rangle_{pix}$	1	1.06	1.24	2.05

TABLE 4.1 Changes in SNR with Increasing Acceleration Factor for *in vivo* Data.

The second and third rows show the degradation in average SNR relative to the baseline (R=1) images using unconstrained and phase-constrained reconstructions respectively (see Eq. [4.29]). The fourth row shows the average increase in SNR of the phase-constrained reconstruction (*pc*) versus the unconstrained reconstruction (*uc*) (see Eq. [4.30]). All calculations show relative changes that result from noise amplification (g-factor) alone.

SECTION 4.5 Discussion

The phase-constrained parallel image reconstruction method presented in this chapter provides an integrated combination of partial-Fourier and parallel imaging techniques that offers a rigorous incorporation of the phase constraint and is capable of avoiding errors arising from partial-Fourier reconstruction of aliased images. The potential for these errors is illustrated in Fig. 4.2. The example of Fig. 4.2 may not be representative of all partial-Fourier reconstructions, coils, or objects being imaged, but it provides anecdotal evidence motivating further exploration.

From the point of view of partial-Fourier imaging, our reconstruction can be viewed as a generalized phase-constrained reconstruction with coil sensitivities included as prior information. From the point of view of parallel imaging, the constraint assists in generating skipped lines in a new way–through conjugate symmetry. For traditional partial-Fourier trajectories (i.e. for trajectories with sampling omitted on one side of k-space), use of this

conjugate symmetry provides essentially the same result as a straightforward combination of parallel MRI with partial-Fourier reconstruction (assuming that such a combination is successful). However, the generalized form of the reconstruction proposed here is compatible with many different types of undersampled k-space trajectories. For example, we have shown results using full-Fourier trajectories (i.e. both sides of k-space sampled) which are either symmetric or asymmetric about k=0. Variable-density trajectories (such as those used in self-calibrating reconstructions) and even non-Cartesian trajectories may also be treated using the same formalism.

For the purposes of exploring this new reconstruction, we have chosen in most cases to compare its performance to standard full-Fourier SENSE reconstruction. This serves as a good reference point for which we can quantify meaningful performance related factors such as noise amplification. We have demonstrated that, as expected, when a phase constraint is imposed on parallel MRI reconstructions, lower noise amplifications (see Fig. 4.3 and Table 4.1) and higher achievable net acceleration factors (see Fig. 4.4) are observed.

For the asymmetrically sampled full-Fourier cases, such as those represented in the second and fourth columns of Fig. 4.3, some component of the reduced noise amplification could likely be achieved by combining partial-Fourier and parallel MR reconstructions in a two-step fashion (with a cautionary reminder of the possibility for errors). In such cases, for example, separate partial-Fourier reconstructions could be performed on both halves of the data yielding a symmetric data set suitable for image-domain parallel image reconstruction. In the second column of Fig. 4.3, the interlaced placement of acquired and corresponding conjugate lines allows the filling of lines using symmetry alone, which may explain the g factor very near one. In the symmetric cases illustrated in Fig. 4.3, however, the Margosian cannot generate any missing lines, and the improvements result only from the combined effects of coil sensitivity information (mixing predominantly nearby k-space lines) and conjugate symmetry (mixing only conjugate lines). For such trajectories, one might consider using a more general partial-Fourier reconstruction algorithm, such as POCS, in combination with parallel imaging. Such a combination, however, would also not involve simple sequential application of existing techniques. The POCS-SENSE algorithm (23), for

example, requires recasting the parallel image reconstruction in terms of an interactively applied projection.

Phase-constrained reconstruction gives improved SNR compared with unconstrained reconstruction even for R=1 images, despite identical unitary g-factors. The constrained inversion intrinsically eliminates the imaginary channel noise. This results in an approximate $\sqrt{2}$ reduction in noise as compared with an unconstrained magnitude image containing noise from both real and imaginary channels. Of course, the component of the improvement in SNR that results from noise filtering could also be accomplished by rephasing an unconstrained reconstruction and taking its real part. This baseline improvement, then, is not unique to the constrained case, and it was excluded from the calculations for Table 4.1. One benefit of the constrained technique, however, is that this rephasing occurs automatically.

Sensitivity to phase errors is the principal weakness of this proposed technique. The phase information must be accurate and works best when the underlying phase is slowly varying and motion between the calibration and the accelerated scan is minimal. Tissue interfaces with large susceptibility discontinuities can result in rapid phase variations, posing problems for low-resolution phase maps. The amount of phase calibration information required depends on many factors and was not specifically explored in this study. The limitations of phase calibration need to be explored further, along with possible solutions such as phase extrapolation or smoothing.

SECTION 4.6 Conclusions

Results from simulations and *in vivo* experiments have been presented to illustrate specific benefits of phase-constrained parallel image reconstructions. The general formalism of the technique enables the combination of partial-Fourier and parallel MR imaging into a single-step exact-inversion method and enables the use of non-Cartesian sampling schemes that cannot be handled using traditional combinations of parallel MRI and partial-Fourier reconstructions. As a consequence of the phase constraint, the solution vector in the constrained inversion problem is reduced in size, and the inversion is more overdetermined

than in the unconstrained case. This results in more available degrees of freedom in the inversion to minimize noise amplification. Aside from improving SNR compared with the unconstrained reconstructions without partial-Fourier, this also allows the extension of achievable undersampling factors beyond the total number of coils used, even for acquisition trajectories that would not normally allow additional acceleration using partial-Fourier techniques. This technique can also be used to avoid potential errors introduced by serial combinations of partial-Fourier and SENSE-like reconstructions. One important limitation which is common among any phase-constrained reconstruction methods, however, is the necessity for accurate phase calibration data.

Chapter 4 References

1. Sodickson DK, Manning WJ. Simultaneous acquisition of spatial harmonics (SMASH): fast imaging with radiofrequency coil arrays. Magn Reson Med 1997;38(4):591-603.
2. Jakob PM, Griswold MA, Edelman RR, Sodickson DK. AUTO-SMASH: a self-calibrating technique for SMASH imaging. MAGMA 1998;7:42-54.
3. Pruessmann KP, Weiger M, Scheidegger MB, Boesiger P. SENSE: sensitivity encoding for fast MRI. Magn Reson Med 1999;42(5):952-962.
4. Griswold MA, Jakob PM, Nittka M, Goldfarb JW, Haase A. Partially parallel imaging with localized sensitivities (PILS). Magn Reson Med 2000;44(4):602-609.
5. Kyriakos WE, Panych LP, Kacher DF, Westin CF, Bao SM, Mulkern RV, Jolesz FA. Sensitivity profiles from an array of coils for encoding and reconstruction in parallel (SPACE RIP). Magn Reson Med 2000;44(2):301-308.
6. Sodickson DK. Tailored SMASH Image Reconstructions for Robust In Vivo Parallel MR Imaging. Magn Reson Med 2000;44:243-251.
7. Sodickson DK, McKenzie CA. A generalized approach to parallel magnetic resonance imaging. Med Phys 2001;28(8):1629-1643.
8. Heidemann RM, Griswold MA, Haase A, Jakob PM. VD-AUTO-SMASH imaging. Magn Reson Med 2001;45(6):1066-1074.
9. Griswold MA, Jakob PM, Heidemann RM, Nittka M, Jellus V, Wang J, Kiefer B, Haase A. Generalized autocalibrating partially parallel acquisitions (GRAPPA). Magn Reson Med 2002;47(6):1202-1210.
10. Liang Z-P, Boada FE, Constable RT, Haacke EM, Lauterbur PC, Smith MR. Constrained Reconstruction Methods in MR Imaging. Reviews of Magnetic Resonance in Medicine 1992;4:67-185.
11. Margosian P, Schmitt F, Purdy DE. Faster MR imaging: Imaging with half the data. Health Care Instrum 1986;1:195-197.
12. Noll DC, Nishimura DG, Macovski A. Homodyne detection in magnetic resonance imaging. IEEE Trans Med Imag 1991;MI-10:154-163.
13. Cuppen JJ, Van Est A. Reducing MR imaging time by one-sided reconstruction.; 1987; Cleveland, Ohio.

14. Youla DC, Webb H. Image restoration by the method of convex projections: Part 1 -- Theory. IEEE Trans Med Imag 1982;MI-1:81-94.
15. Sezan MI, Stark H. Image restoration by the method of convex projections: Part 2 -- Applications and numerical results. IEEE Trans Med Imag 1982;MI-1:95-101.
16. Sezan MI, Stark H. Tomographic image reconstruction from incomplete view data by complex projections and direct Fourier inversion. IEEE Trans Med Imag 1984;MI-3:91-98.
17. Weiger M, Pruessmann KP, Boesiger P. Cardiac real-time imaging using SENSE. SENSitivity Encoding scheme. Magn Reson Med 2000;43(2):177-184.
18. Griswold MA, Jakob PM, Chen Q, Goldfarb JW, Manning WJ, Edelman RR, Sodickson DK. Resolution enhancement in single-shot imaging using simultaneous acquisition of spatial harmonics (SMASH). Magn Reson Med 1999;41(6):1236-1245.
19. Heidemann RM, Griswold MA, Kiefer B, Nittka M, Wang J, Jellus V, Jakob PM. Resolution enhancement in lung 1H imaging using parallel imaging methods. Magn Reson Med 2003;49(2):391-394.
20. Willig-Onwuachi JD, Yeh EN, Grant AK, Ohliger MA, McKenzie CA, Sodickson DK. Phase-constrained parallel MR image reconstruction: using symmetry to increase acceleration and improve image quality. 2003; Toronto, Ontario, Canada. p 19.
21. Bydder M, Robson MD. Partial Fourier partially parallel imaging. 2004; Kyoto, Japan. p 532.
22. Lew C, Spielman D, Bammer R. TurboSENSE: phase estimation in temporal phase-constrained parallel imaging. 2004; Kyoto, Japan. p 2646.
23. Samsonov A, Kholmovski E, Johnson C. Phase-constrained reconstructon of sensitivity-encoded MRI data with POCSENSE. 2004; Kyoto, Japan. p 2647.
24. McKenzie CA, Yeh EN, Ohliger MA, Price MD, Sodickson DK. Self-calibrating parallel imaging with automatic coil sensitivity extraction. Magn Reson Med 2002;47(3):529-538.
25. Gudbjartsson H, Patz S. The Rician distribution of noisy MRI data. Magn Reson Med 1995;34(6):910-914.

CHAPTER 5. GENERALIZED NOISE ANALYSIS FOR MAGNITUDE IMAGE COMBINATION WITH PARALLEL MRI[13]

This chapter develops a generalized method to analyze the noise statistics in parallel image reconstructions which involve magnitude combinations of intermediate solutions for the generalized MR matrix equation, $\mathbf{s} = \mathbf{E}\boldsymbol{\rho}$. These magnitude operations irreversibly transform the underlying complex Gaussian noise statistics, requiring modification of the traditional noise analysis shown in Eq. [1.46]. For the general case of magnitude-combined images, a numerical strategy is developed to compute the new noise distribution. Analytic solutions are noted for special cases which can be expressed in terms of Rayleigh, Ricean, modified Bessel functions.

SECTION 5.1 Introduction

Even though MR images are generally complex, magnitude MR images are often viewed and analyzed in clinical setting. The traditional practice of reading x-ray images on films, which are strictly magnitude images, probably gave rise to radiologists' preference for

[13] The work in this chapter has been presented as "Yeh EN, McKenzie CA, Grant AK, Ohliger MA, Willig-Onwuachi JD, Sodickson DK. Generalized Noise Analysis for Magnitude Image Combination in Parallel MRI. Proc. 11th Annual Meeting ISMRM; 2003; Toronto, Canada. p 21."

magnitude MR images. Hence, the noise distribution in magnitude MR images is an important determinant of perceived image quality. Magnitude noise distributions for conventional (non-parallel) MRI were studied in Refs. (1,2). For individual images, the magnitude operation transforms a complex Gaussian (normal) variate to a Ricean variate (1). When component coil images from an RF coil array are combined as the sum-of-square magnitudes, the distribution is described by a modified Bessel function of the first kind (2).

Two critical assumptions were made in Ref. (2). It was assumed that the noise at a given pixel position across the component coil images was a) uncorrelated and b) of identical variance. For conventional MRI, this can be accomplished in theory by decorrelating noise in signal data from different component coils prior to the reconstruction of individual coil images. The two critical assumptions can then be satisfied, and the noise analysis method described by Ref. (2) can be applied in the final sum-of-squares composite image. However, in practice, noise decorrelation is rarely performed, except in the context of parallel imaging.

In parallel imaging methods that perform coil-by-coil reconstruction followed by a sum-of-squares combination (3-5), the two assumptions just described no longer hold, even when the noise in the component-coil signal data is decorrelated prior to image reconstruction. Coil-by-coil reconstructions have certain advantages (e.g., improved least-squares fits for the block-diagonalization approaches such as PARS), and a final composite image is subsequently obtained by sum-of-squares combination. As illustrated in Fig. 5.1, intermediate images are typically targeted to emulate coil-modulated images, but they can emulate other profiles as well. For this type of image reconstruction approach, parallel image reconstruction invariably re-introduces noise correlation across the intermediate images. In addition, the noise amplitude varies from one coil to the next and from one pixel to the next in the reconstructed image.

To date, no noise analysis tool has been developed for sum-of-squares parallel imaging. Instead, an alternative method of measuring the total error power in reconstructed images is used (Eq. [3.12]). This empirical method calculates the total error power of

parallel MR images based on an unaccelerated reference. In the event that obtaining an unaccelerated reference is not feasible (e.g. when parallel imaging is a necessity instead of an option), or when motion spoils the comparison between referenced and accelerated images, the error power method cannot be applied. A comprehensive and rigorous analysis method is required in order to assess the general behavior and practical performance of sum-of-squares parallel imaging techniques, and to enable future research in areas such as noise filter design.

In this chapter, the noise characteristics of magnitude images are generalized for both parallel and non-parallel imaging. A numerical approach is proposed for the general case, while analytic solutions are derived for three special cases. Calculation of noise amplification (*g*-factor) for magnitude images is demonstrated using the new noise analysis tool, and an SNR-optimal *k*-space radius for the PARS technique (Chapter 3) is determined.

SECTION 5.2 Theory

5.2.a Noise Decorrelation

The MR signal data $s_l(k)$, received by coil l at k-space position k, has a noise covariance matrix $\boldsymbol{\Psi}$ described by Eq. [1.42]. This noise covariance matrix $\boldsymbol{\Psi}$ can be eliminated by creating noise-decorrelated signal data $s_l^{decorr}(k)$ using the Cholesky decomposition process previously described in Eq. [1.44]. The signal data to be used in subsequent derivations will be taken to be noise-decorrelated, and the superscript will be dropped to simplify the notation.

5.2.b Reconstruction of Intermediate Images

The reconstruction of an intermediate image can be expressed as a matrix operation,

$$\boldsymbol{\rho}^{(l)} = \mathbf{E}_{inverse}^{(l)}\mathbf{s} \qquad [5.1]$$

where $\boldsymbol{\rho}^{(l)}$ is the vector representing the intermediate image l , and $\mathbf{E}_{inverse}^{(l)}$ is the reconstruction matrix computed by a parallel MRI technique of choice (e.g., PARS or GRAPPA). It should be noted that even though the number of intermediate images generally equals the number of physical coils L, this is not a requirement. Since there is no noise correlation in **s**, the noise covariance matrix between the pixels in the intermediate images l and l' can be expressed as:

$$\boldsymbol{\Theta}^{(l,l')} = \mathbf{E}_{inverse}^{(l)} \left(\mathbf{E}_{inverse}^{(l')} \right)^{H} \qquad [5.2]$$

For example, the noise covariance between pixel γ in image l and pixel γ' on image l' is defined as,

$$\sigma^2 (l,l',\gamma,\gamma') \equiv \left[\boldsymbol{\Theta}^{(l,l')} \right]_{(\gamma,\gamma')} . \qquad [5.3]$$

5.2.c Sum-of-Squares Combinations

Until now, we have used only linear operations in our reconstruction, and the noise distribution in each image pixel remains Gaussian. However, the sum-of-squares combination that follows will transform the noise characteristics to a non-analytic expression in general.

Sum-of-squares combinations, despite their nonlinearity, are preferred over linear phased-sum combinations in order to eliminate the potential risk of phase cancellation due to coil sensitivity modulation (3). The final solution vector $\boldsymbol{\rho}^{(SOS)}$ is obtained by element-wise sum-of-squares combination of the intermediate solution vectors $\boldsymbol{\rho}^{(l)}$ at each pixel position γ,

$$\boldsymbol{\rho}_{\gamma}^{(SOS)} = \sqrt{\sum_{l=1}^{L} \left| \boldsymbol{\rho}_{\gamma}^{(l)} \right|^2} . \qquad [5.4]$$

The flow diagram in Fig. 5.1 schematically summarizes coil-by-coil parallel image reconstruction approaches.

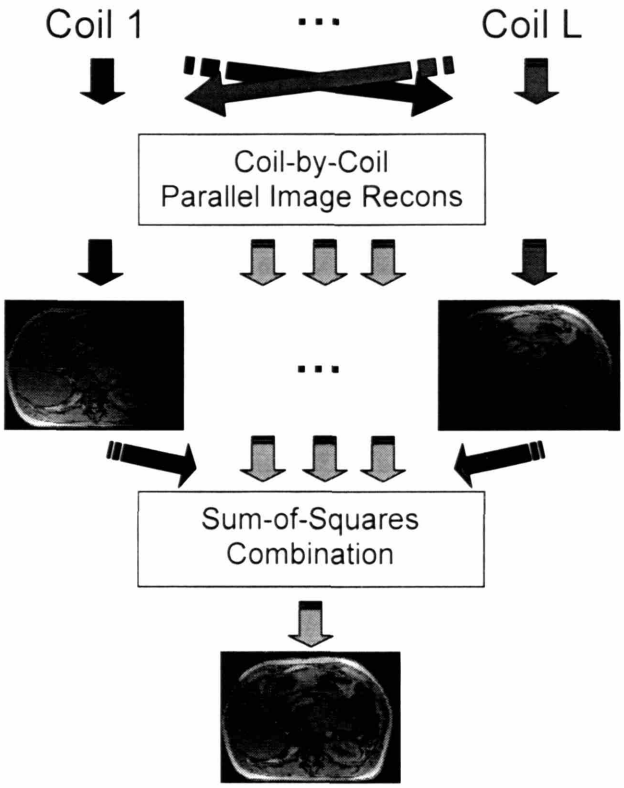

FIGURE 5.1 Schematic of Sum-of-Squares Combined Parallel Image Reconstruction

Schematic illustration of the coil-by-coil approach used by parallel image reconstruction techniques such as PARS and GRAPPA. Intermediate coil images are first reconstructed in order to improve the least-squares fits used SMASH, GRAPPA and PARS. The underlying object in these intermediate images is modulated by the corresponding coil sensitivity, and the coil sensitivities have different phases. A simple-sum combination of the intermediate images risks potential phase cancellation. Instead, a sum-of-squares combination is typically performed to obtain the final composite image.

5.2.d Notational Convention for Random Variables

The remaining sections of this chapter, as well as the appendices, are devoted to technical aspects of the proceeding discussion. In order to enhance readability and allow easy reference to standard literature, we adopt a common convention for random variables, such that italic capital letters (e.g., X, Y, Z) denote random variables, and the corresponding italic lowercase letters (e.g., x, y, z) denote sample values and dummy arguments. The

probability density function (pdf) of random variable X is denoted as $p_X(x)$, with mean, m_x, and variance, σ_x^2. We refer to the Fourier transform of a variable's pdf as its "characteristic function," denoted as $\phi_X(j\omega)$. Vectors of random variables will be denoted using bold lowercase letters (e.g., **x, y, z**), where $\mathbf{x} = [X_1, X_2, \ldots, X_n]^T$,with mean vector, $\mathbf{m}_x$, and covariance matrix $\mathbf{\Psi}_x$. The notation $\mathbf{x} \sim N(\mathbf{m}_x, \mathbf{\Psi}_x)$ is used for random variable vectors of Gaussian (normal) distributions. Table 5.1 summarizes the random variable notation convention used in this chapter.

Random Variable	X
Sample Values and Dummy Arguments	x
Probability Density Function (pdf)	$p_X(x)$
Characteristic Function	$\phi_X(j\omega)$
Mean and Variance	m_x and σ_x^2
Mode	$mode(x) = \arg\max_x p_X(x)$
Vector of Random Variables	$\mathbf{x} = [X_1, X_2, \ldots, X_n]^T$
Mean Vector and Covariance Matrix	$\mathbf{m}_x$ and $\mathbf{\Psi}_x$
Gaussian (Normal) Distribution	$\mathbf{x} \sim N(\mathbf{m}_x, \mathbf{\Psi}_x)$

TABLE 5.1 Notational Convention for Random Variables

5.2.e Changes of Variables

To simplify the noise analysis in Eq. [5.4], we will consider only one particular pixel position γ_o. New variable names are introduced in order to eliminate the irrelevant indices,

$$\begin{aligned} R &\equiv \boldsymbol{\rho}_{\gamma_o}^{(SOS)}, \\ Z_l &\equiv \boldsymbol{\rho}_{\gamma_o}^{(l)} \end{aligned} \qquad [5.5]$$

Eq. [5.4] is reformatted,

$$R = \sqrt{\sum_{l=1}^{L} Z_l^* Z_l} \qquad [5.6]$$

The random variable R is the perceived intensity of pixel γ_o on the sum-of-squares combined image. The probability density function, $p_R(r)$, is to be determined. The Z_l's have complex Gaussian distributions, with mean vector $\mathbf{m}_z$ and covariance matrix $\boldsymbol{\Psi}_z$, or equivalently in our convention, $\mathbf{z} = [Z_1, Z_2, \ldots, Z_L]^T$ and $\mathbf{z} \sim N(\mathbf{m}_z, \boldsymbol{\Psi}_z)$. Conceptually, the elements of $\mathbf{m}_z$ are the values of pixel γ_o for each component coil image. Mathematically, $\mathbf{m}_z$ is expressed as,

$$\mathbf{m}_z = \left[\left[\mathbf{E}_{inverse}^{(1)} \mathbf{E}\boldsymbol{\rho} \right]_{\gamma_o}, \left[\mathbf{E}_{inverse}^{(2)} \mathbf{E}\boldsymbol{\rho} \right]_{\gamma_o}, \ldots, \left[\mathbf{E}_{inverse}^{(L)} \mathbf{E}\boldsymbol{\rho} \right]_{\gamma_o} \right]^T \qquad [5.7]$$

and the entry (l,l') of $\boldsymbol{\Psi}_z$ is extracted from Eq. [5.2],

$$\boldsymbol{\Psi}_z(l,l') = \sigma^2(l,l',\gamma_o,\gamma_o) = \left[\boldsymbol{\Theta}^{(l,l')} \right]_{\gamma_o\gamma_o}. \qquad [5.8]$$

Since $\boldsymbol{\Psi}_z$ is a Hermitian matrix, we can use a similarity transformation (Ref. (6), Section 5.5, Property 4) to find $\boldsymbol{\Lambda}$ and $\mathbf{Q}$ such that

$$\boldsymbol{\Psi}_z = \mathbf{Q}\boldsymbol{\Lambda}\mathbf{Q}^H, \qquad [5.9]$$

where $\mathbf{Q}$ is an orthogonal matrix $\left(\mathbf{Q}^{-1} = \mathbf{Q}^H\right)$, and $\boldsymbol{\Lambda}$ is a diagonal matrix with non-negative entries $\lambda_\eta = \boldsymbol{\Lambda}_{ll}$. Now, define $\boldsymbol{\chi} = \boldsymbol{\Lambda}^{-1/2}\mathbf{Q}^{-1}\mathbf{z}$, and where $\boldsymbol{\chi} = [\chi_1, \chi_2, \ldots, \chi_L]^T$ and $\boldsymbol{\chi} \sim N(\mathbf{m}_\chi, \boldsymbol{\Psi}_\chi)$, $\mathbf{m}_\chi = \boldsymbol{\Lambda}^{-1/2}\mathbf{Q}^{-1}\mathbf{m}_z$ and

$$\begin{aligned}\boldsymbol{\Psi}_{\chi} &= \boldsymbol{\Lambda}^{-1/2}\mathbf{Q}^{-1}\boldsymbol{\Psi}_{z}\left(\boldsymbol{\Lambda}^{-1/2}\mathbf{Q}^{-1}\right)^{H} \\ &= \boldsymbol{\Lambda}^{-1/2}\boldsymbol{\Lambda}\left(\boldsymbol{\Lambda}^{-1/2}\right)^{H} \\ &= \mathbf{Id}\end{aligned} \qquad [5.10]$$

Eq. [5.6] can be expressed in terms of the new variable,

$$\begin{aligned}R &= \sqrt{\sum_{l=1}^{L} Z_l^* Z_l} = \sqrt{\mathbf{z}^H \mathbf{z}} \\ &= \sqrt{\left(\mathbf{Q}\boldsymbol{\Lambda}^{1/2}\boldsymbol{\chi}\right)^H \mathbf{Q}\boldsymbol{\Lambda}^{1/2}\boldsymbol{\chi}} \\ &= \sqrt{\boldsymbol{\chi}^H \boldsymbol{\Lambda}\boldsymbol{\chi}} = \sqrt{\sum_{l=1}^{L} \lambda_l \chi_l^* \chi_l} = \sqrt{\sum_{l=1}^{L} \lambda_l \chi^2_{2,|m_{\chi l}|}}\end{aligned} \qquad [5.11]$$

Because χ_l's are uncorrelated Gaussian variates, each term $\chi^2_{2,|m_{\chi l}|}$ is a non-central chi-square variate, where the notation $\chi^2_{d,m}$ uniquely defines the variate χ^2 with d degrees of freedom and a noncentrality parameter m^2. Now R is expressed as the root of a linear combination of independent non-central chi-square variates.

5.2.f A Numerical Method to Compute the Probability Density Function of R

The pdf $p_R(r)$ for R does not have an analytic expression in general. However, $p_R(r)$ can be numerically computed using the following method.

First, the characteristic function, $\phi_Y(j\omega)$, of random variable Y, where $Y = R^2$, has an analytic expression as shown in Eq. [5.51] in Appendix B. (Appendices A and B provide detailed derivations of $\phi_Y(j\omega)$.) The pdf of Y, $p_Y(y)$, can be obtained numerically by performing a fast Fourier transform (FFT) on discretized $\phi_Y(n)$,

$$\phi_Y(n) = \phi_Y(jn\Delta\omega), \qquad n = 0, \pm 1, \pm 2, \ldots \qquad [5.12]$$

where $\Delta\omega$ represents a sufficiently small frequency interval.

After finding $p_Y(y)$, a change of variables can be applied to compute $p_R(r)$ using the following relationships in the corresponding cumulative density functions (cdf),

$$\int_0^R p_R(r)\,dr = \int_0^Y p_Y(y)\,dy, \qquad [5.13]$$

where

$$dy = 2r dr. \qquad [5.14]$$

The mean of R, m_r, can be computed by performing a simple numerical integration,

$$m_r = E[R] = \int_0^\infty r p_R(r)\,dr, \qquad [5.15]$$

and the variance of R, σ_r^2 can be calculated using

$$\begin{aligned} \sigma_r^2 &= E\left[R^2\right] - \left(E[R]\right)^2 \\ &= E[Y] - (m_r)^2 \\ &= \phi_Y(j\omega)\big|_{j\omega=0} - (m_r)^2 \end{aligned} \qquad [5.16]$$

Finally, the "perceived SNR" is expressed in terms of m_r and σ_r^2 as

$$perceived\ SNR = \frac{m_r}{\sqrt{\sigma_r^2}}, \qquad [5.17]$$

while the g-factor calculation adapted from Eq. [1.49] is expressed as

$$g = \sqrt{\frac{\sigma_{accel}^2}{\sigma_{ref}^2} \cdot \frac{1}{AccelFactor}}, \qquad [5.18]$$

where σ_{accel}^2 and σ_{ref}^2 are the noise variances of the accelerated and reference images, respectively, calculated using Eq. [5.16], and *AccelFactor* is the acceleration factor.

5.2.g Analytic Expressions for Special Cases

There are three special cases in which $p_R(r)$ does have analytic expressions. First, if the pixel γ_0 is in a noise-only region, the non-centrality parameter m^2 becomes zero, and $\chi^2_{2,m_{\chi_l}}$ degenerates to a central chi-square variate $\chi^2_{2,0}$. In this case, $p_R(r)$ can be expressed as a weighted sum of Rayleigh distributions (Appendix A, Eq. [5.43]),

$$p_R(r) = \sum_{l=1}^{L} \frac{q_l r}{\lambda_l} e^{-r^2/2\lambda_l}, \quad r \geq 0 \qquad [5.19]$$

where

$$q_l = \prod_{k,k\neq l}^{L} \frac{1}{1-(\lambda_k/\lambda_l)}. \qquad [5.20]$$

Also, the n^{th} moment, $E[R^n]$, also has an analytic expression,

$$E[R^n] = \sum_{l=1}^{L} q_l (2\lambda_l)^{n/2} \Gamma(1+n/2), \qquad [5.21]$$

where $\Gamma(\cdot)$ is the gamma function. Eq. [5.21] can be used to calculate the mean and variance of R.

In the second special case, parallel imaging techniques that directly reconstruct to one final image without going through intermediate coil images (e.g. SENSE (7)) fall under the trivial degenerate case for which $L = 1$ and R is a scaled Ricean variate, as already shown in Ref. (1) and also in Appendix B, Eq [5.50].

Finally, for parallel image reconstruction using the PILS technique (8) and also non-parallel image reconstruction in general, the diagonal matrix in the similarity transformation (Eq. [5.9]) , $\mathbf{\Lambda}$, is a scalar multiple of the identity matrix, i.e. $\lambda_l = \lambda_0$. Eq. [5.11] can be simplified to,

$$R = \sqrt{\sum_{l=1}^{L} \lambda_l \chi^2_{2,|m_{\chi l}|}}$$
$$= \sqrt{\lambda_o} \sqrt{\sum_{l=1}^{L} \chi^2_{2,|m_{\chi l}|}}, \qquad [5.22]$$
$$= \sqrt{\lambda_o} \sqrt{\chi^2_{2L,\mathbf{m}_\chi^H \mathbf{m}_\chi}}$$

where the new chi-square variate $\chi^2_{2L,\mathbf{m}_\chi^H \mathbf{m}_\chi}$ is of $2L$ degrees of freedom and noncentrality parameter $\mathbf{m}_\chi^H \mathbf{m}_\chi$. The expression of $p_R(r)$ assumes the form that has been derived in Ref. (2), which is also shown in Eq. [5.48] in Appendix B.

SECTION 5.3 Methods

Simulations and *in vivo* experiments were performed, and 2-fold accelerated parallel image reconstructions were performed using the sum-of-squares PARS method. Individual component coil images were first reconstructed to offset approximations inherent in the assumption of *k*-space locality, and then combined as the sum-of-squares in order to eliminate potential phase cancellations.

SIMULATIONS

For simulations, sensitivities of a 6-element rectangular coil array were generated using a Biot-Savart algorithm. Each array element measured 180x80mm, and the array covered a total extent of 180x393mm. A 2-fold accelerated MR dataset was simulated (400x400 mm Field of View, 256 x 256 matrix). A *k*-space radius of 4 was used in the PARS reconstruction. And without any loss of generality, the noise covariance matrix of simulated signal data was set to the identity. As discussed in the Theory section, noise in acquired signal data can be decorrelated by a Cholesky decomposition prior to image reconstruction. The use of the identity noise matrix in simulated data serves to simplify the analysis.

After the generation of signal data, coil-by-coil PARS image reconstructions were performed, and the component coil images were combined using sum-of-squares. The noise covariance matrices Ψ_y of the component coil images were calculated using the PARS reconstruction weights (as shown in Eq. [5.8]). Two pixel positions were considered: the central pixel (128,128) and a ¼ FOV off-center pixel (128, 192).

The pdf of the perceived intensity, $p_R(r)$, is expected to vary both with actual object intensity (due to the nonlinear transformations described above) and with pixel position (due to spatially varying weights in the parallel image reconstruction). Thus, $p_R(r)$ was calculated for actual object intensities ranging from 0 to 6, for both pixel positions.

In Vivo Experiments

In vivo data were acquired on a Siemens Symphony 1.5T MR imaging system (Siemens Medical Systems, Iselin, NJ, USA) with a maximum gradient strength of 30mT/m and a rise time of 300 μsec. One reference image and one two-fold accelerated image volume were acquired with a commercially available four-element body array (2 anterior and 2 posterior elements, each element measured 140x135mm) using Volumetric Interpolated Breath-hold Examination (VIBE) (9) (TR 4.2 ms, TE 1.88 ms, 12° flip angle, 180 mm thick slab, 72 partitions, 225×300 mm Field of View, 146×256 matrix, 2.5×1.54×1.17 mm spatial resolution).

PARS reconstructions using various *k*-space radii were performed. For the image reconstructed using *k*-space radius of 4, g-factors were obtained using both the traditional ROI method and the numerical method proposed in Section 5.2.f. Additionally, the median and mean *g*-factor values for PARS reconstructions using *k*-space radii ranging from 2 to 20 were calculated and plotted for analysis.

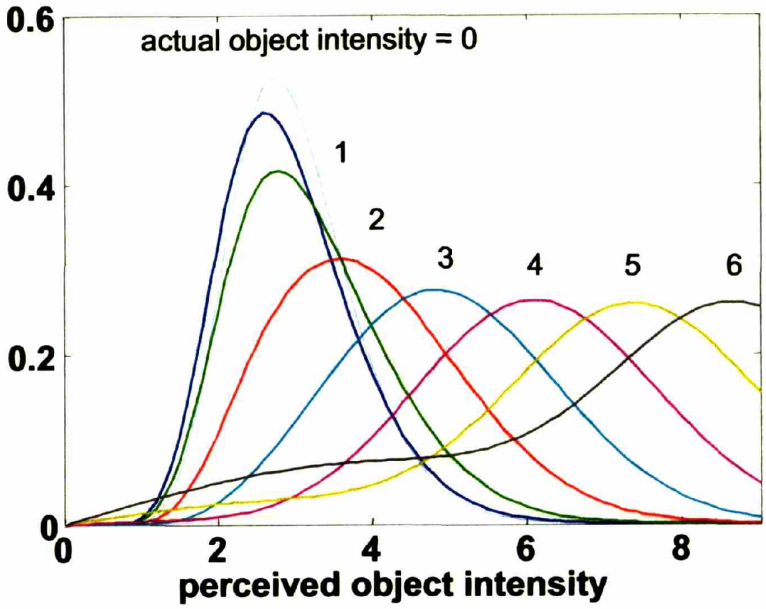

FIGURE 5.2 Probability Density Functions of Perceived Image Intensity

Probability density functions of the perceived image intensity in a simulated 2-fold accelerated PARS image reconstruction. Solid lines represent the pdf of the central image pixel and dashed lines represent the pdf of a pixel offset by ¼ of the FOV from that central pixel. Because of the magnitude operations involved in the image reconstruction, the pdf no longer assumes a Gaussian distribution. As shown by the different shapes of pdf's, the perceived noise variances would also depend on the actual underlying image intensity (illustrated by the different widths of the peaks) and the position of the pixel (illustrated by the dashed and solid lines).

SECTION 5.4 Results

Fig. 5.2 shows the probability density functions of the perceived image intensity in a simulated 2-fold accelerated PARS image reconstruction. Solid lines represent the pdf of the central image pixel and dashed lines represent the pdf of a pixel offset by ¼ of the FOV from that central pixel. It is important to note that prior to the sum-of-squares combination, each image pixel of a component coil image has a complex Gaussian pdf whose mean corresponds to the actual coil-modulated spin density. However, the sum-of-squares combination transforms the complex image pixel to the magnitude image pixel, which assumes a strictly positive real value. As illustrated, the perceived image intensity has a non-Gaussian pdf, and the mean of the pdf no longer corresponds to the actual image intensity. Also, the noise

variances vary depending on the actual underlying image intensity (illustrated by the different widths of the peaks) and the position of the pixel (illustrated by the dashed and solid lines). It should be clear from this figure that a g-factor calculation using the ROI method would not provide an accurate answer.

Fig. 5.3 plots the statistical biases between the perceived and actual intensities. The generalized noise analysis used the noise covariance matrix of the central pixel in the 2-fold accelerated in vivo image reconstructed by PARS ($k_R = 4$). Statistical biases were calculated by subtracting the actual image intensity from the mode and mean of the perceived image intensity and were plotted on a linear scale (a). Fractional biases were calculated by dividing the absolute biases over the actual image intensity and were plotted on a semi-logarithmic scale (b).

Fig. 5.4 qualitatively compares the PARS reconstructions of 2-fold accelerated *in vivo* data using various *k*-space radii: $k_R = 2$ (a), 4 (b), 20 (c). Intermediate coil images were first reconstructed and then combined using the sum-of-squares. Upon visual inspection, (a) and (b) have comparable image quality, while (c) has an elevated noise floor. A quantitative method, such as g-factor calculation using the proposed generalized noise analysis, is required to characterize the difference between (a) and (b).

Fig 5.5 demonstrates two methods to determine g-factor. The first method (a) used a region-of-interest (ROI) approach, which estimated the SNR of the reconstructed image by manually defining a noise-dominant region and a signal-dominant region and measuring the noise and signal power in respective regions. The g-factor was erroneously determined to be less than 1, the theoretical lower bound. The second method (b) used the numerical method proposed in Section 5.2.f to calculate the noise power directly in the signal-dominant region. The g-factor was then computed using the generalized noise statistics.

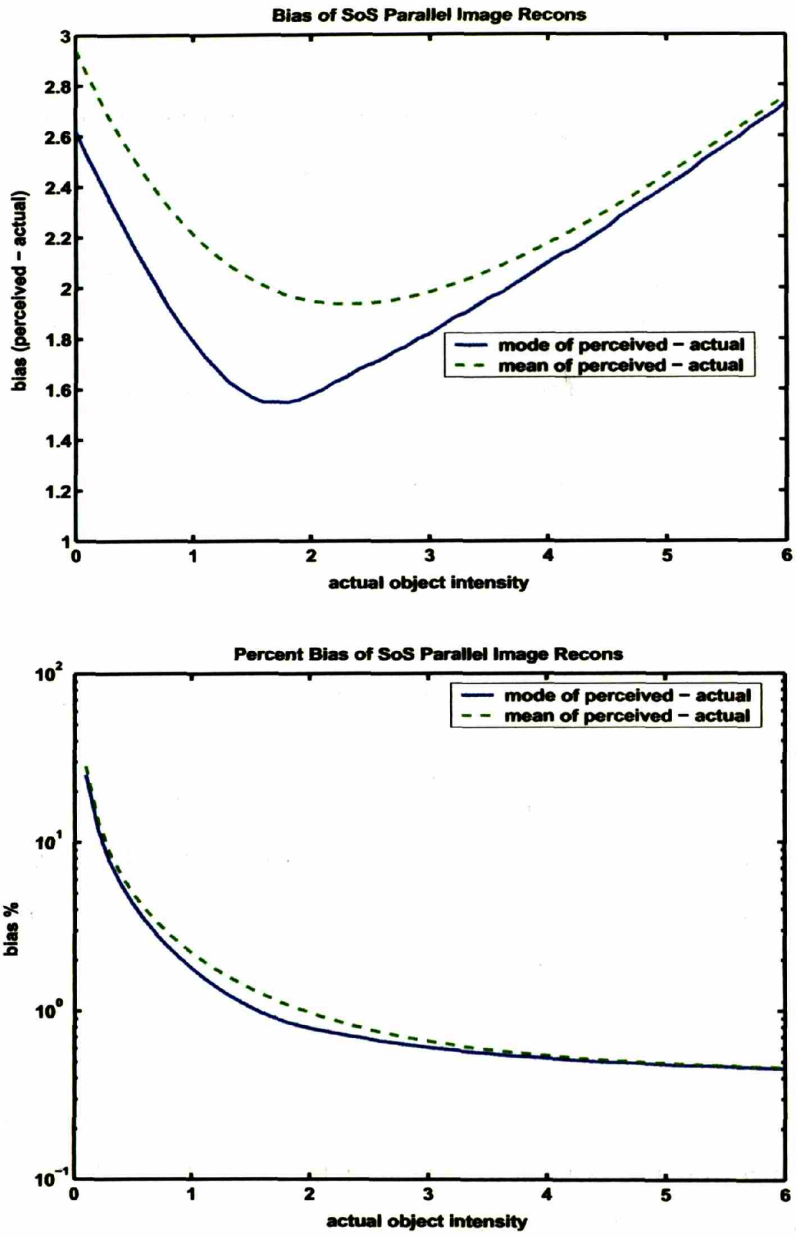

FIGURE 5.3 Statistical Biases of Perceived Image Intensity

Statistical biases between the perceived and actual intensity. Biases were calculated by subtracting the actual image intensity from the mode and mean of the perceived image intensity and were plotted on a linear scale (a). Fractional biases were calculated by dividing the absolute biases over the actual image intensity and were plotted on a semi-logarithmic scale (b).

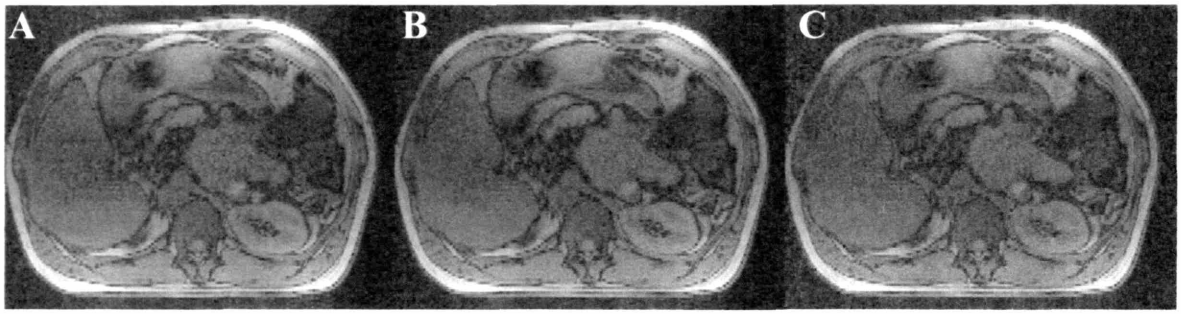

FIGURE 5.4 Image Comparison of Sum-of-Squares PARS Image Reconstructions

Qualitative image comparison of PARS reconstructions. Images were reconstructed from 2-fold accelerated *in vivo* data using PARS *k*-space radii of 2 (a), 4 (b), and 20 (c). Intermediate coil images were first reconstructed and then combined sum-of-squares. a and b have comparable image quality, while c has an elevated noise floor.

Fig. 5.6 plots the mean and median g-factors of PARS reconstructions of *in vivo* data as a function of *k*-space radius. 2-fold accelerated *in vivo* images were reconstructed using *k*-space radii ranging from 2 to 20, and the g-factors of the images were computed pixel-by-pixel using the proposed generalized noise analysis method in Section 5.2.f. The mean and median of the g-factors in a PARS reconstructed image were determined and plotted according to the *k*-space radius used in the reconstruction. The g-factor plots correctly predict the visually noticeable elevation of noise background in Fig. 5.3c compared to Figs. 5.3a and 5.3b. In addition, these plots provide a quantitative comparison between Fig 5.2a and Fig 5.2b that would be difficult to distinguish by visual inspection. This analysis shows that the optimal k-space radius for PARS (i.e., the radius that minimizes the g-factor) is k_R = 4.

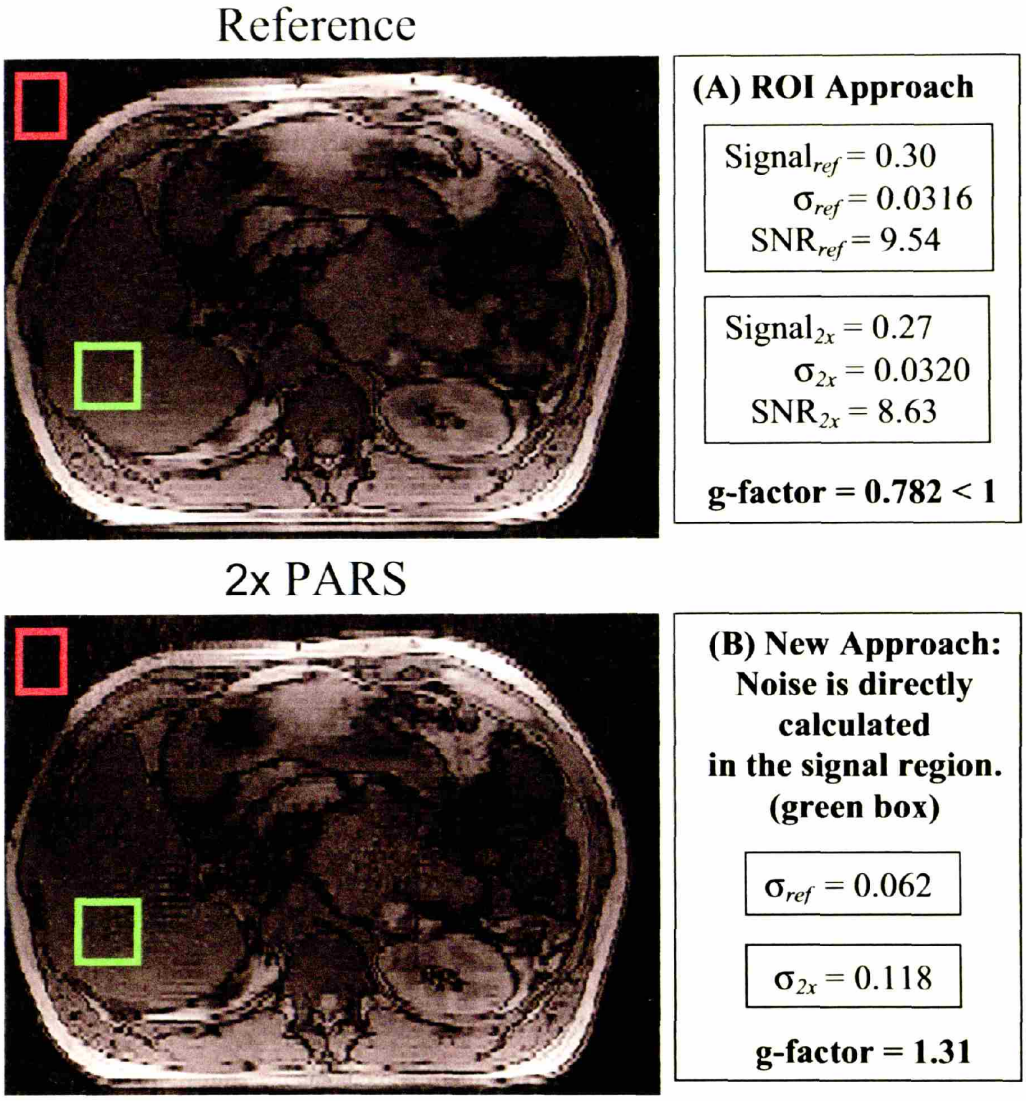

FIGURE 5.5 Comparison of G-factors Obtained by ROI and the proposed Numerical Method

Demonstration of two methods to determine g-factor. The first method (a) used a region-of-interest (ROI) approach, which estimated the SNR of the reconstructed image by manually defining a noise-dominant region (red boxes) and a signal-dominant region (green boxes) and measuring the noise and signal power in the respective regions. The g-factor was erroneously determined to be less than 1, the theoretical lower bound. The second method (b) used the generalized noise analysis method to calculate the noise power in the signal-dominant region, and used that to determine the g-factor.

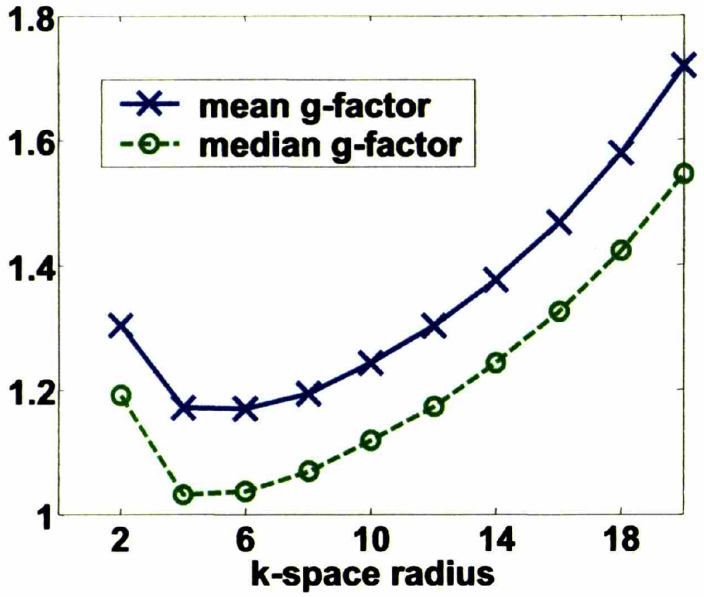

FIGURE 5.6 Calculated G-factors vs k-space Radius

The mean and median g-factors were plotted as functions of *k*-space radii. The PARS technique reconstructed 2-fold accelerated *in vivo* datasets using *k*-space radii ranging from 2 to 20. G-factors were calculated one pixel location at a time using the proposed generalized noise analysis method. The mean and median of the g-factors of a PARS reconstructed image were determined, and were plotted according to the k-space radius used in the reconstruction.

SECTION 5.5 Discussion

5.5.a Bias in Noise-dominant Region and Signal-dominant Region

As shown in Fig. 5.3, the bias introduced by the sum-of-squares combination displays different characteristics in the noise- and signal-dominant regions. In noise-dominant region, the bias can be estimated by the Rayleigh equations (Eqs. [5.19]-[5.21]). In the intermediate region where the noise power and the actual object intensity are comparable, the bias reaches a minimum at an actual object intensity of roughly 2 (in units where the noise variance is 1), while the fractional bias decreases monotonically. As the object intensity continues to increase, the bias increases in direct proportion to the object intensity, and Fig. 5.3b illustrates that the fractional bias asymptotically approaches 0.4%.

While Fig. 5.3 represents the results of one *in vivo* experiment of a particular acceleration factor, it is reasonable to expect that the general trend of these results can be applied to current parallel MRI techniques where the number of elements and the factor of achieved acceleration are relatively small. For highly accelerated parallel MRI with many-element coil arrays, it can be speculated that the same general trend may still be applied. The physical attenuation of coil sensitivities, commonly referred as the PILS effect (8) where coils that are positioned proximal to the image pixel will contribute the most in the reconstruction of the coil-by-coil image reconstruction, will naturally limit the number of effective coils in the coil-by-coil image reconstruction. However, future studies are required to verify these conjectures.

5.5.b Intensity Correction Using a Maximum Likelihood Estimation Method

An *a posteriori* intensity correction can be performed to eliminate the intensity bias in order to enhance image contrast. In particular, the noise-dominant region will benefit the most because this is the region with the largest fractional bias. The bias function, $b(r)$, can be determined using a maximum likelihood (ML) estimation method,

$$s_{ML}(r) = \underset{s \in \text{ all possible } s}{\arg\max}\ p_{(r|s)}(r|s), \qquad [5.23]$$

and

$$b(r) = r - s_{ML}(r), \qquad [5.24]$$

where R is the perceived object intensity, and $s_{ML}(r)$ is the ML estimator of the actual object intensity, S. More discussion on the ML estimation is deferred to Chapter 7.

It should be noted even though the bias function varies pixel to pixel, it only varies slowly (except at sharp aliasing boundaries) because the coil sensitivities used in spatial encoding also vary slowly. A similar trend has been observed in Fig. 5.2 that the pdf's at pixel positions separated by a quarter field-of-view only vary slightly. The bias function calculated for a particular pixel location can be applied to its proximal neighbors. Therefore,

once a small but clinically interesting region is identified, *a posteriori* intensity correction can be applied, and image contrast can be enhanced in that region. On the other hand, if a systematic bias correction is needed for the entire image, selected pixel locations representing different regions can be selected to generate bias functions for their corresponding neighborhoods.

5.5.c Computational Requirement for Numerical Integration

Numerical integration was used to derive the probability distribution function and also the noise characteristics for the general case where the analytical expressions given above are not applicable. The computation time for the numerical method for a 2-D image set was in the order of minutes when implemented using MATLAB (MathWorks, Natick, MA, USA) on a Windows-based AMD Athlon XP 2500+ system. With appropriate code optimization and translation to a low-level language such as C, the projected computation time may be short enough to permit implementation as an interactive tool for real-time clinical applications.

5.5.d g-factor Calculation and Optimal PARS k-Space Radius

A theoretically-consistent g-factor (>1) was calculated using the method proposed, whereas the g-factor derived from the ROI approach was incorrect. The ability to explicitly calculate g-factor for sum-of-squares parallel MRI allows a common quantitative metric to be used across parallel MRI techniques. Perhaps more importantly, the g-factor calculation provides a means for internal optimization. For example, an SNR-optimal *k*-space radius of PARS can be determined by plotting the g-factors at various k-space radii. Similarly, the GRAPPA algorithm, which relies on a less rigorously defined SNR optimization technique to resolve over-determinacy, can use the g-factor metric for optimization.

It should be noted, however, that the g-factor has limited physical meaning since it only accounts for the amplification of the noise variances. In magnitude-combined parallel image reconstructions, the non-Gaussian noise can no longer be completely characterized

using only the variance. A g-factor analysis should be supplemented by other statistical methods such as the bias estimation/correction.

SECTION 5.6 Conclusions

A theoretical model of noise statistics has been derived for sum-of-squares-combined parallel image reconstructions. The g-factor map of magnitude images can be explicitly computed at any given underlying object intensity. While the general case requires numerical methods, analytic expressions exist for three special cases. For the PARS reconstruction, the SNR-optimal *k*-space radius is predicted based upon the knowledge of the coil sensitivities and an estimate of the underlying object intensity. An additional benefit is anticipated for non-Cartesian parallel imaging: proposed iterative reconstruction algorithms for non-Cartesian trajectories do not allow calculation of a g-factor, but g-factor maps are now available for non-Cartesian PARS reconstructions. Thus, this generalized noise analysis tool will enable quantitative SNR analysis for parallel imaging techniques, coil geometries, and *k*-space trajectories of choice.

SECTION 5.7 Appendix A

DERIVATION OF CENTRAL CHI SQUARE DISTRIBUTION WITH DISTINCT VARIANCES

Traditionally, a central chi-square random variable Y is constructed by:

$$Y = \sum_{n} Z_i^2 \qquad [5.25]$$

with the Z_i, $i = 1, 2, ..., n$, being statistically independent and identically distributed Gaussian random variables with zero mean and variance σ^2. When $n = 1$, the probability density function (pdf) can be expressed as:

$$p_Y(y) = \frac{1}{\sqrt{2\pi y}\sigma} e^{-\frac{y}{2\sigma^2}}, \qquad y \geq 0, \qquad [5.26]$$

and the characteristic function:

$$\begin{aligned} \phi_Y(j\omega) &= \int_{-\infty}^{\infty} e^{j\omega y} p_Y(y)\, dy \\ &= \frac{1}{\left(1 - j\omega 2\sigma^2\right)^{1/2}} \end{aligned} \qquad [5.27]$$

Because of the statistical independence, in cases $n > 1$, the characteristic function becomes:

$$\phi_Y(j\omega) = \frac{1}{\left(1 - j\omega 2\sigma^2\right)^{n/2}}. \qquad [5.28]$$

Equation [5.28] has a well-known inverse Fourier transform,

$$p_Y(y) = \frac{1}{\sigma^n 2^{n/2} \Gamma\left(\frac{n}{2}\right)} y^{n/2-1} e^{-y/2\sigma^2}, \qquad y \geq 0. \qquad [5.29]$$

When $n = 2$, i.e. $Y = X_1^2 + X_2^2$, the pdf becomes:

$$p_Y(y) = \frac{1}{2\sigma^2} e^{-\frac{y}{2\sigma^2}}, \qquad y \geq 0. \qquad [5.30]$$

Now, suppose we define a new random variable

$$R = \sqrt{Y} = \sqrt{Z_1^2 + Z_2^2}. \qquad [5.31]$$

By a change of variables in Eq. [5.30], we obtain a Rayleigh distribution:

$$p_R(r) = \frac{r}{\sigma^2} e^{-\frac{r^2}{2\sigma^2}},\ r \geq 0. \qquad [5.32]$$

For magnitude image of a single coil receiver, this Rayleigh distribution governs the noise in image regions when no MR signal is present (1). Here, Z_1 and Z_2 represent the real and imaginary components of a noise-only pixel. For an array with L receivers, we can similarly express the sum-of-squares Y in the noise-only region as:

$$Y = \sum_{l=1}^{L} \left(Z_l^{real}\right)^2 + \left(Z_l^{imag}\right)^2. \qquad [5.33]$$

Substituting $2L = n$ to Equation [5.29], we get

$$p_Y(y) = \frac{1}{\sigma^{2L} 2^L \Gamma(L)} y^{L-1} e^{-\frac{y}{2\sigma^2}}, \qquad y \geq 0. \qquad [5.34]$$

This derivation has been shown in Ref. (2). Here, Eq. [5.34] assumes two conditions: 1) the noise received by each coil is statistically independent, 2) the noises across the receivers have identical variance. In the derivation below, we proceed to relax the second condition.

Suppose each channel (real or imaginary) has distinct variance σ_i^2. The characteristic function then becomes:

$$\phi_Y(j\omega) = \prod_{i=1}^{n} \frac{1}{\left(1 - j\omega 2\sigma_i^2\right)^{1/2}}. \qquad [5.35]$$

However, since it is generally true that the real and imaginary noises received by the same RF coil would have identical variances σ_l, we can rewrite Equation [5.35] as:

$$\phi_Y(j\omega) = \prod_{l=1}^{L} \frac{1}{\left(1 - j\omega 2\sigma_l^2\right)}. \qquad [5.36]$$

Eq. [5.36] assumes the following general form:

$$f(x) = \prod_{L} \frac{1}{(x - a_l)}, \qquad [5.37]$$

and by the partial fraction expansion, Eq. [5.37] can be expressed as:

$$f(x) = \sum_{L} \frac{b_l}{(x - a_l)}, \qquad [5.38]$$

where b_l's are computed by evaluating $f(x)$ at the removable singularities,

$$b_l = \left[(x-a_l) f(x)\right]_{x=a_l}. \qquad [5.39]$$

Equation [5.36] can be expressed in terms of as a summation,

$$\phi_Y(j\omega) = \sum_{l=1}^{L} \frac{q_l}{\left(1-j\omega 2\sigma_l^2\right)}, \qquad [5.40]$$

where q_l's are the appropriate coefficients determined by partial fraction expansion by substituting σ_l^2 in place of b_l. Now each of the terms in the summation series is just the characteristic function of a Rayleigh distribution of variance σ_l^2. Taking the advantage of linearity, the inverse Fourier transform yields:

$$p_Y(y) = \sum_{l=1}^{L} \frac{q_l}{2\sigma_l^2} e^{-\frac{y}{2\sigma_l^2}},\ y \geq 0. \qquad [5.41]$$

Equivalently, we can express R and its pdf as follows:

$$R = \sqrt{Y} = \sqrt{\sum_{l=1}^{L} \left(Z_l^{real}\right)^2 + \left(Z_l^{imag}\right)^2}, \qquad [5.42]$$

and

$$p_R(r \mid \boldsymbol{\sigma}) = \sum_{l=1}^{L} \frac{q_l r}{\sigma_l^2} e^{-\frac{r^2}{2\sigma_l^2}},\ r \geq 0. \qquad [5.43]$$

Interestingly enough, the final pdf is expressed in terms of a weighted sum of the pdf's of Rayleigh distributions with variance σ_l^2.

SECTION 5.8 Appendix B

DERIVATION OF NON-CENTRAL CHI SQUARE DISTRIBUTION WITH DISTINCT MEANS AND DISTINCT VARIANCES

To generalize further from the results of Appendix A, we can derive the pdf for non-central chi square distribution with distinct variances. To begin, we define a random variable Y such that:

$$Y = \sum_{n} Z_i^2 \qquad [5.44]$$

with the X_i, $i = 1, 2, ..., n$, being statistically independent Gaussian random variables with distinct means m_i and distinct variance σ_i^2. When $n = 1$, the probability pdf can be expressed as:

$$p_Y(y) = \frac{1}{\sqrt{2\pi y}\sigma} e^{-\frac{(y+m^2)}{2\sigma^2}\cosh\left(\frac{\sqrt{y}m}{\sigma^2}\right)}, \qquad y \geq 0, \qquad [5.45]$$

The characteristic function associated with the pdf in Eq. [5.45] is

$$\begin{aligned} \phi_Y(j\omega) &= \int_{-\infty}^{\infty} e^{j\omega y} p_Y(y)\, dy \\ &= \frac{1}{\left(1 - j\omega 2\sigma^2\right)^{1/2}} e^{\frac{j\omega m^2}{\left(1 - j\omega 2\sigma^2\right)}}. \end{aligned} \qquad [5.46]$$

We note here that when $m = 0$, Eqs. [5.45] and [5.46] readily degenerate to Eqs. [5.26] and [5.27] respectively. Once again by the argument of statistical independence, in cases $n > 1$, the characteristic function becomes:

$$\phi_Y(j\omega) = \prod_{i=1}^{n} \frac{1}{\left(1 - j\omega 2\sigma_i^2\right)^{1/2}} e^{\frac{j\omega m_i^2}{\left(1 - j\omega 2\sigma_i^2\right)}}. \qquad [5.47]$$

Further simplification of Eq. [5.47] is possible should the variances σ_i's be identical (2).

$$p_Y(y) = \frac{1}{2\sigma^2}\left(\frac{y}{s^2}\right)^{(n-2)/4} e^{-\left(s^2+y\right)/2\sigma^2} I_{n/2-1}\left(\sqrt{y}\frac{s}{\sigma^2}\right), \quad y \geq 0, \qquad [5.48]$$

where $I_m(\cdot)$ is the m-th order modified Bessel function of the first kind. In particular, for the case $n = 2$ and $\sigma_1 = \sigma_2 = \sigma$ (1), we obtain the pdf and the characteristic equation of Y as:

$$p_Y(y) = \frac{1}{2\sigma^2} e^{-\frac{(s^2+y)}{2\sigma^2}} I_0\left(\sqrt{y}\frac{s}{\sigma^2}\right), \quad y \geq 0$$
$$\phi_Y(j\omega) = \frac{1}{(1-j\omega 2\sigma^2)} e^{\frac{j\omega s^2}{(1-j\omega 2\sigma^2)}} \quad , \qquad [5.49]$$

where $s^2 = m_1^2 + m_2^2$. With a change of variable $R = \sqrt{Y} = \sqrt{Z_1^2 + Z_2^2}$, we arrive at the Ricean distribution:

$$p_R(r) = \frac{r}{\sigma^2} e^{-\frac{(s^2+r^2)}{2\sigma^2}} I_0\left(\frac{rs}{\sigma^2}\right), \quad y \geq 0. \qquad [5.50]$$

When $s = 0$, Eq. [5.50] reduces to Eq. [5.32], the Rayleigh distribution (1).

Now, we are ready to derive the pdf of the sum-of-squares Y of an L-coil array with noise of distinct means m_i and distinct variances σ_i. To begin, let each coil have two independent noise channels (real and imaginary) of the identical variance σ_l^2. Letting $2L = n$, we can rewrite Eq. [5.47] as:

$$\phi_Y(j\omega) = \prod_{l=1}^{L} \frac{1}{(1-j2\omega\sigma_l^2)} e^{\frac{j\omega s_l^2}{(1-j2\omega\sigma_l^2)}} , \qquad [5.51]$$

where $s_l^2 = \left(m_l^{real}\right)^2 + \left(m_l^{imag}\right)^2$. The pdf of Y is obtained by taking the inverse Fourier transform of Eq. [5.51].

$$p_Y(y) = \frac{1}{2\pi} \int_{-\infty}^{\infty} \phi_Y(j\omega) e^{-j\omega y} d\omega$$
$$= \frac{1}{2\pi} \int_{-\infty}^{\infty} \prod_{l=1}^{L} \frac{1}{(1-j\omega 2\sigma_l^2)} e^{\frac{j\omega s_l^2}{(1-j\omega 2\sigma_l^2)}} e^{-j\omega y} d\omega, \quad y \geq 0 \qquad [5.52]$$

The function inside the integral has L different essential singularities (poles of infinite order) located at $j\omega = \frac{1}{2\sigma_l^2}$. In order to determine the coefficient of the pole of -1^{th} order, a full Laurent expansion is needed at each singularity, resulting an L^{th}-time nested infinite summation of the coefficients of Laurent series. To the author's knowledge, no analytic solution has been determined.

SECTION 5.9 Appendix C

This appendix provides a summary of literature search for an analytic form of the pdf $p_R(r)$ of the perceived intensity R. The efforts were met with little success, but the author decided that the findings would merit documentation anyway. The following equations were transcribed from the cited sources largely unchanged, but with minor adaptations for the notation convention used in this chapter.

A solution for a special case of Eq. [5.52] exists (Theorem 4 in p.59 of Ref. (10)) when there are only two distinct variances among the σ_i's, that is,

$$\sigma_i = \begin{cases} \sigma_w, & i = 1,\ldots,D \\ \sigma_v, & i = D+1,\ldots,L \end{cases}. \qquad [5.53]$$

And rewriting Equation [5.25]

$$\begin{aligned} Y &= \sum_{i=1}^{n} Z_i^2 \\ &= \sum_{i=1}^{2L} Z_i^2 \\ &= \sum_{i=1}^{2D} W_i^2 + \sum_{i=1}^{2(L-D)} V_i^2 \end{aligned} \quad , \qquad [5.54]$$

where W_i and V_i are the noncentral Gaussian random variables of variances σ_w^2 and σ_v^2 respectively.

In this special case, the pdf of Y is expressed as:

$$p_Y(y) = \frac{1}{\sigma_w^2} \frac{y^{\frac{(2L-2)}{4}}}{a^{\frac{2L-2}{2}}} \left(\frac{\sigma_w^2}{\sigma_v^2}\right) e^{\frac{-y}{2\sigma_w^2}} e^{\frac{-\left(\frac{a^2}{\sigma_w^2}+\frac{b^2}{\sigma_v^2}\right)}{2}} \times \sum_{\alpha=0}^{\infty}\sum_{\beta=0}^{\infty} \frac{\Gamma(D+\alpha+\beta)}{\alpha!\beta!\Gamma(D+\alpha)} \left(\frac{\sqrt{y}b^2\sigma_w^4}{2a\sigma_v^2}\right)^{\alpha} \times \left[\frac{\sqrt{y}\left(\frac{1}{\sigma_w^2}-\frac{1}{\sigma_v^2}\right)\sigma_w^2}{a}\right]^{\beta} I_{\frac{1}{2}(2L+\alpha+\beta-1)}\left(\frac{\sqrt{y}a}{\sigma_w^2}\right) \quad , [5.55]$$

where

$$a = \sqrt{\sum_{i=1}^{D} (s_i)^2} \qquad [5.56]$$

and

$$b = \sqrt{\sum_{i=D+1}^{L} (s_i)^2} \,. \qquad [5.57]$$

The nested infinite summation of Bessel functions in Eq. [5.55] is not attractive computationally. Unfortunately, if there are more than two distinct variances, the expression will further develop into a high order of nested summation.

A slightly more general approach was taken by Press et al (11). The derivation depends on the fact that the pdf of noncentral chi-square variate $\chi^2_{d,s}$ of d degrees of freedom and s^2 noncentrality parameter can be expressed as a weighted sum of central chi-square variates with the weights equal to the probabilities of a Poisson distribution.

$$p_{\chi^2_{d,s}}\left(\chi^2_{d,s}\right) = \sum_{k=0}^{\infty}\left(\frac{s^{2k}}{2^k k!}e^{s^2/2}\right) p_{\chi^2_{d+2k,0}}\left(\chi^2_{d+2k,0}\right). \qquad [5.58]$$

If there are L distinct variance σ_i's, and $2L = n$, then we can express Eq. [5.54] as:

$$\begin{aligned} Y &= \sum_{i=1}^{n} Z_i^2 = \sum_{i=1}^{2L} Z_i^2 = \sum_{l=1}^{L}\left(Z_l^{real}\right)^2 + \left(Z_l^{imag}\right)^2 \\ &= \sum_{l=1}^{L} \sigma_l^2 \chi^2_{2,s_l} \end{aligned} \,. \qquad [5.59]$$

To match the convention used in Press, we let $\tilde{l} = l - 1$:

$$\begin{aligned} Y &= \sum_{\tilde{l}=0}^{L-1} \sigma_{\tilde{l}}^2 \chi^2_{2,s_{\tilde{l}}} \\ &= \alpha\left[\chi^2_{2,s_{\tilde{l}}} + \sum_{\tilde{l}=1}^{L-1} a_{\tilde{l}} \chi^2_{2,\tilde{l}}\right] \end{aligned} \,, \qquad [5.60]$$

where $\alpha = \sigma_0^2$ and $a_{\tilde{l}} = \dfrac{\sigma_{\tilde{l}}^2}{\sigma_0^2}$ for $\tilde{l} = 1,..,L-1$. We will drop the tilde from l from here onward. Now we are ready to express the pdf of Y.

$$p_Y(y)=\sum_{\gamma=0}^{\infty} q_\gamma p_{\chi^2_{2l+2\gamma,0}}\left(\frac{y}{\alpha}\right), \text{ where } q_\gamma>0,\ \sum_{\gamma=0}^{\infty} q_\gamma=1. \qquad [5.61]$$

The weighting constants, q_γ's are a function of s_l and a_l.

$$q_0=\left(\prod_{l=1}^{L-1} a_l^{-1}\right)\exp\left(-\frac{1}{2}\sum_{l=0}^{L-1} s_l^2\right), \qquad [5.62]$$

and for all $\gamma\neq 0$,

$$q_\gamma=\sum_{\alpha=0}^{\gamma}\left[e^{-s_0^2/2}\left(d_0^2/2\right)^{\gamma-\alpha}/(\gamma-\alpha)!\right]K_\alpha(\gamma), \qquad [5.63]$$

and the $K_\alpha(\gamma)$ satisfy $K_\alpha(\gamma)\le 1$, and

$$\begin{aligned} K_\alpha(1)&=h_\alpha^{(1)},\\ K_\alpha(2)&=\sum_{i_1=0}^{\alpha} h_{\alpha-i_1}^{(2)} h_{i_1}^{(1)},\\ K_\alpha(3)&=\sum_{i_1=0}^{\alpha}\sum_{i_2=0}^{i_1} h_{\alpha-i_1}^{(3)} h_{i_1-i_2}^{(2)} h_{i_2}^{(1)}, \quad etc \end{aligned} \qquad [5.64]$$

The $h_\alpha^{(l)}$ are defined by

$$h_\alpha^{(l)}=\sum_{\beta=0}^{\alpha}\sum_{k=0}^{\beta}\left[e^{-d_l^2/2}\left(d_l^2/2\right)^{\beta-k}/(\beta-k)!\right]c_{\alpha-\beta}^{(l)} g_k^{(l,\beta-k)}, \qquad [5.65]$$

where the $c_\alpha^{(l)}$, and the $g_\beta^{(l,k)}$ are defined by

$$c_\alpha^{(i)}=a_l^{-m_l/2}\left(1-a_l^{-1}\right)^\alpha \Gamma(m_l/2+\alpha)/\Gamma(\alpha+1)\Gamma(m_l/2), \qquad [5.66]$$

$$g_\beta^{(l,k)}=a_l^{-k}\left(1-a_l^{-1}\right)^\beta\binom{\beta+k-1}{\beta}, \qquad \beta\ge 1,\ g_0^{(l,0)}=1. \qquad [5.67]$$

In summary, neither of the two approaches shown in this appendix provides any obvious computational benefits for the generalized noise analysis in this chapter. Paradoxically, speculations can be made that should an analytic solution actually exist, it would invariably assume complicated expressions similar to those of the two approaches. The numeric approach described in the Theory section may still be the best alternative.

Chapter 5 References

1. Gudbjartsson H, Patz S. The Rician distribution of noisy MRI data. Magn Reson Med 1995;34:910-914.
2. Constantinides CD, Atalar E, McVeigh ER. Signal-to-noise measurements in magnitude images from NMR phased arrays. Magn Reson Med 1997;38(5):852-7.
3. McKenzie CA, Ohliger MA, Yeh EN, Price MD, Sodickson DK. Coil-by-coil image reconstruction with SMASH. Magn Reson Med 2001;46(3):619-23.
4. Griswold MA, Jakob PM, Heidemann RM, Nittka M, Jellus V, Wang J, Kiefer B, Haase A. Generalized autocalibrating partially parallel acquisitions (GRAPPA). Magn Reson Med 2002;47(6):1202-10.
5. Yeh EN, McKenzie CA, Ohliger MA, Sodickson DK. Parallel Magnetic Resonance Imaging with Adaptive Radius in k-Space (PARS): Constrained Image Reconstruction using k-Space Locality in Radiofrequency Coil Encoded Data (In Press). Magn Reson Med 2005.
6. Strang G. Linear Algebra and Its Applications: Acadmeic Press; 1980.
7. Pruessmann KP, Weiger M, Scheidegger MB, Boesiger P. SENSE: sensitivity encoding for fast MRI. Magn Reson Med 1999;42(5):952-62.
8. Griswold MA, Jakob PM, Nittka M, Goldfarb JW, Haase A. Partially parallel imaging with localized sensitivities (PILS). Magn Reson Med 2000;44(4):602-9.
9. Rofsky NM, Lee VS, Laub G, Pollack MA, Krinsky GA, Thomasson D, Ambrosino MM, Weinreb JC. Abdominal MR imaging with a volumetric interpolated breath-hold examination. Radiology 1999;212(3):876-84.
10. Miller K. Multidimensional Gaussian Distributions. New York: Wiley; 1964.
11. Press SJ. Linear combinations of Non-Central Chi-Square Variates. Ann Math Statist 1966;37:480-7.

CHAPTER 6. FUNDAMENTAL LIMITS: PARALLEL IMAGE RECONSTRUCTION AS AN ARRAY PROCESSING TECHNOLOGY[14]

This chapter studies the theoretical and numerical correspondence between parallel MRI and wireless communications, both of which belong to the general family of array processing technology. In particular, the work in this chapter addresses the question whether parallel image reconstructions (i.e., the linear inverse problem $\mathbf{s} = \mathbf{E}\boldsymbol{\rho}$) could be improved by adapting methods from the wireless community.

SECTION 6.1 Introduction

A close correspondence has recently been reported between parallel MRI and multiple-input multiple-output (MIMO) wireless communications (1). (Fig. 6.1 provides a schematic illustration of MIMO.) Both fields utilize measured "sensitivity" information in multiple detectors to unfold aliased data. However, in MIMO, maximum likelihood estimation (MLE) has been shown to outperform matrix inversion techniques for signal decoding (2). One might speculate, therefore, that MLE might also yield improved

[14] The work in this chapter has been accepted for presentation as "Yeh EN, Ohliger MA, Cheng MC, Grant AK, Sodickson DK. Can Maximum Likelihood Estimation Outperform Matrix Inversion in Parallel Image Reconstruction? Proc. 13th Annual Meeting ISMRM; 2005; Miami Beach, USA."

performance for parallel MRI, in particular if the reconstructed signal data assume finite bit precision. This study addresses this question by first deriving the theoretical bounds of parallel image reconstruction, then outlining a general theory of MLE and also the special conditions under which MLE and encoding matrix inversion become mathematically equivalent. A practical adaptation of MLE for parallel image reconstruction with finite bit precision is then described. Lastly, the results of numerical simulations comparing MLE and matrix inversion are presented and discussed.

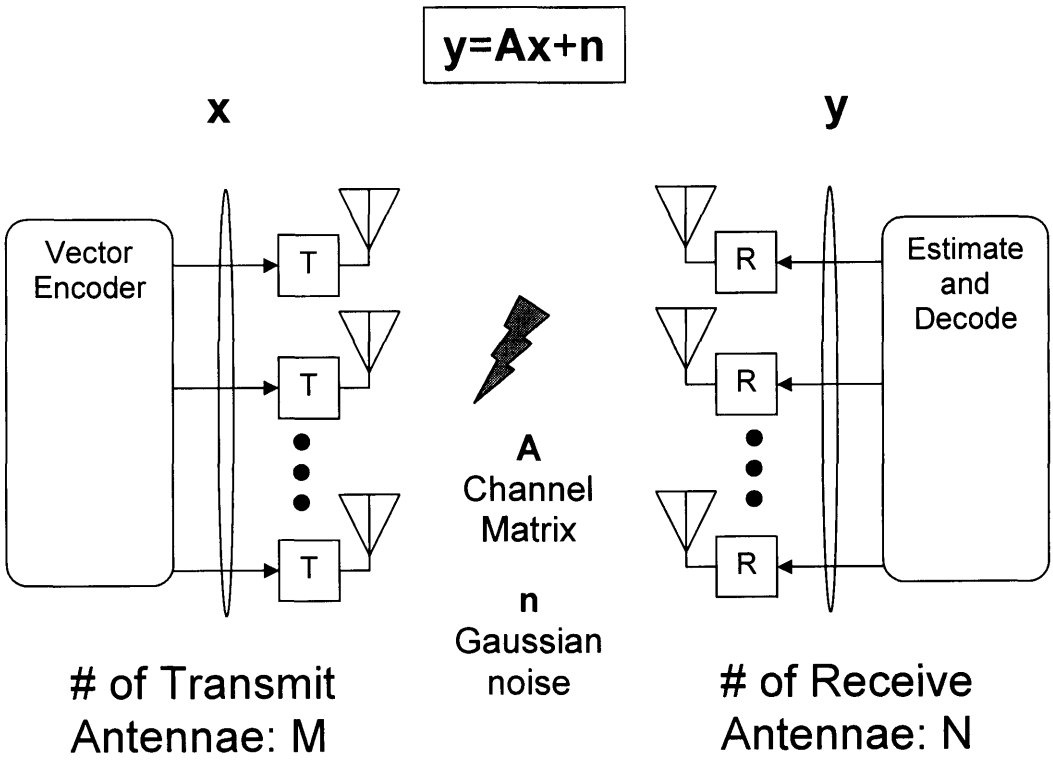

FIGURE 6.1 **Schematic of Multiple-Input Multiple-Out (MIMO) Technology**

Schematic of the multiple-input multiple-output technology in wireless communications. Multiple antennae are transmitting simultaneously in the same channels. The signals traverse different paths, and hence experience different channel conditions, before reaching the multiple receive antennae. The aliased signals can be resolved algebraically using prior knowledge of the channel matrix A (shown here), or using a maximum-likelihood estimation algorithm (not shown here).

SECTION 6.2 Theory

6.2.a The Cramer-Rao Bound for Parallel MRI

The Cramer-Rao bound (CRB) gives the lower bound on the variance of any valid estimator $\hat{x}(y)$ for x. Traditionally, the application of the CRB has been limited to the class of unbiased estimators. However, recent work has expanded it to include the class of biased estimators (3,4). This section provides the derivations of the CRB for two major classes of parallel MRI reconstruction techniques described in Sec. 1.5.c.2: the full matrix inversion approach (e.g., unbiased reconstruction in SENSE (5)) and the *k*-space block-diagonalization approach (e.g., biased reconstruction in PARS, SMASH (6) and GRAPPA(7)). The third, but minor class of parallel MRI reconstruction techniques — the image-domain block-diagonalization, PILS (8) — will be presented in the Discussion section where it is compared to the channel allocation strategy used in wireless communications prior to the development of MIMO.

UNBIASED ESTIMATION

In both parallel MRI and MIMO, a vector of observations, $\mathbf{y}$, can be expressed in terms of a linear system $\mathbf{A}$, an unknown vector of nonrandom parameters $\mathbf{x}$, and a noise vector $\mathbf{n}$,

$$\mathbf{y} = \mathbf{A}\mathbf{x} + \mathbf{n}, \qquad [6.1]$$

where $\mathbf{n} \sim N(0, \mathbf{\Psi})$, denoting zero-mean Gaussian distribution with covariance matrix $\mathbf{\Psi}$. If an estimator $\hat{\mathbf{x}}(\mathbf{y})$ has an expected value equal to the unknown $\mathbf{x}$, i.e.,

$$E\left[\hat{\mathbf{x}}(\mathbf{y})\right] = \mathbf{x}, \qquad [6.2]$$

then $\hat{\mathbf{x}}(\mathbf{y})$ is said to be unbiased. The familiar least-squares (Moore-Penrose) pseudo-inverse solution (Eq. [1.38]) provides an unbiased estimator,

$$\hat{\mathbf{x}}(\mathbf{y}) = \left(\mathbf{A}^H\mathbf{A}\right)^{-1}\mathbf{A}^H\mathbf{y} \qquad [6.3]$$

since

$$
\begin{aligned}
E\left[\hat{\mathbf{x}}(\mathbf{y})\right] &= E\left[\left(\mathbf{A}^H\mathbf{A}\right)^{-1}\mathbf{A}^H\mathbf{y}\right] \\
&= E[\mathbf{x}] + E\left[\left(\mathbf{A}^H\mathbf{A}\right)^{-1}\mathbf{A}^H\mathbf{n}\right]. \\
&= \mathbf{x}
\end{aligned}
\qquad [6.4]
$$

More generally, when a matrix $\mathbf{A}^{-1}$ satisfies the condition $\mathbf{A}^{-1}\mathbf{A} = \mathbf{Id}$ where $\mathbf{Id}$ is an identity matrix, the estimator defined by,

$$
\hat{\mathbf{x}}(\mathbf{y}) = \mathbf{A}^{-1}\mathbf{y} \qquad [6.5]
$$

is unbiased. The CRB for the covariance matrix of any unbiased estimator, $\mathbf{\Lambda}_{unbiased}(\mathbf{x})$, is given by

$$
\mathbf{\Lambda}_{unbiased}(\mathbf{x}) \geq \mathbf{I}_{\mathrm{y}}^{-1}(\mathbf{x}), \qquad [6.6]
$$

where $\mathbf{I}_{\mathrm{y}}(\mathbf{x})$ is the Fisher information matrix,

$$
\begin{aligned}
\mathbf{I}_{\mathrm{y}}(\mathbf{x}) &= E\left[\left[\frac{\partial \ln p_{\mathrm{y}}(\mathbf{y};\mathbf{x})}{\partial x}\right]^H\left[\frac{\partial \ln p_{\mathrm{y}}(\mathbf{y};\mathbf{x})}{\partial x}\right]\right] \\
&= -E\left[\frac{\partial^2 \ln p_{\mathrm{y}}(\mathbf{y};\mathbf{x})}{\partial x^2}\right]
\end{aligned}
\qquad [6.7]
$$

and $p_{\mathrm{y}}(\mathbf{y};\mathbf{x})$ is the probability density of function of $\mathbf{y}$ parameterized by $\mathbf{x}$. As shown in Eq. [3.260] of Ref. (9), the Fisher information matrix for a linear system with Gaussian noise can be expressed as

$$
\mathbf{I}_{\mathrm{y}}(\mathbf{x}) = \mathbf{A}^H\mathbf{\Psi}^{-1}\mathbf{A}, \qquad [6.8]
$$

and the CRB is

$$
\mathbf{\Lambda}_{unbiased} \geq \left(\mathbf{A}^H\mathbf{\Psi}^{-1}\mathbf{A}\right)^{-1}. \qquad [6.9]
$$

Eq. [6.9] interestingly coincides with the noise covariance matrix derived for the minimum-variance unbiased (MVU) reconstruction (Eqs. [1.44]-[1.46]), such that,

$$
\begin{aligned}
\hat{\mathbf{x}}_{\mathrm{MVU}}(\mathbf{y}) &= \mathbf{A}_{\mathrm{MVU}}^{-1}\mathbf{y} \\
&= \left(\mathbf{A}^H\mathbf{\Psi}^{-1}\mathbf{A}\right)^{-1}\mathbf{A}^H\mathbf{\Psi}^{-1}\mathbf{y}
\end{aligned}
\qquad [6.10]
$$

and

$$\mathbf{\Lambda}_{\mathrm{MVU}} = \left(\mathbf{A}^{H}\mathbf{\Psi}^{-1}\mathbf{A}\right)^{-1} = CRB\,. \qquad [6.11]$$

In other words, for unbiased parallel image reconstructions, the full matrix approach with Cholesky decomposition has already achieved the theoretical lower bound imposed by the CRB, and is therefore an optimal method for unbiased reconstructions.

BIASED ESTIMATION

In parallel imaging, an inexact image reconstruction, where $\mathbf{A}_{biased}^{-1}\mathbf{A} \neq \mathbf{Id}$, is often preferred in order to achieve computational efficiency and/or better conditioning in the matrix inversion. PARS and other *k*-space block-diagonalization methods belong to this category. To characterize the inexactness of the reconstruction, a bias gradient matrix $\mathbf{B}$ is defined as

$$\mathbf{B} = \mathbf{A}_{biased}^{-1}\mathbf{A} - \mathbf{Id}\,. \qquad [6.12]$$

The biased estimator, $\hat{\mathbf{x}}_{biased}(\mathbf{y}) = \mathbf{A}_{biased}^{-1}\mathbf{y}$, then has a bias vector that is expressed in terms of $\mathbf{B}$ and $\mathbf{x}$,

$$\begin{aligned}\mathbf{b}(\mathbf{y}) &= E\left[\hat{\mathbf{x}}_{biased}(\mathbf{y})\right] - \mathbf{x} \\ &= E\left[\mathbf{A}_{biased}^{-1}\mathbf{y}\right] - \mathbf{x} \\ &= E\left[\mathbf{A}_{biased}^{-1}\mathbf{A}\mathbf{x}\right] + E\left[\mathbf{A}_{biased}^{-1}\mathbf{n}\right] - \mathbf{x} \\ &= \mathbf{A}_{biased}^{-1}\mathbf{A}\mathbf{x} - \mathbf{x} = \mathbf{B}\mathbf{x}\end{aligned}\,. \qquad [6.13]$$

This bias is not removable because it is a function of the unknown parameter $\mathbf{x}$. The class of matrices $\mathbf{A}_{biased}^{-1}$ for a given $\mathbf{B}$ can be expressed as follows,

$$\mathbf{A}_{biased}^{-1} = (\mathbf{Id} + \mathbf{B})\mathbf{A}_{unbiased}^{-1} \qquad [6.14]$$

where $\mathbf{A}_{unbiased}^{-1}$ is any matrix which satisfies the condition $\mathbf{A}_{unbiased}^{-1}\mathbf{A} = \mathbf{Id}$.

The unbiased CRB stated in Eq. [6.6] can be modified to compute the biased CRB (BCRB) (Eq. [3], in Ref. (4)),

$$\mathbf{\Lambda}_{biased}(\mathbf{x}) \geq (\mathbf{Id} + \mathbf{B})\mathbf{I}_{\mathbf{y}}^{-1}(\mathbf{Id} + \mathbf{B})^{H} \qquad [6.15]$$

A biased estimator $\hat{\mathbf{x}}_{biased}(\mathbf{y}) = \mathbf{A}_{biased}^{-1}\mathbf{y}$ has "biased" minimum variance (MVB) if and only if $\mathbf{A}_{biased}^{-1}$ can be expressed in terms of:

$$\mathbf{A}_{biased}^{-1} = \mathbf{A}_{\mathrm{MVB}}^{-1} = (\mathbf{Id} + \mathbf{B})\mathbf{A}_{\mathrm{MVU}}^{-1}, \qquad [6.16]$$

and the covariance matrix achieves the BCRB,

$$\begin{aligned} \mathbf{\Lambda}_{\mathrm{MVB}} &= (\mathbf{I}+\mathbf{B})\mathbf{A}_{\mathrm{MVU}}^{-1}\mathbf{\Psi}\left((\mathbf{I}+\mathbf{B})\mathbf{A}_{\mathrm{MVU}}^{-1}\right)^{H} \\ &= (\mathbf{I}+\mathbf{B})\mathbf{A}_{\mathrm{MVU}}^{-1}\mathbf{\Psi}\left(\mathbf{A}_{\mathrm{MVU}}^{-1}\right)^{H}(\mathbf{I}+\mathbf{B})^{H} \\ &= (\mathbf{I}+\mathbf{B})\mathbf{I}_{\mathbf{y}}^{-1}(\mathbf{I}+\mathbf{B})^{H} \\ &= BCRB \end{aligned} \qquad [6.17]$$

In fact, when given any matrix $\mathbf{A}_{biased}^{-1}$, the corresponding $\mathbf{A}_{\mathrm{MVB}}^{-1}$ which yields the same bias gradient $\mathbf{B}$ can be determined by a matrix multiplication by $\mathbf{A}\mathbf{A}_{\mathrm{MVU}}^{-1}$,

$$\begin{aligned} \mathbf{A}_{\mathrm{MVB}}^{-1} &= \mathbf{A}_{biased}^{-1}\mathbf{A}\mathbf{A}_{\mathrm{MVU}}^{-1} \\ &= (\mathbf{Id}+\mathbf{B})\mathbf{A}_{\mathrm{MVU}}^{-1} \end{aligned} \qquad [6.18]$$

The ability to determine the minimum-variance $\mathbf{A}_{\mathrm{MVB}}^{-1}$ for any $\mathbf{A}_{biased}^{-1}$ (or any $\mathbf{B}$) is valuable for inexact parallel imaging techniques such as SMASH, GRAPPA and PARS as discussed in Chapter 3. For example, a PARS reconstruction matrix $\mathbf{A}_{PARS}^{-1}$ (expressed in terms of $\mathbf{F\Omega}$ in Eq. [3.14]) can be optimized in regard to noise amplification using $\mathbf{A}_{\mathrm{MV}-PARS}^{-1} = \mathbf{A}_{PARS}^{-1}\mathbf{A}\mathbf{A}_{\mathrm{MVU}}^{-1}$ while maintaining the same level of image artifact power. The total power plotted in Figs. 3.3 and 3.4. will likely decrease, apart from the uncertain effects of magnitude combinations. However, it should be noted that this noise optimization can only be performed when $\mathbf{A}\mathbf{A}_{\mathrm{MVU}}^{-1}$ can be computed efficiently and accurately. In the general case (e.g., non-Cartesian trajectories) where PARS is needed in order to invert large and unstable encoding matrices, it will not be feasible to compute $\mathbf{A}\mathbf{A}_{\mathrm{MVU}}^{-1}$. $\mathbf{A}_{PARS}^{-1}$, even though not necessarily optimized for noise consideration, is still an attractive alternative. And once again, when PARS-reconstructed coil images are combined using sum-of-squares, the BCRB no longer applies to the composite image.

Recent work has developed further applications of the BCRB by deriving an "average-case" BCRB and a "worst-case" BCRB. (3,4). These metrics are particularly

relevant to PARS and other inexact parallel MRI technique since the metrics provide flexible operator-defined parameters to constrain the overall artifacts in image reconstruction. In both cases, the class of biased estimators is no longer defined by a given $\mathbf{B}$. Instead, any biased estimator whose $\mathbf{B}$ has a norm bounded by a constant,

$$\mathrm{Tr}\left(\mathbf{B}\mathbf{B}^{H}\right) \leq \beta. \qquad [6.19]$$

is included. Here, $\mathrm{Tr}(\cdot)$ denotes the trace of the matrix (i.e. sum of the diagonal elements). The "average-case" BCRB gives the lower bound in terms of total variance, λ_{total},

$$\lambda_{total} = \mathrm{Tr}\left((\mathbf{I}+\mathbf{B})\mathbf{I}_{\mathbf{y}}^{-1}(\mathbf{I}+\mathbf{B})^{H}\right), \qquad [6.20]$$

whereas the worst-case BCRB gives the lower bound in terms of the maximum variance, $\lambda_{\max}$,

$$\lambda_{\max} = \max\left(diag\left((\mathbf{I}+\mathbf{B})\mathbf{I}_{\mathbf{y}}^{-1}(\mathbf{I}+\mathbf{B})^{H}\right)\right). \qquad [6.21]$$

While this new approach may provide additional tools to fine-tune the PARS technique, future studies are required to explore potential benefits of the case-based BCRB for parallel MRI in general.

6.2.b Can Maximum Likelihood Estimation Outperform Matrix Inversion in Parallel Image Reconstruction?

To simplify the comparison with MLE, only unbiased image reconstructions were considered for the remaining sections. The previous section has shown that parallel image reconstructions, when solutions of the inverse problem $\mathbf{s} = \mathbf{E}\boldsymbol{\rho}$ are obtained by linear algebraic methods, achieve the CRB. They are so-called efficient estimators. As shown in Eqs. [3.198]-[3.201] in Ref. (9), if an efficient estimator exists, it is a maximum likelihood estimator. When the noise has a non-Gaussian distribution (i.e., Chapter 5), an efficient estimator may not exist. MLE can still be derived, but it need not have any special properties.

The puzzle remains that in MIMO where $\mathbf{x}$ takes discrete values from a finite alphabet, MLE outperforms that of the linear algebraic least-squares solution, which is sometimes referred to in this context as "zero-forcing" (1). This suggests that the least-squares solution for MIMO does not reach the CRB. The simulations in the Method section investigate whether the MLE approach can also outperform the matrix least-squares approach in parallel MRI when the estimated $\hat{\mathbf{x}}$ assumes finite bit precision to represent the underlying magnetization density.

SECTION 6.3 Method

6.3.a Maximum Likelihood Estimation

In MLE, a solution vector $\hat{\mathbf{x}}$ (out of an exhaustive set of candidate $\mathbf{x}$'s) is obtained which maximizes the probability of the observation vector $\mathbf{y}$ parameterized by $\mathbf{x}$,

$$\hat{\mathbf{x}} = \underset{\mathbf{x} \in \text{ all possible x's}}{\arg\max} \; p_{(\mathbf{y};\mathbf{x})}(\mathbf{y};\mathbf{x}) \quad . \qquad [6.22]$$

The discreteness of $\mathbf{x}$ in MIMO allows MLE detection using multiple-hypothesis testing, (M-ary hypothesis testing, Sec. 2.8, Ref. (9)). This detection approach is inherently non-linear, and subsequently outperforms that of the linear inversion.

6.3.b Convolutional Codes and Viterbi decoding algorithm

The Viterbi algorithm (10), a computationally efficient MLE decoder for convolutional codes in wireless system, was adapted to perform MLE for parallel imaging. A large degree of correspondence can be drawn from the two technologies. First, Cartesian sampled MR signal data, instead of the traditional integral form, can be equivalently expressed as a convolution of the Fourier transformations of the underlying spin density and the coil sensitivities,

$$\begin{aligned} s_l(\mathbf{k}) &= \int \rho(\mathbf{r}) C_l(\mathbf{r}) e^{i\mathbf{k}\cdot\mathbf{r}} d\mathbf{r} \\ &= FT\left(\rho(\mathbf{r}) C_l(\mathbf{r})\right) \\ &= FT\left(\rho(\mathbf{r})\right) \otimes FT\left(C_l(\mathbf{r})\right) \end{aligned} \qquad [6.23]$$

Each coil sensitivity function can be treated as a convolutional polynomial used in forward error correction (FEC) channel coding, and the MR signal stream $s_l(\mathbf{k})$ is equivalent to a codeword. The subsequent undersampling (downsampling) procedure for parallel MRI can be represented as a puncturing procedure where selected coded symbols are omitted.

In our implementation of Viterbi decoding, low-resolution approximations of coil sensitivities were used in order to reduce the complexity of the Viterbi algorithm, which scales exponentially with the length of the convolutional polynomials. By initially quantizing $\hat{\mathbf{x}}$ to a limited bit precision, a coarse MLE solution was obtained after the first iteration. Successive iterations added bit precision to the MLE solution by refining the quantization levels. Each iteration added ½ bit of resolution to the MLE solution. A total of 24 iterations were required to obtain the 12-bit precision that is typical in MR images.

Signal data were simulated using a coil array of 8 rectangular elements (400x60mm each), covering a total area of 400x400mm (also the field of view of the image). Various levels of Gaussian noise were added. Parallel image reconstructions were performed from datasets with various acceleration factors, using both the MLE algorithm described above and the standard SENSE least-squares pseudo-inverse reconstruction (5). Total error power was plotted as a function of bit precision.

SECTION 6.4 Results

Fig 6.2 illustrates the simulation results, which are consistent with the theoretical expectations that, in the limit of infinite bit resolution, the MLE and least-squares matrix inverse approaches converge. Two-fold accelerated MR signal data were used in the image reconstructions. The least-squares matrix inverse approach, which has been shown to be an efficient estimator, defines the lower bound toward which the solution from the finite-precision Viterbi decoding algorithm asymptotically converges.

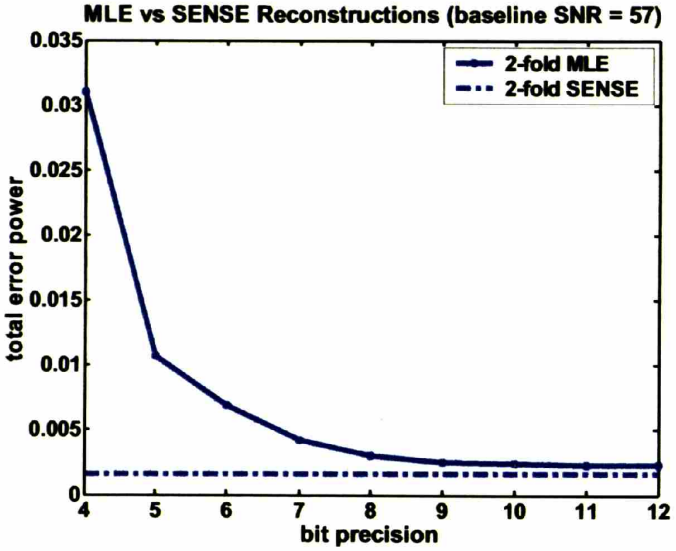

FIGURE 6.2 Convergence of Finite-Precision MLE and Full-Matrix Inversion

Numerical simulations confirm theoretical expectations that, in the limit of infinite bit resolution, the MLE and least-squares matrix inverse approaches converge. Two-fold accelerated MR signal data were used in the image reconstructions. The least-squares matrix inverse approach, which has been shown to be an efficient estimator, defines the asymptotic lower bound towards which the solution from the finite-precision Viterbi decoding algorithm converges.

Fig. 6.3 illustrates the error plots of two-fold (a) and three-fold (b) reconstructions at various noise levels. The total error power monotonically decreases as a function of the bit precision, but at some bit level, it becomes asymptotic. This strongly suggests that the baseline SNR ultimately dictates the realizable bit precision of an image, and added precision to the image reconstruction solution has diminishing yields after the 10^{th} bit.

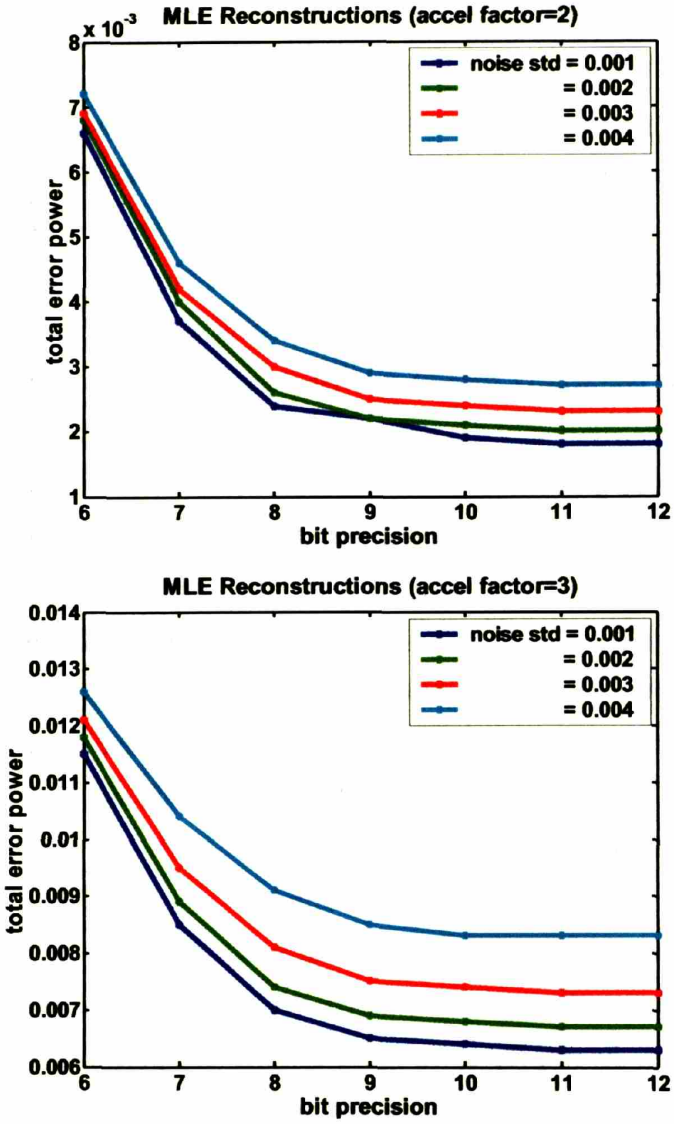

FIGURE 6.3 Error Plots of Finite-Precision MLE

Error plots of MLE reconstructions of two-fold (a) and three-fold (b) accelerated datasets at various noise levels. The total error power monotonically decreases as a function of the bit precision, but at some bit level, it becomes asymptotic. This strongly suggests that the baseline SNR ultimately dictates the realizable bit precision of an image, and added precision to the image reconstruction solution has diminishing yields after the 10^{th} bit.

SECTION 6.5 Discussion

CONVERGENCE TO OTHER ARRAY PROCESSING TECHNOLOGIES

This work provides a demonstration of the correspondence between two array processing technologies. Even though the fields of parallel MRI and MIMO wireless communications have been developed independently, they are on a converging path to the same fundamental stochastic limits, such as those imposed by the CRB. A minor note should be made that the image-domain block-diagonalization approach, e.g., PILS, bears much resemblance of the pre-MIMO state of cellular communications. Both techniques, instead actively resolving the aliasing of the signal using measured sensitivity, use a passive method of avoiding aliasing by guaranteeing adequate spatial separation. As the sensitivities drop off naturally, channel allocation algorithms in cellular networks minimize channel interference by assigning different channels to adjacent cells. The signal from the next-nearest neighbor cell is assumed to drop off sufficiently so that the attenuated signal appears to be noise-like. The advent of MIMO has increased the channel capability by many-fold, where bandwidth is the limiting commodity. In MRI where the imaging speed is critical, the expanded "bandwidth" made available by parallel MRI is harnessed to achieve markedly accelerated data acquisition instead.

Additional correspondence can be made with other array processing technologies, such as those used in radio astronomy where the notation of k-space and the regridding algorithm were first developed, or in multi-detector computerized tomography (MDCT) where rows of scintillation detectors are added to accelerate the imaging speed. As the field of parallel MRI continues to mature, new breakthroughs may come from cross-fertilization with other already matured array processing technologies.

GENERALIZATION FOR NON-GAUSSIAN NOISE

The least-squares solution is equivalent to MLE only when the noise has Gaussian distribution. In the event that the noise is no longer Gaussian, the least-squares solution is no longer optimal. The Viterbi decoding algorithm, in this case, provides an attractive alternative since it can be adapted to a different noise metric to provide a non-linear solution.

For current applications, the Viterbi decoding algorithm provides an illustrative linkage between wireless communication and parallel MRI which has no immediate computational advantage.

SECTION 6.6 Conclusions

This work has established the CRB for both unbiased and biased parallel image reconstruction techniques. It has also tested the potential benefit of MLE for parallel image reconstructions of finite bit precision. Preliminary results suggest that assuming a solution of moderate but finite bit precision gives *no* apparent advantage over the linear least-squares approach. One might imagine only very specialized circumstances with limited precision requirements for which the MLE algorithm might provide a specific SNR advantage. That said, the stochastic approach in MLE does offer new generalities in accommodating different noise behaviors (e.g. non-Gaussian), *a priori* information, and means to non-linear solutions for future developments of parallel imaging.

Chapter 6 References

1. Bolcskei H. Principles of MIMO-OFDM Wireless Systems. Swiss Federal Institute of Technology (ETH).
2. Bolcskei H. The Communication Handbook. 2nd ed: CRC Press. p 90.1-14.
3. Hero A. Exploring Estimator Bias-Variance Tradeoffs Using the Uniform CR Bound. IEEE Trans Signal Proc 1996;44(8):2026-2040.
4. Eldar Y. Minimum Variance in Biased Estimation: Bounds and Asymptotically Optimal Estimators. IEEE Trans Signal Proc 2004;52(7):1915-1929.
5. Pruessmann KP, Weiger M, Scheidegger MB, Boesiger P. SENSE: sensitivity encoding for fast MRI. Magn Reson Med 1999;42(5):952-62.
6. Sodickson DK, Manning WJ. Simultaneous acquisition of spatial harmonics (SMASH): fast imaging with radiofrequency coil arrays. Magn Reson Med 1997;38(4):591-603.
7. Griswold MA, Jakob PM, Heidemann RM, Nittka M, Jellus V, Wang J, Kiefer B, Haase A. Generalized autocalibrating partially parallel acquisitions (GRAPPA). Magn Reson Med 2002;47(6):1202-10.
8. Griswold MA, Jakob PM, Nittka M, Goldfarb JW, Haase A. Partially parallel imaging with localized sensitivities (PILS). Magn Reson Med 2000;44(4):602-9.
9. Willsky A. Stochastic Processes, Detection and Estimation: MIT CourseNotes; 1998.
10. Proakis J. Digital Communications. 3rd ed: McGraw-Hill; 1995.

CHAPTER 7. ADAPTATION OF A CARDIAC IMAGING TECHNIQUE FOR PARALLEL MRI[15]

A preliminary case study using a cardiac imaging technique is presented to demonstrate how existing clinical scanning protocols can be adapted for parallel MRI. Parallel image reconstruction techniques developed in this thesis were used, and additional imaging parameters not explicitly studied in the previous chapters were considered. As the last subject presented in the dissertation, this chapter offers a forward-looking perspective on how clinical MRI protocols are being reengineered to take full advantage of parallel MRI.

SECTION 7.1 Introduction

In coronary MR angiography (MRA), clinical diagnosis of pathology in the coronary vasculature requires image sets of particularly high spatial resolution. Because of the prolonged acquisitions, these datasets are highly susceptible to cardiac and respiratory motion artifacts. Prior to the invention of parallel MRI, methods have been devised to overcome these constraints. To minimize cardiac motion artifacts, coronary MRA strategies typically restrict data acquisitions to a short temporal window (e.g., 200ms or shorter) around

[15] The work described in the chapter has been presented as "Yeh EN, Botnar RM, Leiner T, McKenzie CA, Sodickson DK. *Adaptation of Coronary Imaging Pulse Sequences for Self-Calibrated Non-Cartesian Parallel Imaging.* Proceedings of the 12th ISMRM Scientific Meeting, Kyoto, Japan, 2004."

end-diastole when the heart is relatively stationary (1). MRA data acquisitions, which generally require much longer than the duration of a single acquisition window, are then segmented over multiple cardiac cycles. Additionally, the length of the acquisition window and the electrocardiogram (ECG) trigger delay are subject-specific, but even after careful calibration, they are susceptible to normal or pathological heart beat variability. Arrhythmia rejection techniques have been proposed to further safeguard the reliability of the acquired data (2).

To minimize respiratory motion artifacts, two different approaches have been developed. In the breath-hold approach, the patient is asked to hold his/her breath during data acquisition, of which by design must be completed within a single breath-hold (3). The quality of the MR images greatly depends on the patient's ability to hold his/her breath during the exam. Alternatively, in the free-breathing approach, the patient can breathe normally, but a diaphragmatic navigator is used to gate and compensate for the respiratory motion (4). A typical free-breathing coronary protocol, however, takes tens of minutes.

The advent of parallel MRI warrants a re-examination of these pulse sequence designs. In addition to providing accelerated imaging speeds, parallel imaging enables a new degree of freedom in designing coronary protocols where not only speed but also the timing of data acquisition is crucial. Furthermore, parallel imaging now has the capability to perform self-calibrated reconstruction on MR data acquired with non-Cartesian trajectories, (e.g., Ref. (5-7) and also Chapters 2 and 3), making many existing coronary MRA sequences readily adaptable to parallel imaging. Without the need of acquiring sensitivity calibration scans or modifying sampling trajectories, images reconstructed from accelerated datasets can be directly and fairly compared to the non-parallel counterparts.

In this chapter, 3-D non-Cartesian MRA sequences (diaphragmatic navigator gated and corrected; ECG triggered; free-breathing) were tested with various lengths of data acquisition windows, acceleration factors and RF excitation pulses. Parallel image reconstructions were performed, and images were evaluated qualitatively to explore an improved design of cardiac parallel imaging protocols.

SECTION 7.2 Methods

DATA ACQUISITION

All scans were performed on a 1.5T Gyroscan ACS-NT whole body MR system (Philips Medical Systems, Best, The Netherlands). MR signal data of coronary arteries of healthy volunteers were acquired with a commercial 5-element array. Two ECG-triggered, navigator-gated/corrected non-Cartesian MRA sequences were used as references: a 3-D spoiled gradient echo (SPGR) spiral sequence (42-interleaf spiral, 2 interleaves per RR interval, flip angles 45°-60°, sampling window 70ms) (8) and a 3-D steady-state free-precession (SSFP) radial sequence (368 projections, balanced TFE, TR 5.6ms, flip angle 110°, sampling window 200ms) (2). Both sequences used conventional phase encoding in the slice direction (12 slices, 30-mm slab thickness) (9). Prior to data acquisition in each RR interval, T2 preparation pulses (for myocardial signal suppression) and fat-saturation pulses (for pericardial fat signal suppression) were applied. The two data acquisition sequences were subsequently modified with various undersampling factors and acquisition window durations, resulting in different overall acceleration factors. Tables 7.1 and 7.2 summarize and compare the important imaging parameters.

# of Spiral Interleaves	# of Interleaves per RR Interval	Acquisition Window	Undersampling Factor	Overall Acceleration
a) 42 (ref)	2 (45°/60°)	70 ms	1.0	1
b) 21	1 (90°)	35 ms	2.0	1
c) 14	1 (90°)	35 ms	3.0	1.5

TABLE 7.1 Imaging Parameters for *in vivo* Spiral Acquisitions.

The number of spiral interleafs per R-R interval decreases from 3 (a) to 1 (b) and (c), making it possible to use a full 90° excitation to capture all the magnetization energy in the sole spiral interleaf. The single-interleaf per RR acquisition has the benefits that it results in a shorter acquisition window (yielding greater tolerance for heart rate variability), and that it eliminates artifacts due to partial T1 recovery in between the excitations of the first and second RF pulses.

# of Radial Projections	# of Project/ RR Intervals	Acquisition Window	Under-sampling Factor	Overall Acceleration
a) 368 (ref)	25	200ms	1.0	1
b) 250	17	140ms	1.4	1
c) 123	12	100ms	3.0	1.5

TABLE 7.2 **Imaging Parameters for *in vivo* Radial Acquisitions.**

The number of radial projections per R-R interval decreases from 368 (a) to 250 (b) and to 123 (c). Since a steady-state free-precession sequence was used, the transverse magnetization vector was supposed to be identical for each data acquisition. However, because of the much longer acquisition windows (as compared to spiral sequences), image artifacts due to the diminishing effectiveness of T2 preparation and fat-saturation were potentially more prominent. By shortening the acquisition windows using parallel MRI, both image quality and tolerance to heart rate variability would increase without the penalty of increased imaging time.

IMAGE RECONSTRUCTION

For undersampled datasets, images were reconstructed using a self-calibrating version of the PARS technique described in Chapter 3. Low-resolution *in-vivo* coil sensitivities were extracted from the sufficiently sampled center of *k*-space. PARS parallel image reconstruction was then performed using a *k*-space radius of 2. Reference datasets were reconstructed with a standard gridding algorithm with a Kaiser-Bessel kernel of width = 3 and $\beta = 13.9086$ (Table 2 of Ref. (10)).

SECTION 7.3 Results

Image reconstructions corresponding to the entries of Tables 7.1 and 7.2 are shown in Figs 7.1 and 7.2.

7.3.a Spiral Image Reconstructions

Fig. 7.1**a** and **b** display comparable baseline SNR despite the fact that **b** was reconstructed from a two-fold undersampled dataset. This is consistent with our expectation

because unlike **a** which splits the magnetization energy between the two spiral interleaves in the same RR interval, **b** can take advantage of a full 90° RF excitation. Besides the g-factor penalty (Eq. [1.49]), there is no theoretical SNR loss between the two. **b** also carries an advantage that every acquisition receives the same magnetization energy, whereas **a** needs to address the effect of T_1 recovery between the two RF excitations (e.g., the 45° and 60° pulses). **c** shows a visible SNR loss compared to **b** in exchange for an accelerated acquisition.

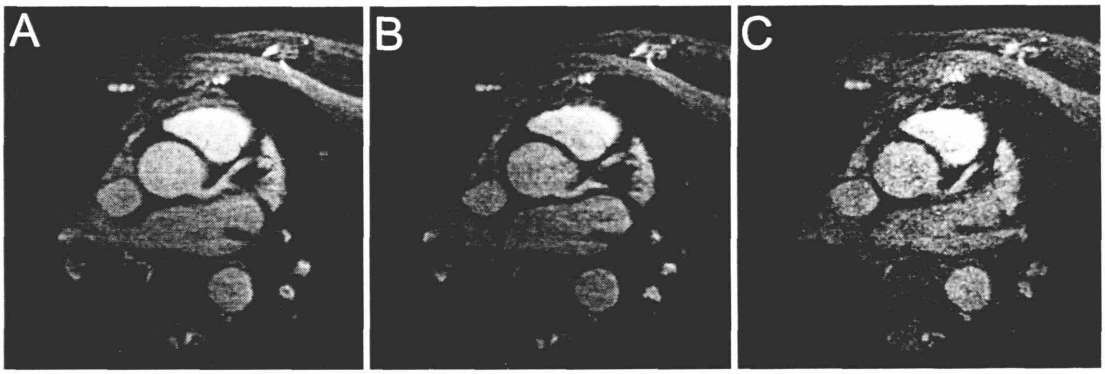

FIGURE 7.1 Spiral Coronary MRA Parallel Image Reconstructions

Spiral coronary MRA images acquired using 42-interleaves (a), 21-interleaves (b), and 14 interleaves (c). Data acquisition for (a) were performed using two-interleaves per RR interval with flip angles 45° and 90°, and (b) and (c) using one-interleaf with a single flip angle 90°. The rest of the corresponding imaging parameters are shown in Table 7.2. (a) and (b) display comparable baseline SNR despite the fact that (b) was reconstructed from a two-fold undersampled dataset. This is consistent with our expectation because unlike a which splits the magnetization energy between the two spiral interleaves in the same RR interval, (b) can take advantage of a full 90° RF excitation. Besides the g-factor penalty, there is no theoretical SNR loss between the two. (b) also carries an advantage that every acquisition receives the same magnetization energy, whereas a needs to address the effect of T_1 recovery between the two RF excitations (e.g., the 45° and 60° pulses). (c) shows an noticeable SNR loss compared to b in exchange for a slightly accelerated acquisition.

7.3.b Radial Image Reconstructions

Fig. 7.2, **a** and **b** display apparently similar baseline SNR, even though there *is* an expected loss of SNR from **a** to **b** due to undersampling, in addition to the associated g-factor. **c** shows a more appreciable SNR loss compared to **a** and **b** but has the shortest acquisition window, advantageous in overcoming beat-to-beat heart rate variations.

Additionally, image artifacts are introduced due to the diminishing effectiveness of T2-preparation and fat-saturation pulses in projections acquired late in the acquisition window. These image artifacts directly influence the perceived image quality. In general, the longer the acquisition window, the larger the amount of undesirable variation there is between the first and last projections collected, and the lower the image quality.

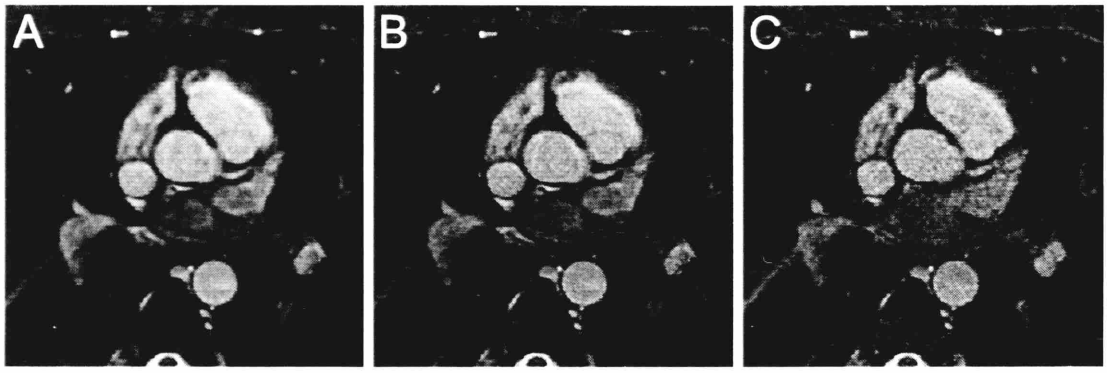

FIGURE 7.2 Radial Coronary MRA Parallel Image Reconstructions

Radial coronary MRA images acquired using 368 projections (a), 250 projections (b), and 123 projections (c). The rest of the corresponding imaging parameters are shown in Table 7.2. (a) and (b) display apparently similar baseline SNR, even though there is an expected SNR loss in additional to the associated g-factor. (c) shows a visible SNR loss compared to (a) and (b) but has the shortest acquisition window, advantageous in overcoming beat-to-beat heart rate variations. The diminishing effectiveness of T2-preparation and fat-saturation pulses (especially in projections acquired late in the RR interval) also influences the perceived image quality. In general, the longer the acquisition window, the larger the amount of undesirable variation there is between the first and last projections collected, the lower the image quality.

SECTION 7.4 Discussion

SHORTER ACQUISITION WINDOW

The shorter acquisition windows used in table entries 7.1a-b and 7.2a-b provide greater tolerance for beat-to-beat variation, which is especially critical for patients with existing cardiovascular pathology. In this study, the datasets were collected from healthy volunteers with no known history of arrhythmia. Fig. 7.1a and 7.2a are arguably the best case scenarios since there is no arrhythmia. It is reasonable to speculate that in future clinical

studies conducted with arrhythmic patients, the image quality for the approaches represented in Fig. 7.1a and 7.2a are expected to decrease.

RF Excitation Angle and T1 Recovery

The nature of the SPGR pulse sequence used in the spiral imaging experiments limits the total magnetization energy available in each RR interval. The employment of different RF excitation angles in the spiral acquisition was intended to optimally and evenly distribute the magnetization energy among each intra-interval spiral interleaf. (Here, the flip angles were *not* used as a means of spatial encoding, whose potential to create a full complement of generalized encoding functions has been discussed in Chapter 1.)

Ideally, if T1 recovery is negligible between the intra-interval excitations, the successive flip angles, α_m, are expressed as follows in order to evenly split the total magnetization,

$$\alpha_m = \sin^{-1}\left(\frac{1}{\sqrt{M-m+1}}\right), \qquad m = 1,\ldots,M, \qquad [7.1]$$

where M is the total number of intra-interval interleafs. In a two-interleafs/RR scheme, for example, the ideal flip angles should be 45° and 90°. However, in practice, T1 recovery is not negligible between RF excitations. As a result, the second RF pulses excite a larger transverse magnetization, creating image artifacts as a result of the modulation of signal amplitude on every other spiral interleaf. Rather, an empirically determined flip angle combination (45°, 60°) has been used in this example for routine clinical exams. Even though this combination reduces the modulation and improves image quality, it is clear that this too is not an optimal combination because of the residual magnetization left in the z-axis after the last pulse. An additional optimization is required.

Parallel MRI, on the other hand, offers a straightforward alternative. With the ability to reconstruct a full image from a reduced number of spiral interleafs, a strategy of a single interleaf per RR with a 90° excitation can be implemented to ensure optimal use of magnetization energy and elimination of modulation. The noticeable loss of SNR for 3-fold

undersampled spiral in Fig 1.c is mainly a result of an unfavorable g-factor particular to the 5-element array. As MR hardware advances continue to increase the number of coil elements, the g-factors of relatively low accelerations are expected to converge to the theoretical lower bound of 1 (11). In the foreseeable future, the imaging parameters in Table 7.1c and Figure 7.1c will serve as an illustrative example in accelerating overall imaging speed while simultaneously improving image quality.

Steady State Sequence and Diminishing Effectiveness of Preparation Pulses

The radial experiments used an SSFP sequence to explore another potential benefit of parallel imaging. In a steady-state sequence, the magnitude of the magnetization vector is presumably kept in steady-state by periodic RF excitations. While the variation in the signal amplitude has been reduced, there is a noted diminishing effectiveness of T2 preparation and fat-saturation pulses due to the typically longer acquisition time. The gradual recovery of the myocardial and fat signals would disturb the equilibrium, possibly broadening the point-spread function and resulting in a blurring of the image. Methods that insert additional T2 preparation and fat-saturation pulses in the middle of the steady-state sequence have been proposed (12). These methodologies generally require careful manipulations of the steady-state magnetization to prevent undesirable perturbation. Moreover, the extra preparation pulses prolong the overall acquisition time.

Parallel imaging, by shortening the acquisition time, preserves (or even improves) the effectiveness of the preparation pulses. Fig. 7.2b displays a slightly sharper image than Fig. 7.2a, but the difference is very subtle. Cardiac images, in general, may not be able to fully demonstrate the difference of the point-spread functions because the cardiac cycles have limited the length of the continuous acquisition window. In applications such as abdominal imaging where a steady-state sequence is used to collect the entire dataset continuously without interruption, the diminishing effectiveness of the preparation pulses will be more pronounced. Lastly, the inherent robustness of radial imaging, as described in the Discussion section of Chapter 2, makes the qualitative image comparisons even more difficult.

SECTION 7.5 Conclusions

This work has demonstrated the feasibility and benefits of adapting coronary MRA sequences to parallel imaging. Imaging parameters such as acquisition windows, flip angles, and preparation pulses have been redesigned in order to take advantage of the capabilities of parallel MRI. A study using parallel imaging to optimize SNR has recently been reported (13), affirming a growing interest in the MR community to explore a broader use of parallel MRI beyond mere image acceleration. As parallel imaging moves forward to many-element coils with better spatial encoding abilities (e.g., (14)), future clinical protocol designs will have to fully integrate parallel MRI in order to optimally harness these various new capabilities.

Chapter 7 References

1. Glover GH, Pelc NJ. A rapid-gated cine MRI technique. Magn Reson Annual 1988:299.
2. Leiner T, van Yperen G, Eggers H, Yeh EN, Kissinger KV, Katsimaglis G. A Novel Real-Time R-Wave Gating Algorithm for Detection of Heart Rate Variability: Impact on Free-Breathing, Navigator Gated Coronary Artery Imaging. In: Proc. 12th Annual Meeting ISMRM, Toronto, Canada, 2003.
3. Bloomgarden DC, Fayad ZA, Ferrari VA, Chin B, Sutton MG, Axel L. Global cardiac function using fast breath-hold MRI: validation of new acquisition and analysis techniques. Magn Reson Med 1997;37(5):683-92.
4. Ehman RL, Felmlee JP. Adaptive technique for high-definition MR imaging of moving structures. Radiology 1989;173(1):255-63.
5. Pruessmann KP, Weiger M, Bornert P, Boesiger P. Advances in sensitivity encoding with arbitrary k-space trajectories. Magn Reson Med 2001;46:638-651.
6. Yeh EN, Stuber M, McKenzie CA, Ohliger MA, Grant AK, Willig J, Sodickson DK. Self-Calibrated Spiral Parallel Imaging. In: Proc 10th Annual Meeting ISMRM, Honolulu, Hawaii USA, 2002. p 2390.
7. Qian Y, Zhang Z, Stenger VA, Wang Y. Self-calibrated spiral SENSE. Magn Reson Med 2004;52(3):688-92.
8. Bornert P, Stuber M, Botnar RM, Kissinger KV, Koken P, Spuentrup E, Manning WJ. Direct comparison of 3D spiral vs. Cartesian gradient-echo coronary magnetic resonance angiography. Magn Reson Med 2001;46(4):789-94.
9. Irarrazabal P, Nishimura DG. Fast three dimensional magnetic resonance imaging. Magn Reson Med 1995;33(5):656-62.
10. Jackson JI, Meyer CH, Nishimura D, Macovski A. Selection of a convolution function for Fourier inversion using gridding. IEEE Trans Med Imaging 1991;10(3):473-478.
11. Ohliger MA, Grant AK, Sodickson DK. Ultimate intrinsic signal-to-noise ratio for parallel MRI: electromagnetic field considerations. Magn Reson Med 2003;50(5):1018-30.

12. Scheffler K, Heid O, Hennig J. Magnetization preparation during the steady state: fat-saturated 3D TrueFISP. Magn Reson Med 2001;45(6):1075-80.
13. Weiger M, Boesiger P, Hilfiker PR, Weishaupt D, Pruessmann KP. Sensitivity encoding as a means of enhancing the SNR efficiency in steady-state MRI. Magn Reson Med 2005;53(1):177-85.
14. Zhu Y, Hardy CJ, Sodickson DK, Giaquinto RO, Dumoulin CL, Kenwood G, Niendorf T, Lejay H, McKenzie CA, Ohliger MA and others. Highly parallel volumetric imaging with a 32-element RF coil array. Magn Reson Med 2004;52(4):869-77.

CHAPTER 8. GENERAL DISCUSSION AND FUTURE DIRECTIONS

Advances in parallel MRI signify an exciting breakthrough in accelerating imaging speed beyond previous limits. Clinical practitioners have begun to harness the benefits of accelerated imaging to enhance diagnostic accuracy, reduce medical costs and increase patient comfort. At the same time, active research continues to address various challenges posed by parallel MRI. In this dissertation work, six specific issues pertaining to parallel image reconstruction have been explored, and theoretical and practical solutions have been proposed.

This chapter begins with a summary of the major results in each area of the thesis, proceeds to briefly discuss future directions, and concludes with a speculative outlook on parallel MRI in general.

SECTION 8.1 Summary of Major Results

As previously shown, image reconstruction in parallel MRI can be formulated as a generalized linear inverse problem, where the MR matrix equation can be expressed as $\mathbf{s} = \mathbf{E}\boldsymbol{\rho}$, where s is the signal, $\mathbf{E}$ the encoding matrix, and $\boldsymbol{\rho}$ the spin density. Each piece of

work in this thesis is thematically related to explorations of one or more components of this matrix equation. Collectively, Chapters 2-7 have presented a logical progression in solving an inverse problem, that is: a) determine the encoding matrix $\mathbf{E}$, b) compute an inverse $\mathbf{E}^{-1}$, and c) characterize and minimize the error involved.

Chapter 2 presented a method for computing the encoding matrix $\mathbf{E}$ that exploits the inherently self-calibrating characteristics of many non-Cartesian *k*-space trajectories to obtain accurate and consistent results. This method can be applied to existing pulse sequences without modification, and does not require any additional scan time in order to obtain necessary coil sensitivity calibration information.

Chapters 3 and 4 discussed methods that exploit physical properties of $\mathbf{E}$ and $\boldsymbol{\rho}$, for efficient and stable inversion of $\mathbf{E}$. In Chapter 3 presented the PARS technique, which exploits the principle of *k*-space locality to simplify the inversion of $\mathbf{E}$. In many cases, the encoding matrix is too large to invert directly. The PARS technique judiciously partitions $\mathbf{E}$ into many small and sub-blocks that can be inverted independently, making the overall process of the matrix inversion $\mathbf{E}$ efficient and stable.

To further facilitate the matrix inversion process, Chapter 4 has integrated *a priori* phase information of the underlying spin density $\boldsymbol{\rho}$ into the parallel image encoding matrix. Instead of performing partial Fourier reconstruction and parallel image reconstruction separately, this integrated approach incorporates a phase constraint of $\boldsymbol{\rho}$ to transform the inherently complex-valued matrix equation $\mathbf{s} = \mathbf{E}\boldsymbol{\rho}$ into a strictly real-valued one. The number of unknowns is reduced by a factor of two, and the solution $\boldsymbol{\rho}$ can be obtained in a single step.

Chapters 5 and 6 have explored characterization and minimization of errors in parallel image reconstruction. Chapter 5 presented a numerical technique for computing the noise distribution in magnitude-combined parallel image reconstructions. This in turn has enabled quantitative comparisons among different parallel MRI reconstruction techniques. Analytic

solutions have been noted for special cases. In addition, a bias correction algorithm based on a maximum-likelihood estimation has been presented.

In Chapter 6, parallel imaging has been studied as an array processing technology. Theoretical lower bounds on noise variance have been derived using the Cramer-Rao bounds for exact (unbiased) and inexact (biased) parallel image reconstructions. In this chapter it was shown that existing unbiased parallel image reconstruction strategies have already achieved the Cramer-Rao bounds. For biased parallel image reconstruction strategies which may or may not have converged to the Cramer-Rao bounds, a noise-minimization algorithm has been proposed to ensure such convergence.

Lastly, Chapter 7 has reported a preliminary case study in clinical cardiac imaging using some of the techniques developed in this thesis. Additional imaging parameters such as RF excitation angles, data acquisition windows, effects of T1 recovery, and the relative effectiveness of T2-preparation and fat-saturation pulses have been considered. Tradeoffs between imaging speed, image artifact and noise amplification have been evaluated.

SECTION 8.2 Future Directions

The evolution of parallel MRI points toward a persistent quest for faster and better medical imaging. The familiar matrix equation $\mathbf{s} = \mathbf{E}\boldsymbol{\rho}$ provides valuable insights that parallel imaging can go faster and better by carefully designing a better encoding matrix $\mathbf{E}$. As discussed in Chapter 1 and other places in the thesis, the quality of reconstructed images relies heavily on the distinctiveness of the spatial information embedded in $\mathbf{E}$. Conventional MRI has made image reconstruction both robust and seemingly trivial by the use of Fourier encoding. The engineering efforts required to achieve that goal, however, were not trivial. The same argument can be made with parallel imaging. At the current stage, parallel image reconstruction techniques (including those proposed in this thesis) are capable of providing robust image reconstruction at relatively low acceleration factors. Higher acceleration factors will necessitate a full complement of the generalized encoding functions (as discussed

in Eq. [1.9]) in order to ensure a well-conditioned **E**. Continual engineering efforts will be required to achieve this goal.

8.2.a Advanced Spatial Encoding Using Magnetic Field Gradients

Non-Cartesian trajectories, as demonstrated in Chapters 2, 3, and 7, provide many benefits for parallel imaging. In addition to the inherently self-calibrating capability, non-Cartesian parallel imaging provides an efficient sampling strategy, especially for multi-dimensional accelerated parallel MRI. The spiral and radial parallel image reconstructions performed in this thesis are a demonstration of two-dimensional accelerated parallel imaging. The ability to accelerate in several dimensions allows optimal use of spatial encoding by RF coil arrays. It has been shown in recent work that at a given total acceleration factor, a 2-D accelerated method will have less noise amplification than a corresponding 1-D counterpart (1). The natural implication is that a 3-D acceleration scheme is highly desirable, and may even be necessary for applications at very high acceleration factors. Future development of a 3-D non-Cartesian trajectory, which can flexibly traverse the 3-D *k*-space in order to complement the limitations on the underlying RF coil encoding functions, will provide definitive spatial encoding advantages over conventional Cartesian acquisitions.

8.2.b Advanced Spatial Encoding Using Many-Element Coil Arrays

MR hardware development, which made parallel MRI possible in the first place, will continue to be a critical area of research. There is little question that the trend of hardware development is pointing toward "more". The number of coil elements in an array will continue to increase. At the time this dissertation work began, a typical RF coil array had four to six elements. Nowadays, new coil arrays for parallel imaging have been designed with 32 elements (2). The primary limitation on the number of coil elements, at least for now, is the number of RF receiver channels available on commercial MRI scanners. Major vendors are introducing MRI scanners with more RF receiver channels, and the gap between research scanners and commercial products is closing. When the number of coil elements is large enough (e.g., 128), this trend may lead to the design of grid-based coil arrays, where

there will be more emphasis on the overall arrangement of the array pattern, and arguably less emphasis on the design of an individual element. At that point, parallel imaging may have an even closer correspondence with other array processing technologies.

8.2.c Advanced Spatial Encoding Using Spatially-Selective RF Pulses

As discussed in Chapter 1, the possibility of using spatially-selective RF pulses to tailor the generalized spatial encoding remains an intriguing proposition (3). Currently, the field of "transmit" parallel imaging, which usies coil arrays to the shorten RF excitation time for a given excitation pattern, is undergoing rapid development (4,5). Perhaps in due time, the field of "receive" parallel imaging discussed in this thesis can also benefit from these developments.

SECTION 8.3 General Conclusions

The thesis work has been devoted to the investigation of the physical and engineering principles of spatial encoding and decoding in parallel MRI. MR image reconstruction has been formulated as a generalized inverse problem. Under this linear algebraic framework, the results of several original research studies have been presented, and solutions to the constraints of parallel image reconstruction have been proposed. This dissertation will provide useful tools and insights for future developments in parallel MRI, and lead to better and faster clinical imaging.

Chapter 8 References

1. Ohliger MA, Grant AK, Sodickson DK. Ultimate intrinsic signal-to-noise ratio for parallel MRI: electromagnetic field considerations. Magn Reson Med 2003;50(5):1018-30.
2. Zhu Y, Hardy CJ, Sodickson DK, Giaquinto RO, Dumoulin CL, Kenwood G, Niendorf T, Lejay H, McKenzie CA, Ohliger MA and others. Highly parallel volumetric imaging with a 32-element RF coil array. Magn Reson Med 2004;52(4):869-77.
3. Kyriakos WE, Panych LP. Optimization of Parallel Imaging By Use of Selective Excitation. In: Proc 9th Annual Meeting ISMRM, Glasgow, Scotland, UK, 2001. p 768.
4. Katscher U, Bornert P, Leussler C, van den Brink JS. Transmit SENSE. Magn Reson Med 2003;49(1):144-50.
5. Zhu Y. Parallel excitation with an array of transmit coils. Magn Reson Med 2004;51(4):775-84.